Dissertation
submitted to the
Combined Faculties of the Natural Sciences and Mathematics
of the Ruperto-Carola-University of Heidelberg. Germany
for the degree of
Doctor of Natural Sciences

Put forward by
Lisa, Scalone
born in: Maniago
Oral examination: 17.05.2017

Retrieval of Cirrus Optical Properties in the near-IR spectral range within the NASA ATTREX Project

Referees: Prof. Dr. Klaus Pfeilsticker
Prof. Dr. Thomas Leisner

Sine Sole Sileo.

Abstract. In this work we propose a new method based on a near-IR ($[0.9-1.7]\mu m$) full spectral retrieval to infer the optical properties of ice particles forming cirrus clouds. The quasi in situ near-IR spectroscopic measurements were collected by the mini-DOAS instrument ($S/N \sim 300$) on board the NASA Global Hawk within a critical region for climate forcing, i.e. the tropical tropopause layer (TTL). The theoretical model is set up using a Monte Carlo radiative transfer model for spectral radiance simulations (1% relative error) and a Mie scattering code to calculate the optical properties ($\sim 10^{-4}-10^{-5}$ relative errors). The ice particles are described as mass equivalent spheres and they are treated as a statistical ensemble by making use of two particle size distributions, both parameterized in terms of the ice water contents (IWCs). The novel method is applied to one flight segment where a cirrus cloud over the eastern Pacific TTL was probed during the convective season (NH winter). The cloud optical depths (ODs) are retrieved using the oxygen absorption band ($^1\Delta_g \leftarrow ^3\Sigma_g^-$) at $1.27\mu m$, while the IWCs are inferred from the ice absorption band ($1.49\mu m$). The results are compared and discussed with the simultaneous observations of the Cloud Physics Lidar (CPL) and in situ measurements of Hawkeye, NOAA Water, UCATS and DLH. Together, they provide relevant information concerning the microphysics of cirrus within the TTL. Tropical cirrus clouds are extremely important for the global radiative net budget (greenhouse vs. albedo effects), since they exert a direct impact on the TTL and on the lower stratosphere in a changing climate. The new method proved to be a powerful tool for cirrus optical properties retrieval. The thresholds for the inferred results are 0.01 for ODs (3.2% relative error) and $10^{-3}[g/m^3]$ for the total IWCs (3.8% relative error).

Zusammenfassung. In der vorliegenden Doktorarbeit wird eine neue spektroskopische Methode vorgeschlagen und untersucht, mit deren Hilfe man die optischen Eigenschaften vom Zirren und die sie bildenden Eisteilchen messen kann. Die Methode beruht auf der spektroskopischen Analyse mit Hilfe eines "full spectral fit" des im Limb empfangenen atmosphärischem Himmelsstreulicht im nahen infraroten Spektralbereich ($[0.9-1.7]\mu m$). Die quasi in situ Messungen wurden mit Hilfe des mini-DOAS Instrumentes ($S/N \sim 300$ im nearIR) an Bord der NASA Global Hawk in der tropischen Tropopausenregion (engl. TTL) durchgeführt. Die TTL ist eine für den Strahlungsantrieb des Klimas kritische Region. Die spektralen Radianzen des Vorwärtsmodell wurden mit Hilfe eines Monte Carlo Modells mit einem relativen Fehler von 1% berechnet und die Streuung an Wolkenteilchen sowie ihre optischen Eigenschaften wurde dabei mittels eines Mie Algorithmus (Genauigkeit $10^{-4}-10^{-5}$) modelliert. Dabei werden die Eisteilchen als massenäquivalente Kugeln modelliert und ihre Größenverteilung wird mit zwei Verteilungen beschrieben, mit der Eiswasserkonzentration (engl. IWC) als freier Parameter. Die neuartige Methode wird auf die Beobachtung einer Zirruswolke angewandt, die während der konvektiven Jahreszeit (im NH Winter)

über dem Ostpazifik von Bord der Global Hawk beprobt wurde. Die optische Dicke der Wolke wurde mit Hilfe der Absorption von Sauerstoff ($^1\Delta_g \leftarrow^3 \Sigma_g^-$) bei $1.27\mu m$ bestimmt und die Eiswasserkonzentration mit Hilfe der Eiswasserbande bei $1.49\mu m$. Die Ergebnisse werden mit gleichzeitigen Messungen der Instrumente des Cloud Physic Lidars (CPL) und der in situ Instrumente Hawkeye, NOAA Water, UCATS und DLH verglichen. Diese liefern die relevante Information zur IWC und der Größenverteilung der Wolkenteilchen. Die Zirruswolke entstand in dem Ausfluss eines starken konvektiven Ereignisses. Zirren haben maßgeblich einen großen Einfluss auf die Zusammensetzung der TTL und der Stratosphäre. Mit der neuen Methode lassen sich Zirren mit optischen Dichten von 0.01 mit einem relativen Fehler von 3.2% und Eiswasserkonzentrationen von $10^{-3}[g/m^3]$ mit einem relativen Fehler von 3.8% nachweisen.

Riassunto. In questo lavoro proponiamo un nuovo metodo per ricavare le proprietà ottiche delle particelle di ghiaccio che formano i cirri usando l'intera gamma spettrale del vicino infrarosso ($[0.9-1.7]\mu m$). Le misure spettroscopiche quasi in situ sono state collezionate dallo strumento mini-DOAS ($S/N \sim 300$) a bordo del drone della NASA, Global Hawk, in una regione critica per l'inflenza sui cambiamenti climatici, cioè la tropopausa nella fascia tropicale (TTL). Il modello teorico si basa su un algoritmo Monte Carlo per il trasferimento radiativo che simula le radianze spettrali (errore relativo 1%) e su un codice di scattering di Mie per il calcolo delle proprietà ottiche (errori relativi $10^{-4}-10^{-5}$). Le particelle di ghiaccio sono descritte come sfere di massa equivalente e sono trattate come un ensemble statistico facendo uso di due diverse distribuzioni di probabilità sulle dimensioni delle particelle, entrambe parametrizzate in termini di contenuti in ghiaccio (IWCs). Il nuovo metodo è applicato ad una parte di volo in cui è stato osservato un cirro nella TTL sul Pacifico orientale durante la stagione convettiva (inverno nell'emisfero nord). Gli spessori ottici della nuvola (ODs) sono ricavati usando la banda di assorbimento dell'ossigeno ($^1\Delta_g \leftarrow^3 \Sigma_g^-$) a $1.27\mu m$, mentre gli IWCs sono dedotti dalla banda di assorbimento del ghiaccio ($1.49\mu m$). I risultati sono confrontati e discussi con le misure in situ degli strumenti CPL, Hawkeye, NOAA Water, UCATS e DLH. Insieme, questi risultati forniscono informazioni rilevanti riguardo la microfisica dei cirri nella TTL, e forniscono osservazioni di un forte flusso convettivo. I cirri tropicali sono di notevole importanza per il bilancio radiativo globale (effetto serra contro effetto di albedo), dal momento che hanno un impatto diretto sulla TTL e sulla bassa stratosfera in un clima che sta cambiando. Il nuovo metodo si è rivelato essere un potente strumento d'indagine per ricavare le proprietà ottiche dei cirri. I valori di soglia per i risultati ottenuti sono 0.01 per gli ODs (errore relativo 3.2%) e $10^{-3}[g/m^3]$ per il contenuto totale in ghiaccio (errore relativo 3.8%).

Contents

Introduction 1

1 Cirrus within the Topical Tropopause Layer 5

1.1 The Earth's Atmosphere 6

1.1.1 The Tropical Tropopause Layer 12

1.2 Cirrus Clouds 15

1.2.1 Cirrus Radiative Forcing 17

1.2.2 Cirrus and TTL 20

2 The NASA ATTREX Project 23

2.1 Global Hawk and Instrument Descriptions 24

2.1.1 The mini-DOAS instrument 31

2.2 Science flights 33

3 The Measurements 37

3.1 The mini-DOAS Data 38

3.1.1 Spectrometer Wavelength Calibration 39

3.1.2 Dark Current and Offset Voltage 41

3.2 The CPL Data 43

3.3 The Hawkeye Data . . . 45
3.4 The NOAA Water Data . . . 47
3.5 The UCATS and DLH Data . . . 47

4 Theory and Modeling **49**
4.1 The Radiative Transfer Equation . . . 50
4.2 The McArtim Radiative Transfer Model . . . 54
4.2.1 Photon Number Dependence . . . 57
4.3 The Detector . . . 58
4.4 Setup of the Atmosphere . . . 60
4.4.1 Geometric Coordinates . . . 61
4.4.2 Trace Gases Profiles . . . 63
4.4.3 Solar Spectrum . . . 64
4.4.4 Ocean Surface Albedo . . . 65
4.5 Molecular Extinction . . . 68
4.5.1 Molecular Absorption . . . 68
4.5.2 Rayleigh Scattering . . . 79
4.6 Ice Particle Extinction . . . 83
4.6.1 The Gamma Distribution . . . 84
4.6.2 The Lognormal Distribution . . . 85
4.6.3 The Mie Theory . . . 90
4.6.4 The Double-Precision Lorenz-Mie Scattering Code . . . 97
4.6.5 The Henyey-Greenstein Phase Function . . . 101
4.6.6 The Optical Properties of Ice Spheres . . . 102
4.7 Flowchart of the RTM Simulations . . . 105

5 The Retrieval Procedure **107**

5.1 The DOAS Method 108
5.2 Optical Properties Retrieval for Cirrus 109
5.2.1 Oxygen Absorption Band Analysis - Part I 110
5.2.2 Convergence Criterion and Estimation of the Errors 116
5.2.3 Oxygen Absorption Band Analysis - Part II 119
5.2.4 Ice Absorption Band Analysis 121

6 Results and Discussions **127**
6.1 The Data Selection 128
6.1.1 Cirrus Layer Configuration 133
6.2 Inferred Cirrus ODs 135
6.3 Inferred IWCs and IWPs 138

Conclusions **155**

List of Figures **161**

List of Tables **165**

List of Abbreviations and Acronyms **167**

Bibliography **169**

Publications **181**

Acknowledgements **183**

Introduction

Cirrus clouds, in particular thin and sub-visible cirrus, and their radiative effects have been identified as one of the major unsolved components in weather and climate research [12, 71, 72]. Recently, through the availability of high flying aircraft equipped with remote sensing and in situ instrumentations, these high located cirrus have intensively been studied [24, 61, 118, 134].

Figure 1: "*Obscured by clouds*", Pink Floyd (1972). Album cover.

The cirrus clouds are globally distributed and they cover about 20% of the globe. They are present at all latitudes and they undergo continuous changes in coverage, thickness and position [26].

High level cirrus may contain a significant amount of large crystals with different shapes. They have low concentrations of ice particles and therefore they are usually thin and weak absorbers [71].

In the last decades the influence of optically thin and little absorbing cirrus on the radiation field of the Earth's atmosphere system has been investigated. Their impact on the radiative budget is twofold: they reflect light in the solar region (albedo effect), thus leading to a negative forcing, while in the thermal IR region they lead to a positive forcing (greenhouse effect) [117, 70, 82]. These so called greenhouse-versus-albedo effects generate significant differential cooling and heating in vertical as well as horizontal scales; in particular thin cirrus clouds have been shown to have a positive radiative forcing [53]. Because of these radiative effects, cirrus clouds are important regulators of climate [100, 101]. In the tropics, where they can cover up to 43% of the globe [135], they are also important in directly regulating the stratospheric water vapour concentration [55, 30, 111] and indirectly, through the radiative effects, the transport of troposphere air into the stratosphere [31, 3, 4, 9, 45].

Finally, cirrus clouds can impact the chemical composition of the atmosphere, since cloud particles may incorporate nitrogen and sulphate species as well as activate reactive species [96, 97, 7, 115, 43, 1, 8, 76]. However, the importance of these processes are still less explored.

Therefore, it is fundamental to have a detailed understanding of their physical and optical characteristics, as the radiative transfer, water budget, and chemistry depend on their microphysical properties, equivalently, their particle size distributions and habits, as well as their vertical location and horizontal structure [71].

Cirrus clouds in the tropical tropopause layer (TTL) are frequently optically thin and thus difficult to observe due to their weak signature in space-borne remote sensing applications [64, 105, 95, 127].

In this work we used limb-scanning near-IR absorption spectroscopy measurements, collected on board the NASA's Global Hawk during the ATTREX project [59] to pro-

vide observations of cirrus clouds in the TTL. The data were collected over the eastern and western Pacific regions in early 2013 and 2014.

The developed new method is based on the observation of the ice absorption signature in scattered/reflected sunlight spectra detected within cirrus clouds. The limb geometry significantly increases the sampling distance determining a view along the cirrus cloud for hundreds kilometers and, hence, the capability of detecting ice absorption features even for very thin cirrus clouds.

In order to retrieve the optical properties of ice cirrus particles from the collected measurements, a new algorithm is developed which makes use of a Monte Carlo radiative transfer model (McArtim) [20]. The model is implemented with a Lorentz-Mie code for optical properties calculations [86, 85]; the optical properties of cloud particles are characterized using particle size distributions parameterizations involving ice cirrus particles in the tropical environment [81].

The present work is divided in several chapters as follows.

In chapter 1 the background knowledge about this study is provided. A description concerning the ice cirrus clouds, their dynamic and composition within the tropical tropopause layer is presented.

In chapter 2 the NASA ATTREX project is introduced. A brief characterization of the instrumentations, science campaigns, and objectives of the missions is given.

Chapter 3 provides an overview of the mini-DOAS collected near-IR spectroscopic measurements and introduces the CPL, Hawkeye, NOAA Water, UCATS and DLH data required to validate the proposed new method.

In chapter 4 a thorough treatment of the model built for the retrieval of optical properties of ice cirrus particles is provided.

Chapter 5 provides the methods and strategies applied on both the spectroscopic data

and the model in order to retrieve the microphysical characteristics of cirrus.

Finally, chapter 6 provides the validation of the proposed new methods and shows the results obtained for one flight segment. These results are supported by the direct comparison of the findings obtained by other instruments on board the aircraft.

1 Cirrus within the Topical Tropopause Layer

In this chapter, the background relevant for this work is summarized.

We provide first some general information about the Earth's atmosphere system and the tropical tropopause layer.

Following, the actual knowledge about cirrus clouds formation, location and microphysical properties as well as their radiative forcing is summarized.

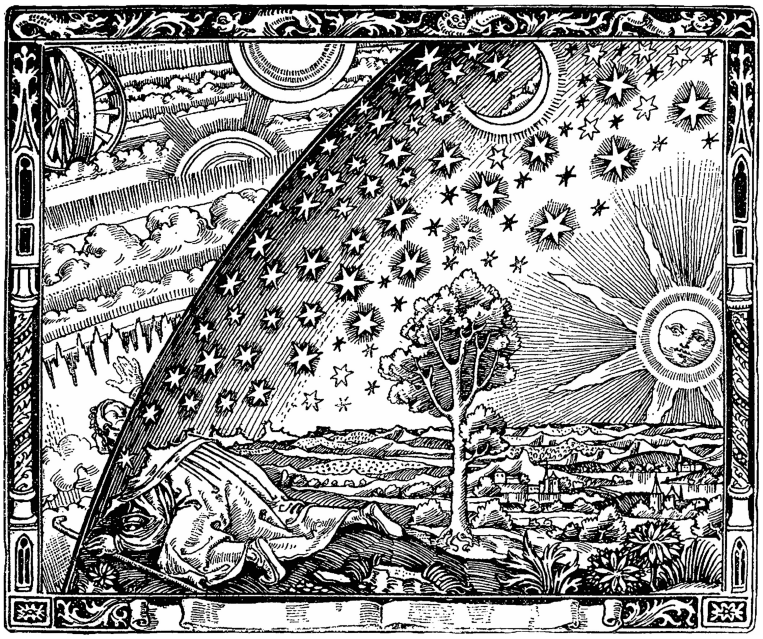

Figure 1.1: L'atmosphère: météorologie populaire (p. 163), Nicolas C. Flammarion (Paris, 1888).

In the end, a brief overview concerning the role of cirrus within the tropical tropopause layer is depicted, showing some recent measurement results.

1.1 The Earth's Atmosphere

Within this section we briefly describe the Earth's atmosphere which is a very complex and interacting system, therefore for a comprehensive treatment of this subject refer to [124]. The atmosphere represents the set of all gases which enfold a celestial body. These molecules are trapped by the gravity generated by the planet itself. The atmosphere of the Earth is not homogeneous and thus it can be divided in several layers, i.e. spheres, which have different characteristics. From the Earth's surface to the top of the atmosphere the different spheres are: troposphere, stratosphere, mesosphere, thermosphere and exosphere. The division derives from the behavior of the vertical thermal gradient. In other words, when the gradient of the temperature profile changes its sign within the atmosphere, a discontinuity layer is present, called *pause*, which

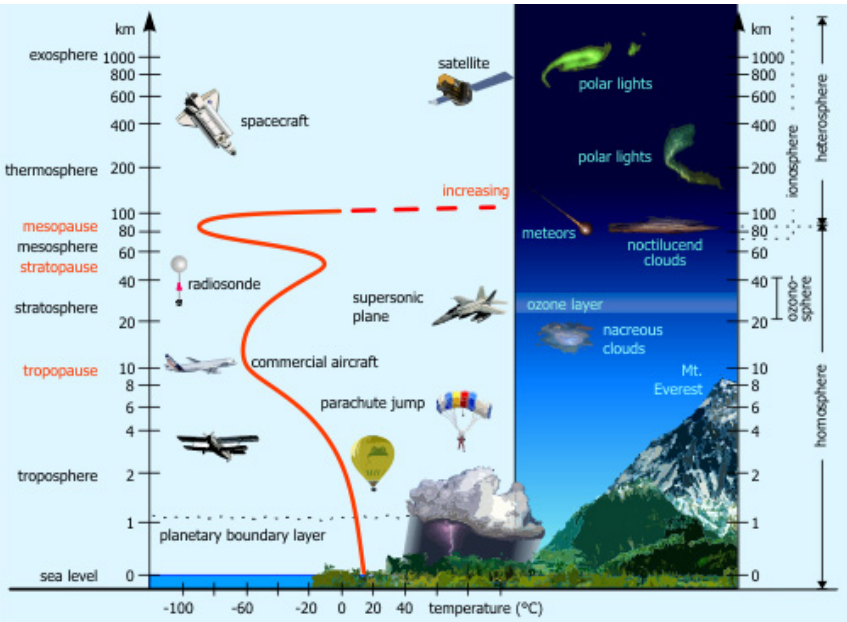

Figure 1.2: Vertical structure of the Earth's atmosphere. Along the x-axes the temperature is plotted while on the y-axes the different layers as a function of the altitude are shown. Adapted from `http://www.theozonehole.com`.

marks the border between one and another sphere.

For example, the World Meteorological Organization (WMO) defines the boundary between the troposphere and the stratosphere as the layer where an abrupt change in lapse rate usually occurs. It is defined as the lowest level at which the lapse rate decreases to $-2\mathrm{K/km}$ or less, provided that the average lapse rate between this level and all higher levels within $2\mathrm{km}$ does not exceed $-2\mathrm{K/km}$ [133]. In Fig.1.2 a schematic of the vertical structure of the atmosphere is reported.

Concerning the chemical composition, the atmosphere can be considered as a gas mixture and apart from dust, aerosols and pollutants of anthropogenic origin, it shows the average composition reported in table 1.1.

Table 1.1: Average chemical composition of the atmosphere at the ground.

Gas	**Symbol**	**Content**
Nitrogen	N_2	78.08%
Oxygen	O_2	20.94%
Argon	Ar	0.93%
Carbon dioxide	CO_2	392ppm
Neon	Ne	18ppm
Helium	He	5ppm
Methane	CH_4	2ppm
Krypton	Kr	1.1ppm
Hydrogen	H_2	0.5ppm
Xenon	Xe	0.08ppm

To these gases we can add the water vapour, which shows a huge variability as a function of the altitude, ozone ($0.04\mathrm{ppm}$ in the troposphere and $6\mathrm{ppm}$ in the stratosphere) and the tracers such as nitrogen oxides (NO, NO_2, N_2O), carbon monoxide (CO), ammonia (NH_3), sulfur dioxide (SO_2) and hydrogen sulfide (H_2S).

The atmospheric trace gases are not uniformly distributed and they show different spatial distributions which may also strongly change with time. For example referring to

absolute concentrations, the water vapour is more abundant at the ground and decreases with the altitude, as well as oxygen or carbon dioxide, while molecules such ozone are more abundant in the stratosphere compared to the ground. In any case the average chemical composition of the major atmospheric constituents (N_2, O_2, He, etc.) doesn't change until the altitude of 100km is reached. In fact, from the sea level up to 100km we refer to the homosphere, while above 100km we usually talk about heterosphere. In the heterosphere the chemical composition of the air starts to change and when moving to higher altitudes preferably light molecules and atoms can be found until a sort of vacuum is reached.
Concerning the different layers forming the vertical structure of the Earth's atmosphere, starting from the ground, we find first the troposphere.

The **troposphere** is the layer where almost all meteorological phenomena can happen. It contains the 80% of the total gaseous mass and the 99% of all the water vapour mass. The air within the troposphere is heated by the solar energy absorbed by the ground and the temperature profile decreases when moving towards higher altitudes, reaching is lower value of ca. 200K at the tropopause ($\sim$ 17km). Due to the presence of a strong negative temperature gradient the air tends to move from the lower troposphere to the upper levels generating strong moist convective currents.
The general circulation within the troposphere can be interpreted as the way the Earth system tends to reach the thermodynamic equilibrium. In fact, due to a different absorption of the solar radiation moving from the equator to the poles, it happens that, during a solar year, different zones are heated more than others and this gradient gives rise to the general circulation. The different absorption of the solar radiation is just a consequence of the inclination of the Earth's rotation axes with respect to the ecliptic. Generally speaking, the atmospheric circulation can be divided in three major cells

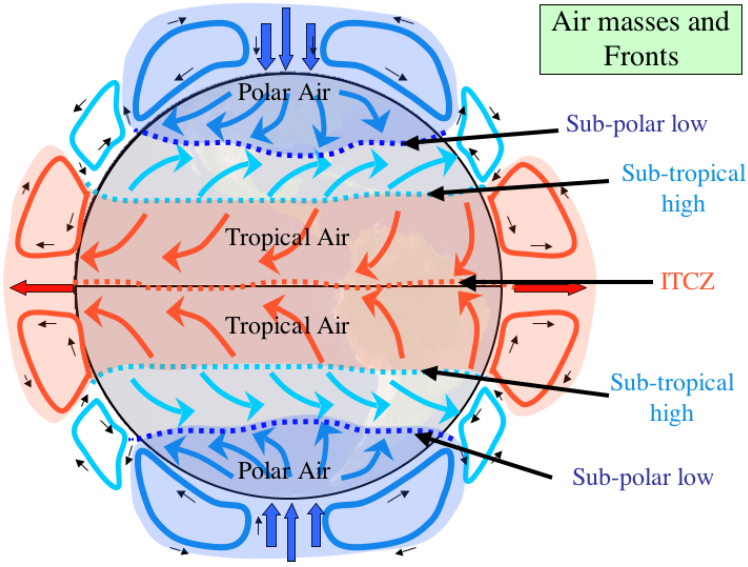

Figure 1.3: Sketch of the global circulation: Hadley cells (red), Ferrel cells (light blue), and Polar cells (blue). Adapted from `http://montessorimuddle.org`.

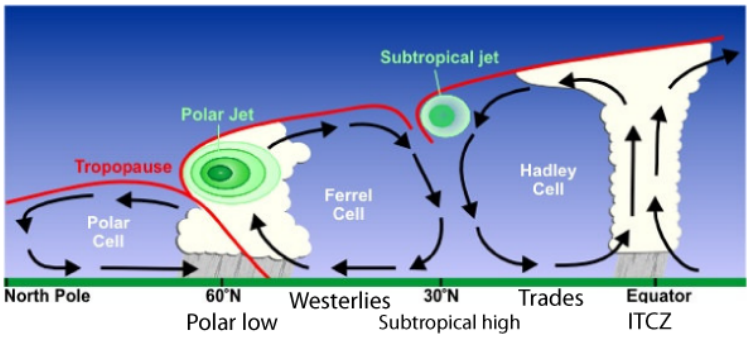

Figure 1.4: Sketch of the dynamic within the troposphere. Adapted from `http://www.globalsailingweather.com`.

in the boreal hemisphere and three in the austral hemisphere. They are called the Hadley, Ferrel and Polar cells, respectively. The Hadley cells move the air masses from the equator to the tropics, the Ferrel cells cover the midlatitudes, and the Polar cells extend from the poles to the polar circles. In Fig.1.3 a sketch of the global circulation is depicted, while in Fig.1.4 a longitudinal section of the northern hemisphere, showing the atmospheric dynamics, is reported. The Hadley system provides an example of a thermally direct circulation [46]: warm air rises from the equator to the tropopause; it is pushed poleward by air rising from below; it is radiatively cooled when moving poleward; it sinks near subtropics; and finally it moves equatorward returning near the surface (see Fig.1.4). Near the tropopause, the air masses moving poleward are turned eastward by the Coriolis force, creating the subtropical jet streams that flow

from west to east. Analogously, near the surface, the equatorward return flow is turned to the west by the Coriolis force. The resulting surface winds, with both an equatorward and a westward component, are referred to as the trade winds.

The Ferrel cells are a consequence of the Hadley and Polar cells on either side of them and they are driven by thermal winds. The Ferrel system is weak, and air flow and temperatures within it are variable. It provides an example of thermally indirect circulation [46]. The air of the Ferrel cell that descends in the subtropics returns poleward at the ground level, and as it does so it deviates toward the east. In the upper atmosphere, the air moving toward the equator deviates toward the west. Both of those deviations are driven by conservation of angular momentum. They are not a closed loop because of instability of their thermal winds that can be easily disrupted, e.g. by the local passage of a cold front. As the Hadley cells give rise to the tropical jets, the Ferrel cells give rise to the Polar jets (see Fig.1.4).

Finally, the Polar cells are strong closed loops of thermally direct circulation. At the polar front, the air rises to the tropopause ($\sim 8\mathrm{km}$) and moves poleward, as it does so, the upper level air mass deviates toward the east. When the air reaches the polar areas, it has cooled and is considerably denser than the underlying air. It descends, creating a cold, dry high-pressure area. At the polar surface level, the mass of air is driven toward the 60th parallel, replacing the air that rose there, and the polar circulation cell is complete (see Fig.1.4). As the air at the surface moves toward the equator, it deviates toward the west. Again, the deviations of the air masses are the result of the Coriolis force. The outflow of air mass from the cell creates harmonic waves in the atmosphere known as Rossby waves. These ultra-long waves determine the path of the polar jet stream, which travels within the transitional zone between the tropopause and the Ferrel cell.

The **stratosphere** is the second layer of the Earth's atmosphere. It is characterized by a positive vertical thermal gradient. This increment of the temperature derives at lower altitude from the absorption of solar radiation by ozone and, in upper levels, by the dissociation of the ozone molecule due to the absorption of UV radiation. In addition, the thermal gradient derives from the thermal emission which is particular strong in the lower stratosphere. Because the temperature in the stratosphere increases with altitude, it does not cause convection and has a stabilizing effect on atmospheric conditions in the region. Hence, the stratosphere is dynamically stable and stratified [107].

In the **mesosphere**, which begins at about 50km, the temperature decreases again due to decreasing solar heating and increasing cooling by carbon dioxide radiative emission. Here, the coldest point of the Earth is reached, with temperatures around 140K.

Above the mesosphere lies the thermosphere. The **thermosphere** extends from ca. 95km to ca. 500km. It is characterized by an increment of the temperature because it is exposed to the most energetic solar radiation and the air molecules are barely present there. The so called Karman line lies within this layer (around 100km), and it represents the boundary between the Earth's atmosphere and the outer space.
There is a region covering partially the mesosphere and the thermosphere which is called the ionosphere [62]. Here, the thin air and the presence of energetic solar radiation as well as cosmic rays gives rise to a large ionized section where the air molecules can interact easily with the electromagnetic radiation. In this respect, this region provides a screen effect on some wavelengths intervals (e.g. it reflects almost entirely the radio waves from the Earth's surface), and it is strongly dependent from the solar activity.

The last layer is the **exosphere**. Within this layer the kinetic temperature can reach

and exceed 2270K, under these conditions the rare molecules have velocities that allow them to escape from the Earth's gravitational potential and they cannot be trapped anymore in the atmosphere system. The classical thermal escape mechanism is when individual molecules have a velocity higher than the so called escape velocity. This is known as Jeans escape [13]. Within a gas, the average velocity of a molecule is determined by temperature, but the velocities of individual molecules change due to collisions. The variation of the kinetic energy is described by the Maxwell distribution. Individual molecules in the high tail of the distribution may reach escape velocity, and this happens when the mean free path of the molecule, i.e $l = kT/\sqrt{2}\pi d^2$ (k is the Bolzmann's constant, T and p are temperature and pressure of the molecule, and d its diameter), is comparable to the scale height in the atmosphere, defined as $H = kT/mg$ where k is the Boltzmann constant, T the temperature, m the mass of the molecule and g the gravity acceleration. An atmosphere with a high enough pressure and temperature can also undergo a different escape mechanism called hydrodynamic escape [50]. In this situation the atmosphere simply flows off like a plume of molecules into space, due to pressure gradients initiated by thermal energy deposition. By hydrodynamic escape is possible to lose heavier molecules that would not normally be lost. This mechanism interests mostly gaseous exoplanets very close to their central star.

1.1.1 The Tropical Tropopause Layer

The tropical tropopause layer (TTL) defines an atmospheric layer that presents properties of both the troposphere and the stratosphere. In the tropics, this layer may extend vertically over several kilometers. Due to its definition, within the TTL two different dynamical regimes exist and this interface acts as a gate to the stratosphere for atmospheric substances as water vapour, other chemicals with sufficient large lifetime, or variable amounts of the so-called very short lived species (VSLS), which play

an important role for stratospheric chemistry [31, 90].

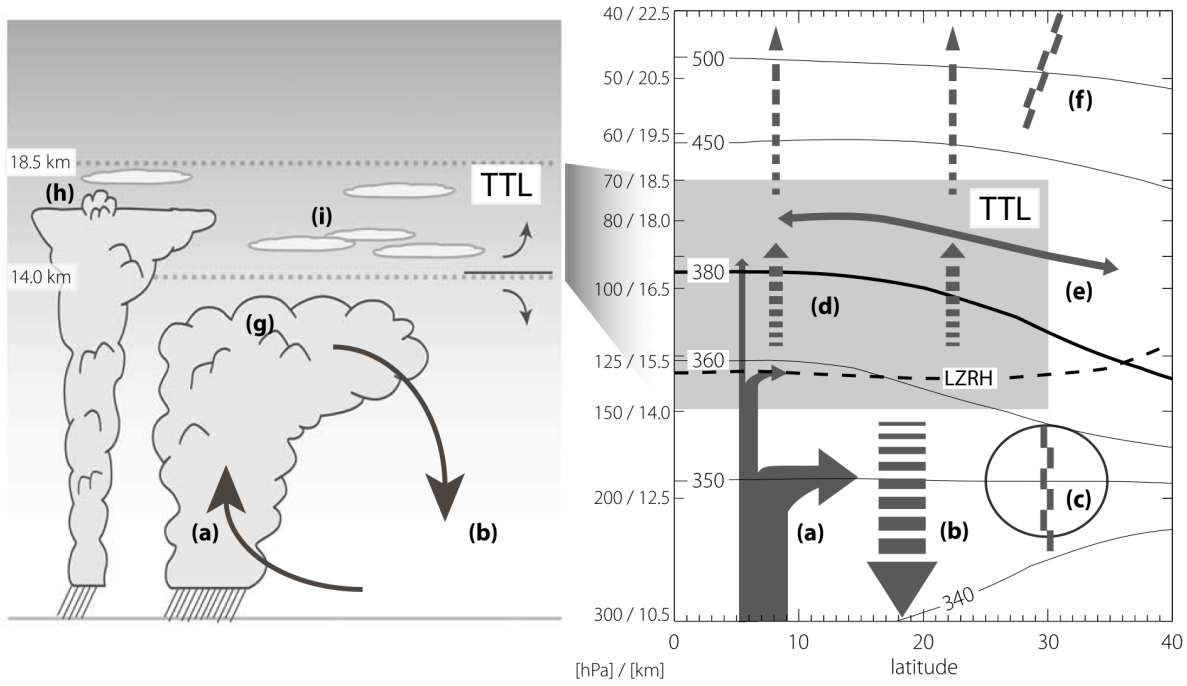

Figure 1.5: Sketch of cloud processes and transport (left), and zonal mean circulation (right). The arrows indicate circulation, the black dashed line is clear-sky level of zero net radiative heating (LZRH), and the black solid lines show isentropes (in K, based on the European Center for Medium Range Weather Forecasts 40-years reanalyzed (ERA-40 [122])). See the text for more details. Adapted from [31].

In Fig.1.5 a schematic of the tropical troposphere and lower stratosphere is shown. The letter (a) indicates deep convection: main outflow around 200hPa, rapid decay of outflow with height in the TTL, and rare penetrations into the TTL (and beyond), fast vertical transport of tracers from boundary layer into the TTL. The letter (b) means radiative cooling at the cloud top, and divergence of air masses towards the subtropics. (c) indicates subtropical jets, which limit quasi-isentropic exchange between troposphere and stratosphere (transport barrier). The letter (d) indicates radiative heating, which balances forced diabatic ascent. The letter (e) means rapid meridional transport of trac-

ers and mixing. (f) stands for the edge of the *tropical pipe*, relative isolation of tropics, and stirring over extratropics (*the surf zone*). The letter (g) means deep convective clouds. (h) indicates the convective core overshooting its level of neutral buoyancy. The letter (i) stands for ubiquitous optically (and geometrically) thin, horizontally extensive cirrus clouds, often formed in situ [31].

The upper and lower bounds of the TTL are commonly defined in terms of the potential temperature. The potential temperature at a pressure P is the temperature that an air parcel would acquire if adiabatically brought to a standard reference pressure P_0 usually 1000hPa. The potential temperature is denoted θ and, for air, is given by

$$\theta = T\left(\frac{P_0}{P}\right)^{R/c_p} \tag{1.1}$$

where T is the absolute temperature (in K) of the parcel, R is the gas constant of air, and c_p is the specific heat capacity at a constant pressure. $R/c_p = 0.286$ for air. The adiabatic transport of air parcels happens without energy exchange with the environment. In contrast, diabatic transport allows exchange of energy by radiation, both heating or cooling of the air parcel. The potential temperature is an important dynamically quantity because it defines the lines or surfaces in the atmosphere, where air parcels move. Air parcels can move along (adiabatic) and perpendicular (diabatic) to isentropes of potential temperature. Meridional horizontal transport is mainly limited by the potential vorticity conservation, i.e. conservation of energy and angular momentum.

Fueglistaler et al. [31] indicate the lower bound of the TTL at 14km with a pressure around 150hPa and a potential temperature of 355K. While for the upper bound, they suggest the altitude of 18.5km, a pressure of 70hPa and potential temperature of 425K. Depending on the cloud cover, the LZHR (level of zero net radiative heating) lies at higher altitudes respect to the lower bound of the TTL. In some studies, the lower bound of the TTL is also located at the LZHR for clear sky conditions which often corresponds to a minimum in ozone or at even lower altitudes, i.e. at the level of maximum

outflow. Due to thermodynamics reasons the upper bound is placed at the cold point tropopause (CPT) around 17km [32].

1.2 Cirrus Clouds

Cirrus clouds are globally distributed, they are present at all latitudes and without respect to land or sea or season of the year. They undergo continuous changes in the area coverage, optical thickness, texture, and position [71, 72]. They form when water vapour undergoes condensation at altitudes above $\sim 5.5\text{km}$ in temperate regions and above $\sim 6.4\text{km}$ in tropical regions.

In the tropics, cirrus clouds are related to mesoscale convective systems associated with the convective activity over the oceans [54, 77] more vigorous over land (Africa and South America). The global cirrus cover has been estimated to be about 20 to 25%, but recent analysis using the satellite infrared channels at the $15\mu\text{m}$ CO_2 band has shown that in the tropics their frequency is more than 40% [64, 105, 95, 127, 135].

Cirrus clouds usually reside in the upper troposphere region where temperature are generally colder than 230K, and in the TTL $< 200\text{K}$. Because of their high location in the atmosphere, direct observation of the composition and structure of cirrus is difficult and requires a highflying aircraft platform or sophisticated remote sensing instruments (e.g. CALIPSO [132]). Moreover, the high altitudes, and thus low temperatures, guarantee that the composition of cirrus clouds is mainly ice.

Concerning the shape and the size of ice crystals, we actually know that the ice crystal growth is primarily controlled by the temperature and the relative humidity inside the cloud. If ice crystals undergo collisions and coalescence due to gravitation pulling and turbulence, more complicated shapes can result [71, 5].

In midlatitudes, cirrus clouds have been found to be composed of primarily nonspherical ice crystals with shapes ranging from solid and hallow columns to plates, bullet

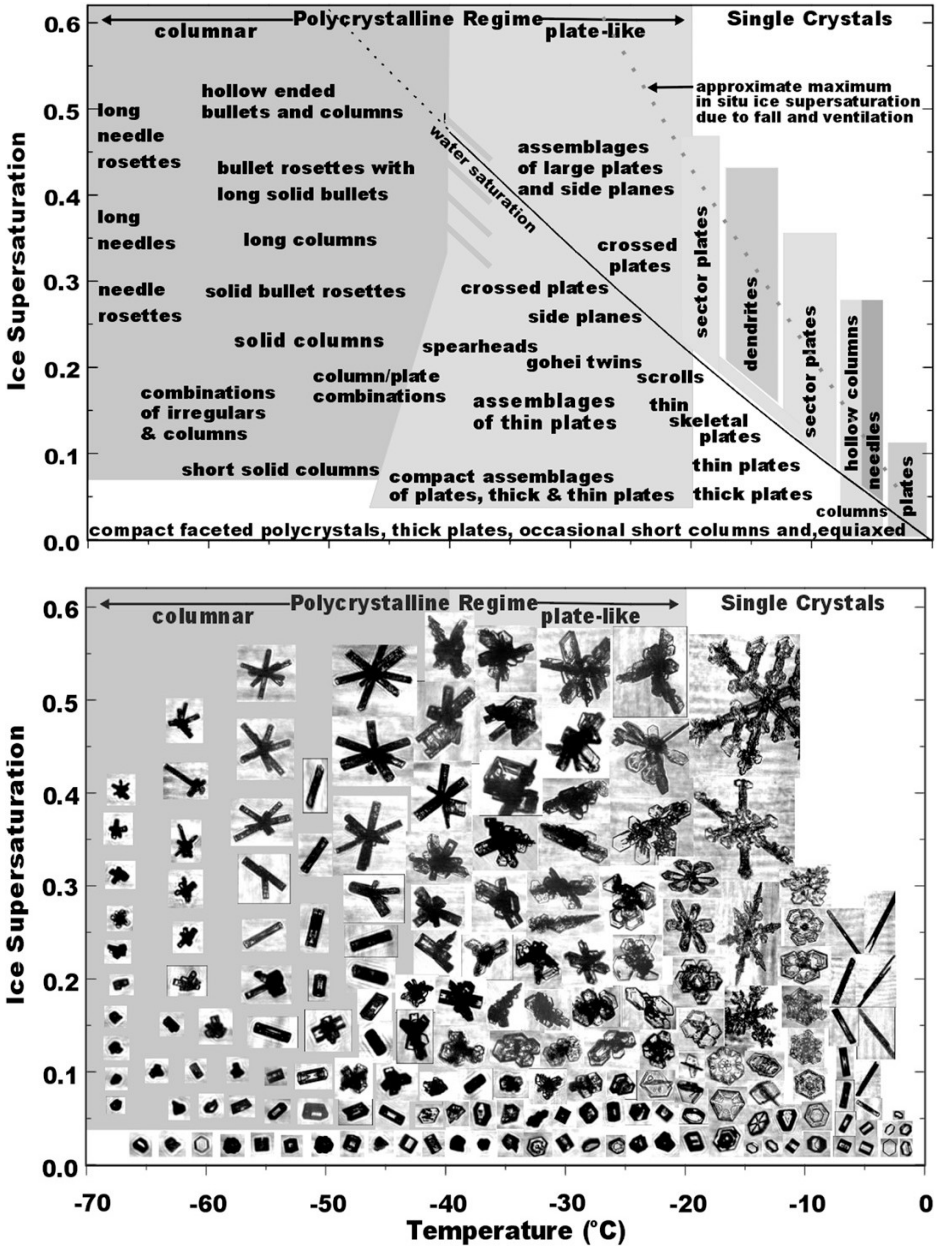

Figure 1.6: Habit diagram in text and pictorial format for atmospheric ice crystals derived from laboratory results and CPI images gathered during AIRS II and other field studies. Adapted from [5].

rosettes, and aggregates, and with sizes spanning from about 10μm to thousands of micrometers [34, 35]. In Fig.1.6 the habit diagram for ice crystals derived from laboratory and atmospheric studies is reported [5]. Observations in midlatitudes also reveal that at the cloud top small columns and plates are predominant, whereas at the lower part of the cloud bullet rosettes and aggregates are most common [34, 35].

Limited in situ measurements in the tropical cirrus clouds [131, 28, 125], illustrate that their ice crystal size ranges from about 10μm to 1000μm with four predominant shapes: bullet rosettes, aggregates, hollow columns, and plates. In the tropics, observations reveal that large sizes are associated with warmer temperatures mostly related to convection.

In the arctic, the ice crystal shapes are more often a combination of irregular types with sizes larger than about 40μm. In the Antarctic, the prevalence of long needle ice crystal types has been observed [65].

It is clear then that ice crystals vary substantially in size and shape from the tropic to midlatitudes to the polar regions.

Sometimes, a horizontal orientation of some columnar and plate crystals in cirrus has been observed from a number of lidar backscattering depolarization measurements [49, 89, 93]. Moreover, the observation of halos and arcs confirms that in some cases cirrus clouds can have crystals with specific orientations.

1.2.1 Cirrus Radiative Forcing

Cirrus clouds can absorb, reflect and transmit the sun radiation as well as they can reflect (poorly) and transmit the thermal infrared emitted from the surface and the atmosphere and, at the same time, emit infrared radiation according to the temperature structure within them [33]. Therefore, it is fundamental to know the ice crystal size and shape distributions and cloud thickness, because these parameters determine the

relative strength of the radiative effects, which are essential components of the climate forcing by cirrus [100, 101].

These radiative effects are determined by the basic scattering and absorption properties of ice crystals and their IR emission properties.

In order to infer the impact of cirrus clouds on the radiation field of the Earth and the atmosphere and thus on the climate, the term *cloud radiative forcing* has been developed to quantify the relative significance of the solar albedo and infrared greenhouse effects. It is defined as the difference between the net radiative fluxes at the top of the atmosphere in clear and cloudy conditions when satellite measurements are conducted. In case of surface-based radiation measurements, it is defined as the difference between the surface downwelling radiation in all-sky and clear-sky conditions [75]. The addition of a cloud layer in a clear sky would lead to more sunlight reflected back to space and thus reduce the amount of solar energy available to the atmosphere and the surface. On the other hand, the trapping of atmospheric thermal emission by non absorbing cirrus clouds enhances the radiative energy, or heat, available in the atmosphere and the surface. Based on theoretical calculations, it has been shown that the infrared greenhouse effect for cirrus clouds generally predominates over their solar albedo effect, except when the clouds contain very small ice crystals on the order of a few micrometers, which exert a strong solar albedo effect. The relative significance of the solar albedo versus infrared greenhouse effects is clearly dependent on the ice crystal size and the amount of ice in the cloud [53, 31, 70, 111]. Because of the complexity of sorting cirrus signatures from satellite observations, the radiative forcing of cirrus estimated to calculate the global effect is still rather uncertain.

The first issue concerning the role of cirrus clouds in the greenhouse warming produced by the increase in greenhouse gases such as H_2O, CO_2, CH_4, NO_2, CFCs, and O_3 is their possible changing occurrence with location and season. A positive feedback would also

be evident if the high cloud cover increase because of gas-induced perturbations of the atmospheric structure [53]. Theoretical experiments using one- and three-dimensional climate models have illustrated that high clouds with low emission temperature could exert a positive feedback resulting in the amplification of the temperature increase at the surface [71].

However, the extent and degree of this feedback and temperature amplification have not been reliably quantified for the following reasons.

First, the prediction of cirrus cloud cover and their position based on physical principles is a difficult task, and successful prediction using climate models has been limited. This difficulty is also associated with the uncertainties and limitations in inferring cirrus cloud cover and position from current satellite instruments. Unfortunately, we do not have sufficient cirrus cloud data to correlate with the greenhouse warming that has occurred so far [71, 72].

The second issue that determines the role played by cirrus in climate and greenhouse warming is related to the variation of ice water content and crystal size within these clouds. Based on aircraft observations, some evidence suggests that there is a distinct correlation between temperature and ice water content and crystal size [73]. An increase in temperature supports an increase in ice water content. Also, ice crystals tend to be smaller (larger) at colder (warmer) temperatures. The implication of these microphysical relationships is significant for climate.

For high cirrus containing primarily nonspherical ice crystals, illustrative results from one-dimensional climate models suggested that the balance of solar albedo versus infrared greenhouse effects, i.e. positive or negative feedback, depends not only on ice water content, but also on ice crystal size [73, 70, 82].

This competing effect differs from low clouds containing purely water droplets, in which a temperature increase in their formation region would result in a larger liquid water

content. In this case, clouds would then reflect more sunlight, thus leading to a negative feedback.

1.2.2 Cirrus and TTL

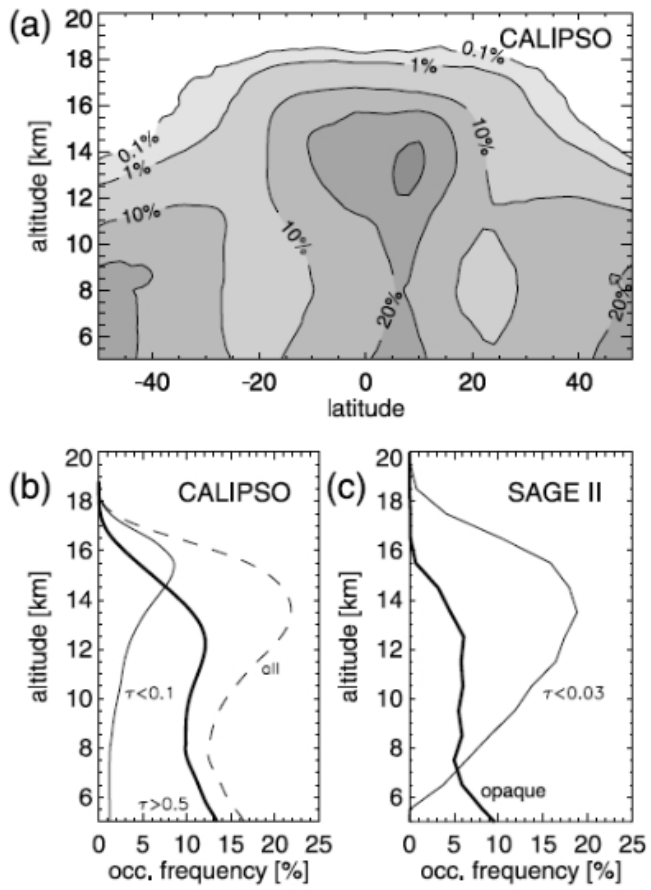

Figure 1.7: (a) Zonal mean cloud occurrence frequency (Jun.06-Feb.07, CALIPSO). Below, profiles for cloud occurrence frequency for thick or thin clouds, from CALIPSO ((b) thick ($\tau > 0.5$), thin ($\tau < 0.1$)) and SAGE II ((c) thick (opaque), thin ($\tau < 0.03$)). Adapted from [31].

As described in the previous subsection, cirrus clouds have an important role for the structure of the TTL due to their impact on the radiative budget (greenhouse-albedo effects); furthermore they indicate the activity of vertical transport by convection and steady uplifting of air by net radiative heating, and in situ condensation.

In the TTL layers of cirrus are commonly observed, and they can be optically thin (e.g., optical depth $\tau < 0.03$ [108]) and then contain small amounts of water (e.g., $40 ppbv$ [93]). The cirrus in TTL form either as remnants of convective anvil clouds (about half of them), or by in situ condensation supporting different shapes and structures (the other half) [19, 94, 80, 78].

Generally speaking, the factors that

contribute to longer cloud persistence in the TTL than elsewhere are a high relative humidity and small particle sizes due to very limited available water vapour [54, 77]. The radiative heating of the clouds may also lead to diabatic uplift of the cloud layer (*cloud lofting*), or drive a local circulation that brings sufficient water vapour to sustain the cloud [55, 113].

In order to explain how optically thin clouds with very little ice water content can exist on a time scale of a day, and extend over hundreds kilometers despite being in a thermodynamically delicate state (a small warming would immediately lead to complete evaporation, while a cooling would induce particle growth and rapid sedimentation), a stabilization of the cloud layer is required. It may arise from the gradual cooling supersaturation and condensation in upwelling air [77].

In the context of direct observations of the cloud properties that characterize cirrus in the TTL, it has to be underlined that different sensors are sensitive to different particle sizes, have different viewing geometry, and have different spatial and temporal coverage. For example, the radar instruments can observe only large particles ($> 100\mu m$) optically thick, but they are insensitive to thin cirrus [74, 44]. The lidar observations from the ground or aircraft are sensitive to optically thin clouds, but in optically thick clouds the lidar is too much attenuated for the particle detection in rear part of the clouds. [49, 89, 93].

The satellite observations, such as the Cloud-Aerosol Lidar and Infrared Pathfinder Satellite Observation (CALIPSO)[1] or the Stratospheric Aerosol and Gas Experiment (SAGE II)[2] have provided a new view of the cirrus cloud heights in the TTL as well as optical depths and relative occurrence frequencies [131, 28, 125]. Fig.1.7 summarizes the zonal mean cloud occurrence frequency determined from CALIPSO (panel (a)) and the occurrence profiles for optical thin and thick clouds detected by the CALIPSO (panel

[1] https://www.nasa.gov/mission_pages/calipso/main/index.html
[2] https://data.giss.nasa.gov/sageii/

(b)) and SAGE II (panel (c)) instruments [31].

2 The NASA ATTREX Project

The Airborne Tropical TRopopause EXperiment (ATTREX[1]) was initiated by the National Aeronautics and Space Administration (NASA) in 2010 in order to study cirrus clouds, water and chemistry of the tropical tropopause layer (TTL).

Figure 2.1: The NASA ATTREX project logo.

The ATTREX missions [59, 58] have been providing the measurements needed to improve the insufficient understanding of TTL physical processes and poor representations of these processes in global models.

In this view, the project aimed to improve the prediction on future changes in stratospheric humidity and ozone, taking into account several TTL processes as convection, transport, cloud microphysics, atmospheric waves, and chemistry.

The study of the processes controlling the TTL composition largely controls the stratospheric composition due to its tight physical constraints (cf., for water vapour and soluble gases). Further, the Brewer-Dobson circulation transports air upward through

[1] https://espo.nasa.gov/home/attrex/

the TTL and this results into a transport throughout the entire stratosphere.
A particular focus of the NASA ATTREX was to study the dehydration of air entering the stratosphere by ice crystal growth and sedimentation near the cold tropical tropopause. In this respect radiative transfer calculations are showing that even small changes in stratospheric humidity have larger significant climate impacts with respect to the effects caused by greenhouse gases [25, 116].
Since direct observations, i.e. measurements, of the TTL composition are sparse in comparison to other climatically important parts of the atmosphere, the ATTREX project has made use of the NASA Global Hawk (GH) Unmanned Air System (UAS) in order to provide unprecedented high-resolution measurements of water vapour, meteorological conditions, cloud properties, tracer and chemical radical concentrations, and radiative fluxes over multiple seasons and over large geographic regions.

2.1 Global Hawk and Instrument Descriptions

Figure 2.2: The NASA GH during a checkout flight (credit: NASA).

The Global Hawk (see Fig.2.2) is designed to operate at altitudes above 15km and with a ceiling altitude of ca. 20km. It is a fully autonomous unmanned aerial system requiring a pre-loaded mission plan but, during the flight, it is also possible to reschedule the mission plan. The GH has numerous payload compartments and has also mounting locations under its wings.
In Fig.2.3 the accessible compart-

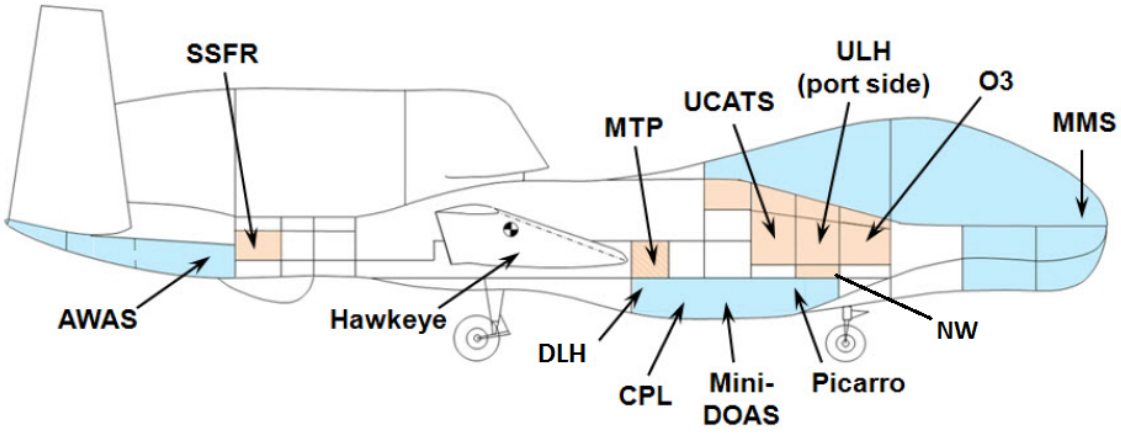

Figure 2.3: Sketch of the instrument arrangement on aircraft. The blue (red) sectors identify the unpressurized (pressurized) compartments. Courtesy of E. Jensen (2015).

ments as well as the locations of instruments assembled on board are shown. The GH altitude, range and payload capacity are well suited for large, regional scale research missions in the TTL.

The NASA GH aircraft is based at the Dryden Flight Research Center (DFRC) in California. The duration of one science flight is about 30 hours and the speed reached by the drone is ca. 200m/s. The Global Hawk operations require a ground control station and for the GH deployments also a mobile operation facility has been developed.

In Table 2.1 the instruments of the ATTREX mission are summarized.

Cloud Physics Lidar (CPL)

The CPL [18] is a multi-wavelength backscatter lidar. It utilizes a high repetition rate, low pulse energy transmitter and photon-counting detectors. The CPL operates at three wavelengths (355, 532 and 1064nm), with depolarization measurement at 1064nm. An

Table 2.1: Instruments on board the GH with specific topic of investigation.

Instrument	**Measurements**
Cloud Physics Lidar (**CPL**)	Aerosol/cloud backscatter
Ozone (**O_3**)	O_3
NOAA Water (**NW**)	H_2O, IWC
Advanced Whole Air Sampler (**AWAS**)	Tracers with varying lifetimes
Chromatograph for Tracers (**UCATS**)	O_3, CH_4, N_2O, SF_6, H_2O, CO
Picarro Cavity Ringdown Spectrometer	CO_2, CO
UAS Laser Hygrometer (**ULH**)	H_2O
Diode Laser Hygrometer (**DLH**)	H_2O
Hawkeye	Ice crystals properties
Solar, Infrared Radiometers (**SSFR**)	Radiative fluxes
Meteorological Meas. System (**MMS**)	Temperature, winds
Microwave Temperature Profiler (**MTP**)	Temperature profile
Absorption Spectrometer (**mini-DOAS**)	BrO, NO_2, cirrus properties

off-axis parabola is used for the telescope to collect the backscattered light. The CPL is designed with a nominal $100\mu rad$ field of view to minimize effects of multiple scattering. CPL data[2] products are typically provided at $30m$ vertical resolution and $1sec$ horizontal resolution ($\sim 200m$ at the nominal speed of $200m/s$). The quantities measured by CPL are attenuated backscatter and cloud optical depths.

Ozone (O_3)

The Ozone photometer [59] is an autonomous dual beam UV absorption photometer for in situ ozone measurements. It has been designed to achieve high sensitivity and fast response in a small package with minimal power requirements. The ozone concentration is calculated from a differential absorbance measurement between sample and reference cells.

[2] https://cpl.gsfc.nasa.gov/

NOAA Water (NW)

The NOAA Water instrument [120] is a two-channel, closed-path, tunable diode laser absorption spectrometer designed for the measurement of water vapour and enhanced total water (vapour + condensed phase). The instrument utilizes wavelength-modulated spectroscopy with second harmonic detection near $2694\mathrm{nm}$ to achieve high precision with a $79\mathrm{cm}$ double-pass optical path. The detection cells are operated under constant temperature, pressure, and flow conditions to maintain a constant sensitivity to H_2O independent of the ambient sampling environment. An on board calibration system is used to perform periodic in situ calibrations to verify the stability of the instrument sensitivity during flight.

Advanced Whole Air Sampler (AWAS)

The AWAS instrument [59] collects air samples from airborne platforms for detailed analysis of a wide range of trace gases with sources from anthropogenic emissions, from biomass burning, and from the marine boundary layer, with certain compounds (e.g. organic nitrates) that have a unique source in the equatorial surface ocean. The post-flight analysis in the laboratory makes use of a gas chromatographic technique and of a coupled mass spectrometer for the detection of specific gases. AWAS also measures a full suite of halocarbons that provide information on the role of short-lived halocarbons and halogen budgets in the upper troposphere and lower stratosphere regions, and on trends of HCFCs, CFCs, and halogenated solvents.

UAS Chromatograph Atmospheric Trace Species (UCATS)

The Unmanned aircraft systems Chromatograph Atmospheric Trace Species [59] is three different instruments in one enclosure:

i. a two-channel gas chromatograph that measures nitrous oxide, sulfur hexafluoride,

hydrogen, carbon monoxide and methane;

ii. a dual-beam ozone photometer;

iii. a tunable diode laser spectrometer for water vapour.

The H_2-CO-CH_4 gas cromatograph channel can be switched between flights for measurement of atmospheric chlorofluorocarbon-11 (CFC-11), CFC-12, and halon-1211.

Picarro Cavity Ringdown Spectrometer

The Picarro instrument [59] is a cavity ringdown spectrometer and it measures concentrations of CO_2, CH_4, and CO with very high stability and precision.

UAS Laser Hygrometer (ULH)

The Unmanned aircraft systems Laser Hygrometer [59] is a single-channel, near-infrared, open-path tunable diode laser spectrometer that measures atmospheric water vapour in situ. ULH operates in two modes: harmonic wavelength modulation spectroscopy and direct absorption. The harmonic spectroscopy is precise and fast, and time-averaged data are recorded at a user-adjustable rate between 1 and 40Hz. The direct absorption measurements are highly accurate, and are used as an in-flight calibration of the faster harmonic data.

Diode Laser Hygrometer (DLH)

The DLH [59] is a near-infrared external open-path diode laser spectrometer operating in the $\sim 1.39\mu m$ water vapour absorption band. The instrument measures the water vapour mixing ratio in the atmosphere by wavelength modulated differential absorption.

Hawkeye

Hawkeye [69, 83] measures the size distribution of cloud and precipitation particles, provides high-resolution images of cloud particles, with the potential to remove artifacts from ice particle shattering. This is accomplished by combination of technology developed in three existing optical cloud particle probes:

i. a fast forward scattering spectrometer probe, that measures size distributions from 1 to 50 microns, records individual particle statistics and removes shattered particles using inter-arrival times;

ii. a cloud particle imager with upgraded imagery, capable of recording up to 500 frames per second;

iii. a 2D-Stereo probe that is configured with one channel to provide full-view images of particles from $10\mu m$ to $1.28mm$, and a second channel configured to provide full-view images of particles from $50\mu m$ to $6.4mm$.

By using the information about particle dimensions along the direction of flight, it produces particle size distributions from $1\mu m$ to several cm.

Solar, Infrared Flux Radiometers (SSFR)

Two instruments [63] measure solar and terrestrial radiation. The Solar Spectral Flux Radiometer covers the near-ultraviolet, solar, and near-infrared wavelength range from $360nm$ to $2200nm$. A pyrgeometer provides broadband infrared irradiance from 4.5 to $42\mu m$. Optical inlets for both instruments are mounted on top and at the bottom of a platform and provide upwelling, downwelling and net irradiance. The two instruments together provide complete measurements required for the cloud energy budget, radiative forcing, and heating rate. The spectral resolution of SSFR is crucial to distinguish

radiative effects of clouds from those of, e.g., the underlying surface. It also allows an independent retrieval of cloud optical thickness and effective drop or crystal radius.

Meteorological Measurement System (MMS)

MMS [57] provides calibrated, in situ state measurements of static pressure, static temperature, and three-dimensional wind and turbulence indices. Differencing the measured aircraft ground velocity from the true air speed vector it produces the 3-dimensional wind vector. The embedded GPS inertial navigation system provides the aircraft altitude, position, velocity, and acceleration data.

Microwave Temperature Profiler (MTP)

MTP [59] is a passive, microwave radiometer that measures the brightness temperature of the atmosphere due to the natural thermal emission from oxygen molecules near 60GHz. During a 15sec scan cycle from near-zenith to near-nadir in the flight direction, measurements are made at three frequencies and at ten elevation angles. The thirty measured brightness temperatures are converted to air temperature versus altitude using a modified statistical retrieval procedure developed especially for the airborne application.

Mini-Differential Optical Absorption Spectrometer (mini-DOAS)

The mini-DOAS instrument [118] is an automated UV/vis/near-IR spectrometer which uses scattered solar light in the limb (horizon) and nadir (downward) geometry to detect path-integrated concentrations of BrO, O_3, NO_2, O_4 from the UV/vis channels [130], as well as ice water concentration and ice water path of cirrus clouds from the near-IR channel. Spectral retrieval of trace gas slant column densities from the measured absorption spectra are achieved using established DOAS methods.

2.1.1 The mini-DOAS instrument

The mini-DOAS instrument is a custom-built limb-scanning system based on earlier balloon-borne and airborne mini-DOAS instruments [66, 99, 123]. The instrument [118] consists of a telescope/scanner unit connected via fiber bundles to a three spectrometer assembly containing UV, visible and near-IR channels. Fig.2.4 shows a sketch of the instrument setup.

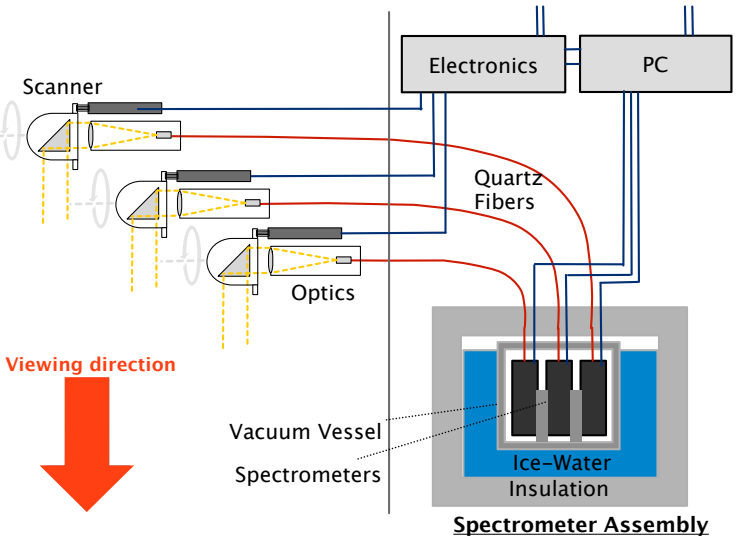

Figure 2.4: Sketch of the mini-DOAS instrument.

The optical spectrometers are housed in a vacuum vessel and, in order to reach thermal stabilization during each flight, a 9 liters water-ice mixture bath was used. The ice-water tank is insulated. According to these arrangements, the spectrometer temperatures during each flight were maintained to within ± 0.1K.

In order to overcome the detector non-linearity, the spectrometers are operated at the same saturation levels (50%) through an adjustment of the integration time.

Each spectrometer is connected to a small telescope using a quartz (UV) and glass fiber bundles (VIS and near-IR). To minimize the UV spectrometer straylight, an optical bandpass filter is placed in front of the lens of the UV telescope. To suppress the second grating order in the near-IR channel, an optical filter is used. The final optical components of the telescopes are the internal reflection prisms, which are mounted with one side in flight direction (for a limb geometry) and turn the incoming light beam by

Table 2.2: Specifics of the mini-DOAS spectrometers.

	UV	**VIS**	**near-IR**
Spectrometer	Ocean Optics QE65000	Ocean Optics QE65000	Ocean Optics NIRQuest 512
Grating [g/mm]	2400	1800	150
Entrance slit [μm]	200	100	100
Wavelength range [nm]	301-387	410-425	896-1730
Dispersion [nm/pixel]	0.085	0.11	1.6
Spectral resolution [nm]	0.6	0.8	~10
Filter	Hoya UG-340	none	Schott RG 850

90 degrees onto the filter/lens. In the final configuration, the telescopes point 2° away from the flight direction in order to minimize scattered light from the GH fuselage [118]. Optically the telescopes view a rectangle in the sky that is ~ 0.25° in elevation and ~ 1° in the azimuth. The scanner has a precision of better than 0.01°. Since the pointing accuracy and the viewing geometry are important parameters for the vertical profile retrievals, during the alignment procedure, the pitch of the aircraft is extracted from the GH navigation system and an absolute calibration relative to the aircraft limb with an accuracy of better than ~ 0.2° is achieved.

It should be noted that the GH flights were mostly performed with long straight flight legs (see Fig.2.5) and that turns were not flown frequently. This translates into a minor impact of the aircraft roll which did not affect the data analysis. Special features of the telescope assembly are diffuser plates mounted in zenith direction above each telescope that allow the measurements of direct sunlight. These diffusers are used only when they are directly illuminated by the sun. As the measurements of solar references are crucial in DOAS applications, low solar zenith elevation direct sun measurements were performed at least once during each flight.

For the spectrometer data acquisition, an industrial computer (Moxa V2101) is used. It allows to control the telescope elevation angle, to regulate and monitor the tele-

scopes temperature and instrument assembly, and to communicate with the GH and the ground. Communications with the aircraft include synchronization with the GH main clock every 90sec, reading of aircraft status data (at 1Hz frequency) and broadcast of instrument status to the aircraft and the ground.

2.2 Science flights

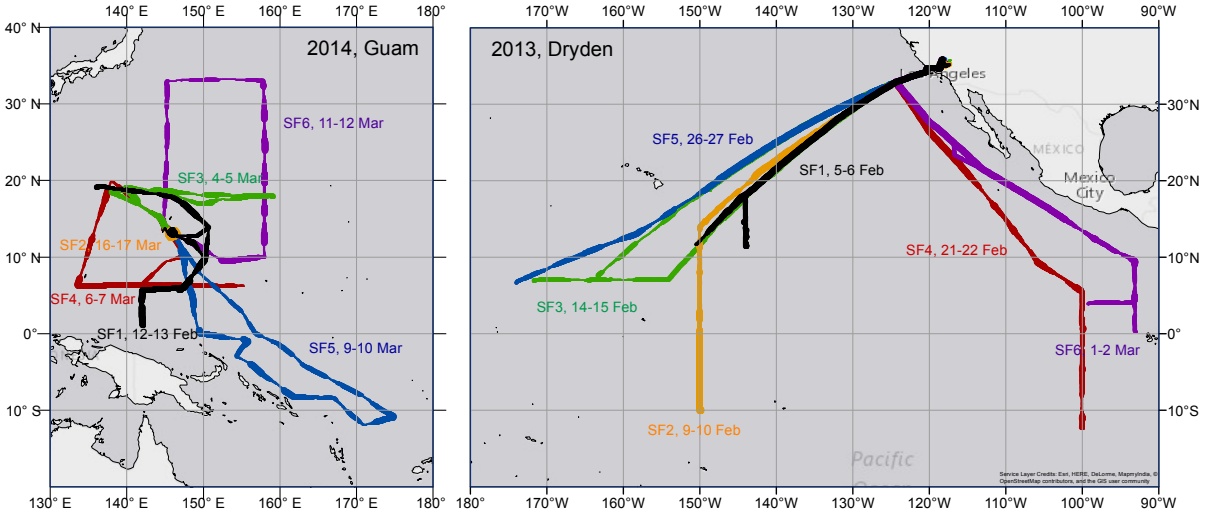

Figure 2.5: Flight tracks of the GH during the ATTREX mission over the eastern Pacific in 2013 (right map) and over the western Pacific in 2014 (left map). The thickness of the colored lines indicates the altitude of the aircraft. To thin lines correspond lower altitudes (~ 14km), while to thick lines correspond higher altitudes (~ 18km).

Within the framework of the NASA ATTREX project several sorties were planned. Test flights were done in 2011 for technical check-up of all the instrumentation on board and two ferry flights were performed in 2014 to transport the drone to the Anderson airfield on Guam.

The significant scientific flights for data collection were at least twelve. Six of those flights were done in 2013 (first campaign) using as ground base the Dryden Flight

Table 2.3: List of the NASA ATTREX science flights.

Flight	Date	Science foci
Eastern Pacific - 2013		
SF1-2013	Feb. 5-6	Central Pacific TTL profiling
SF2-2013	Feb. 9-10	Meridional TTL cross section
SF3-2013	Feb. 14-15	Central Pacific TTL profiling
SF4-2013	Feb. 21-22	Eastern Pacific meridional cross section
SF5-2013	Feb. 26-27	Central Pacific cold TTL cirrus profiling
SF6-2013	Mar. 1-2	Eastern Pacific cold TTL cirrus profiling
Western Pacific - 2014		
SF1-2014	Feb. 12-13	TTL survey, cirrus sampling
SF2-2014	Feb. 16-17	TTL survey, cirrus sampling
SF3-2014	Mar. 4-5	Cyclone Faxai sampling, cirrus sampling
SF4-2014	Mar. 6-7	TTL survey, wave measurements
SF5-2014	Mar. 9-10	Southern survey, convective outflow
SF6-2014	Mar. 11-12	Northern/midlatitude survey

Research Center in California (US) and the others were performed in 2014 (second campaign) using as ground base the Anderson Air Force Base in Guam (US). The average length of these flights was 25 hours, with no flight exceeding 30 hours.

In Fig.2.5 the sorties of the GH for both 2013 and 2014 campaigns are shown, while in Table 2.3 a brief description for each science flight is reported.

The first campaign was based in Dryden (CA, US) in order to cover the subtropical and tropical eastern Pacific zone during the winter season. In this period the TTL reaches the coldest temperature and extremely dry air enters the stratosphere [31, 90].

The second campaign was based in Guam, during the boreal winter, because of its proximity to the TTL over the western Pacific. With the six flights covering a period of almost one month, it was sufficient to span most of the 40-50 days Madden-Julian oscillation in large scale tropical convection. The tropical tropopause is seasonally at its coldest temperature during this period, and Guam is near the coldest TTL temperatures, the lowest water vapour, the highest incidence of observed TTL clouds, and the

region with the largest mean ascent rate [31].

3

The Measurements

In this chapter the measurements necessary for the retrieval procedure of the optical properties are briefly introduced.

The mini-DOAS instrument provides the near-IR spectral radiance to be compared with the radiative transfer simulations.

The CPL instrument provides the data on the cloud morphology, i.e. cloud bottom/top as well as the cloud optical depths and extinction coefficients.

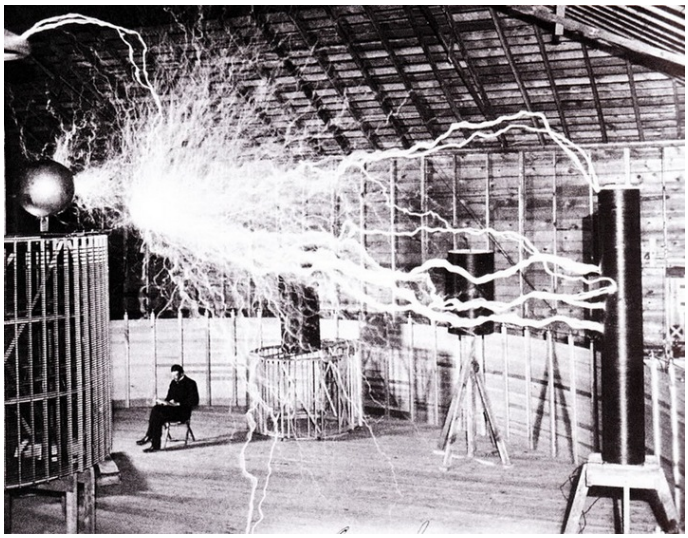

Figure 3.1: Publicity photo of N. Tesla and his magnifying transmitter high voltage generator (Colorado Springs, 1899).

The Hawkeye instrument provides the in situ IWCs and the information on the crystals shapes. Hawkeye also calculates the extinction coefficients of cirrus particles as well as particle size distributions (PSDs). The NOAA Water instrument provides in situ IWCs, while UCATS and DLH provide water vapour concentrations.

3.1 The mini-DOAS Data

The mini-DOAS instrument (see subsection 2.1.1) provides spectral radiance in three different wavelengths interval, making use of three scanning telescopes. Two main strategies are adopted for the data collection in order to have accessible measurements on vertical profiling, and the software is set up in order to treat each telescope as an independent unit [118].

During level flights, the telescopes scan in elevation. In the case of the UV and visible, the angles are: zenith/direct sun, 1°, 0°, −0.5°, −1°, −1.5°, −2°, −2.5°, −3°, −4°, −7°, and −15°. The positive angles are collected looking upward with respect to the limb while the negative angles are collected looking downward from the limb direction. The near-IR telescope is moved using the following angles: zenith/direct sun, −0.5°, −1°, −1.5°, −2°, −2.5°, −3°, and −4°.

The zenith/direct sun spectra are collected turning the telescopes to 90° (i.e. zenith direction), and in this configuration direct sun measurements can be done. The radiation before entering the slit of the telescope encounters a diffuse plate (see section 2.1.1). The plate allows to collect photons from the 2π-upward direction. These measurements, called solar references, are fundamental for the DOAS method because they provide the spectral radiance of the solar spectrum, but they differ from it because they are collected within the atmosphere at a certain altitude and not at the top of the atmosphere. Therefore, they carry some residual absorption features since, even if the concentration of air decreases in function of the altitude, some molecules are present above the detector causing slight absorptions within the solar spectrum.

During the GH ascents and descents the telescopes are pointed to −0.5° elevation. This small deviation from the horizon is chosen in order to compensate for the Earth's curvature, and to provide observations which are more reflective of the flight altitude.

The integrated measurement time for each angle in the UV and visible is set to 30 seconds, while 60 seconds is used in the near-IR. The solar reference, for each telescope, is collected during each flight with an integration time longer than 3 minutes. The collection of this measurement is chosen according to the flight plan, selecting the lower solar zenith angle (SZA) and the smaller solar azimuth relative to the aircraft angle (SRAA) which decreases the chance of reflection from the fuselage.

3.1.1 Spectrometer Wavelength Calibration

The collected spectra are spectral radiance (binary units that are proportional to the number of received photons) as function of detector pixels, since they are collected using a grating spectrometer. As a first step, it is necessary to map the pixels into wavelengths. The number of pixels is 1044 in the case of UV and visible spectral intervals, while in the near-IR range the total amount of pixels is 512. In the case of the UV and visible spectra, the mapping is done using some standard references as lamps (e.g., Hg, Kr or Ar) or a solar spectrum.

The solar spectrum involved in the mapping procedure is the *Kurucz et al.* [68], while the lamp spectra are collected before each flight and they are the mercury lamp for the UV range, the krypton lamp for the visible range and the argon lamp for the near-IR range. They are shown in Fig.3.2 for SF2-2013.

The basic idea in the wavelengths calibration is to use high-resolved lamp spectra or a high-resolved solar spectrum in order to identify the transition lines which account for a specific peak in the collected lamp spectrum [98]. They can be single, double or triple lines but they show up just like one peak because of the resolution of the instrument. From theoretical calculations the transitions occurring for a specific element as a function of the wavelengths are known, therefore it is possible to map with a polynomial the position of the wavelengths with respect to the pixels and finally to calibrate the

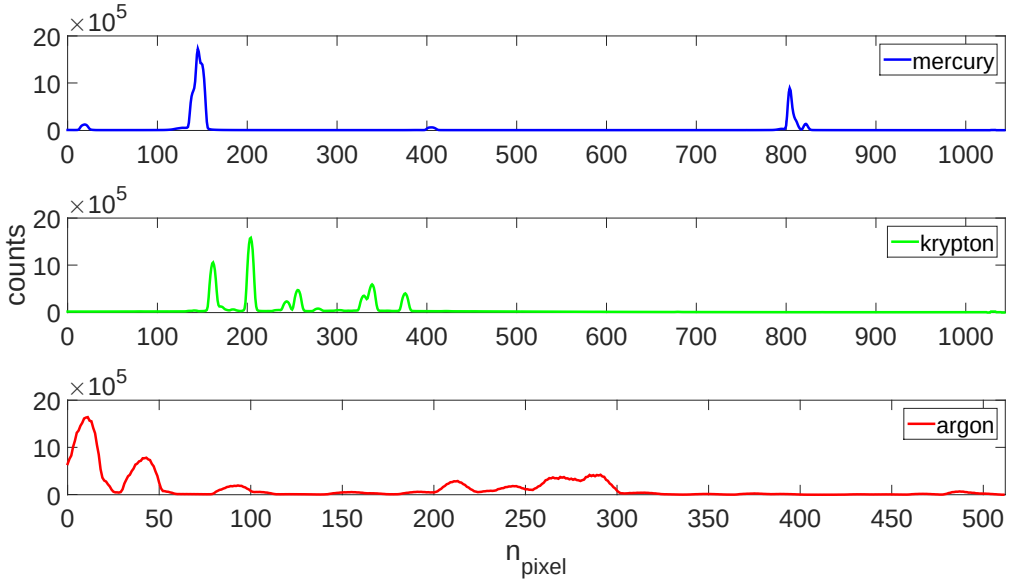

Figure 3.2: Lamp spectra from SF2-2013. The mercury lamp (upper panel) is used in the UV interval calibration, the krypton lamp (middle panel) in the visible interval and the argon lamp (lower panel) for the near-IR interval. All spectra are corrected for dark current and offset voltage.

spectra. The list of lines are tabulated by NIST[1] (National Institute of Standards and Technologies).

For the near-IR, the spectral calibration is not trivially possible since the spectral resolution is too coarse to properly assign the different argon lines. Therefore, the spectral wavelengths mapping is done directly comparing one collected spectrum and the relative simulation, identifying the absorption features of oxygen, water vapour and carbon dioxide.

The polynomial of third degree found as dispersion function is

$$\lambda[nm] = 901.28 + 1.66 \cdot n_{pixel} - 1.72 \times 10^4 \cdot n_{pixel}^2 + 1.31 \times 10^7 \cdot n_{pixel}^3 \qquad (3.1)$$

[1] http://physics.nist.gov/PhysRefData/ASD/lines_form.html

where n_{pixel} is the number of the pixel and λ the corresponding wavelength in nanometers. All the collected spectra during SF2-2013 are calibrated with this polynomial.

3.1.2 Dark Current and Offset Voltage

Before each flight, the dark current spectrum as well as the electronic offset voltage spectrum were collected for each spectrometer. In Fig.3.3 the spectra for dark current and offset voltage collected during SF2-2013 in the near-IR range are shown.

The dark current is an electric current that is present in the electronic devices even when no photons are illuminating the instrument. It consists of charges random generated in the depletion region of the detector due to thermal excitation. Keeping the temperature of the device stable and as low as possible helps to decrease the effect of this noise. Concerning the technical specifics of the detector used in the mini-DOAS instrument refer to the Hamamatsu[2] data sheet.

Dark current spectra were collected before each flight for all the telescopes with all the possible largest exposure times ($30000msec$ for the near-IR).

All the collected spectra are corrected for the dark current in order to avoid thermal random noise.

The offset voltage is internally added in order to avoid negative output voltages before the analog to digital conversion of the signal. It is present in each pixel and for every exposure time. Theoretically an electronic device has to measure a zero voltage when it is not illuminated by photons, but in practice a low voltage is present which is added to the signal detected and it depends on the type of the device and its composition. Itd random contribution, called offset, can be measured with the lower possible exposure time and adding sequentially lots of scans in order to identify better its signal with respect to other kind of contributions. Also for the electronic offset, for every flight the

[2] www.hamamatsu.com

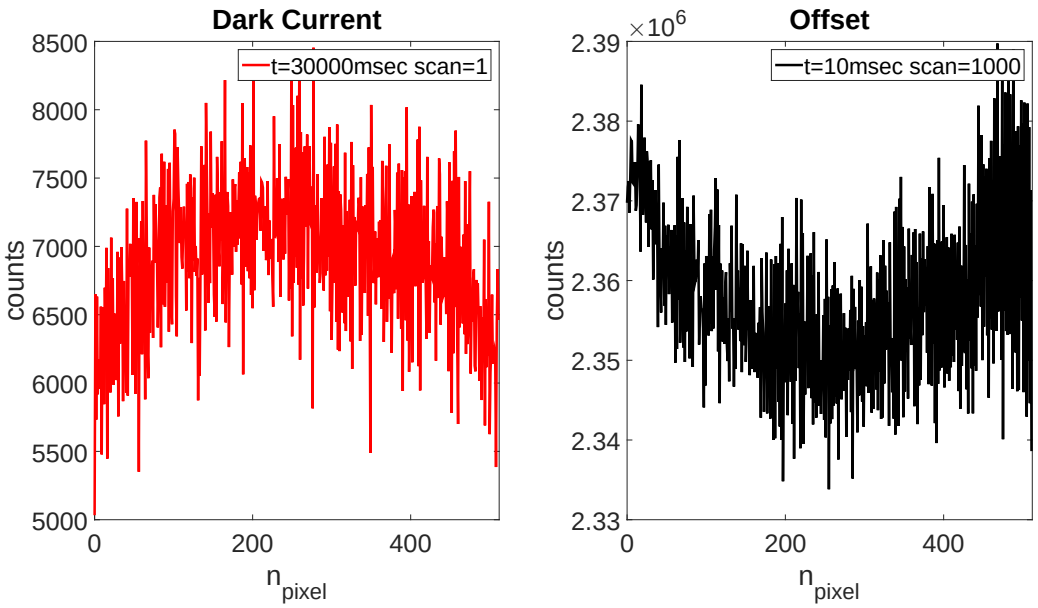

Figure 3.3: Dark current (left panel) and offset (right panel) spectra collected during SF2-2013 in the near-IR wavelengths range.

offset spectrum (for each telescope) was collected, and all the spectra are after corrected accounting for this effect.

In Fig.3.4 typical collected spectra in the near-IR range from SF2-2013 are shown. In the upper panel left (upper panel right) a collected spectrum in limb geometry (zenith geometry) is shown, while in the lower panel the optical depth as a function of the wavelengths is plotted. The absorption features caused by the molecules of water, oxygen and carbon dioxide as well as the absorption of ice particles are already recognizable. Specifically they are: the $2\nu + \delta$ and 2ν overtones of the symmetric water vapour stretch mode ($\sim 1130nm$ and $\sim 1380nm$, respectively); the ${}^1\Delta_g \leftarrow {}^3\Sigma_g^-$ for oxygen ($\sim 1270nm$); the $21^02 \leftarrow 00^00$ for carbon dioxide ($\sim 1590nm$); finally, the ice (particles) absorption occurring at $\sim 1490nm$.

Summarizing, all the collected spectra are corrected for the dark current and offset noises, they are calibrated in wavelengths, divided by the solar reference and finally the

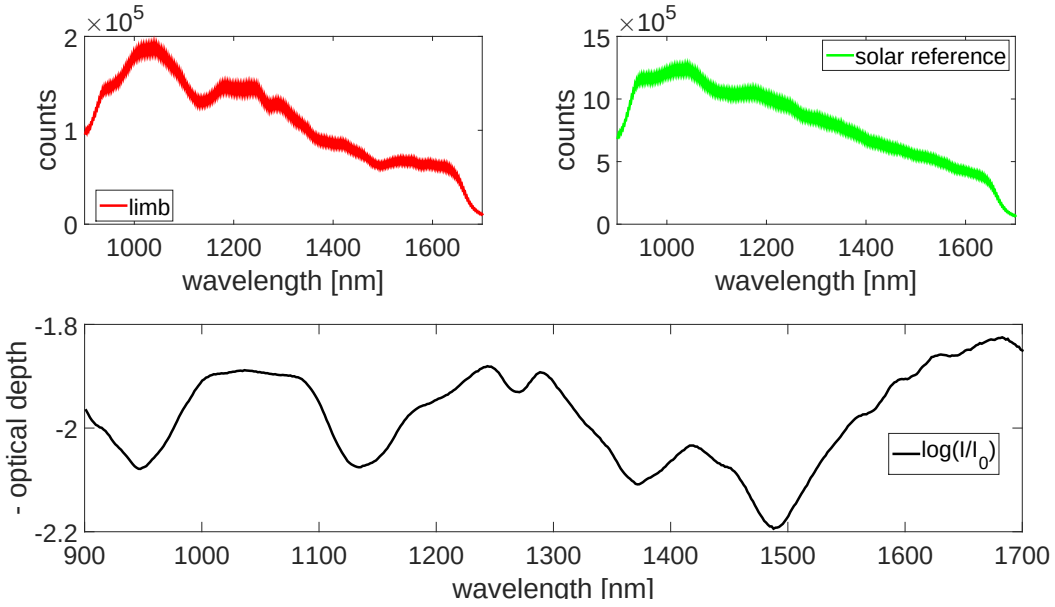

Figure 3.4: Samples of collected spectra in limb ($EA = -0.5°$) and zenith ($EA = 90°$) configurations (see the upper panels). In the lower panel: measured optical depths obtained from the upper spectra as $\log(I(EA = -0.5°)/I_0(EA = 90°))$.

measured optical depths are accessible for the direct analysis with the simulations.

3.2 The CPL Data

The Cloud Physics Lidar (CPL)[3] is an airborne lidar system designed specifically for studying clouds and aerosols. It is a non-scanning system and it looks fixed in nadir direction ($EA = -90°$), hence it is able to provide in situ vertical profiling measurements of cloud particles extinction coefficients as well as aerosols extinction profiles [18].
The CPL data products about the cloud physics information during the NASA ATTREX project can be directly downloaded from the instrument's web page (see footnote 3). They consist of:

i. cloud profiling with 30m vertical and 200m horizontal resolution at 1064nm,

[3] http://cpl.gsfc.nasa.gov/

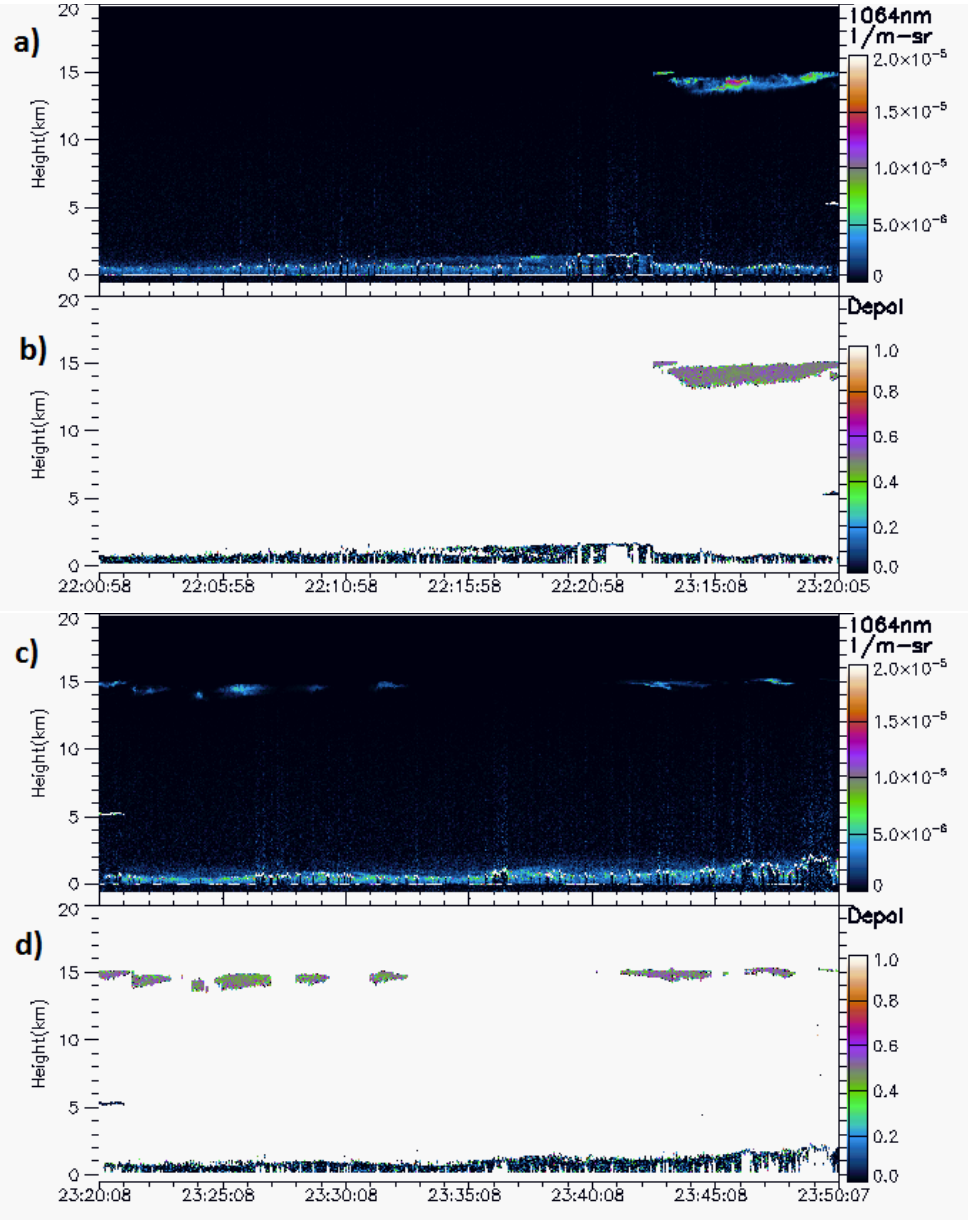

Figure 3.5: CPL data for a segment of flight SF2-2013. The plots show the altitude (km) as a function of the time (UTC). Panel a): attenuated backscatter coefficient at 1064nm (22:00-23:20 UTC). Panel b): depolarization ratio at 1064nm (22:00-23:20 UTC). Panel c): attenuated backscatter coefficient at 1064nm (23:20-23:50 UTC). Panel d): depolarization ratio at 1064nm (23:20-23:50 UTC). The height resolution is $\sim$ 30m.

532nm, and 355nm, providing cloud location and internal backscatter structure;

ii. aerosol, boundary layer, and smoke plume profiling at all three wavelengths;

iii. depolarization ratio to determine the phase (e.g. ice or liquid water) of clouds using the wavelength at 1064nm;

iv. cloud particle size determined from a multiple field-of-view measurement using the 532nm output (off-nadir multiple scattering detection);

v. direct determination of the optical depth of cirrus clouds (up to OD $\sim$ 3) using the 355nm channel.

In Fig.3.5 the CPL data collected during one segment (23:20-02:59 UTC) of flight SF2-2013 are shown.
The thin cirrus detected within the time interval 23:20-00:24 UTC is investigated in the present work.

3.3 The Hawkeye Data

The Hawkeye[4] instrument is developed by the SPEC Inc.[5] company, which started in 1979 as a consulting company and after expanded in research programs for cloud physics and relative instrumentations.
The instrument is a combination of two imaging instruments, a 2D Stereo probe and a Cloud Particle Imager [69], and a spectrometer equivalent to the Fast Cloud Droplet Probe [83].
During the NASA ATTREX missions, Hawkeye provided information about the ice

[4] http://www.specinc.com/hawkeye-combination-cloud-particle_probe
[5] http://www.specinc.com/home

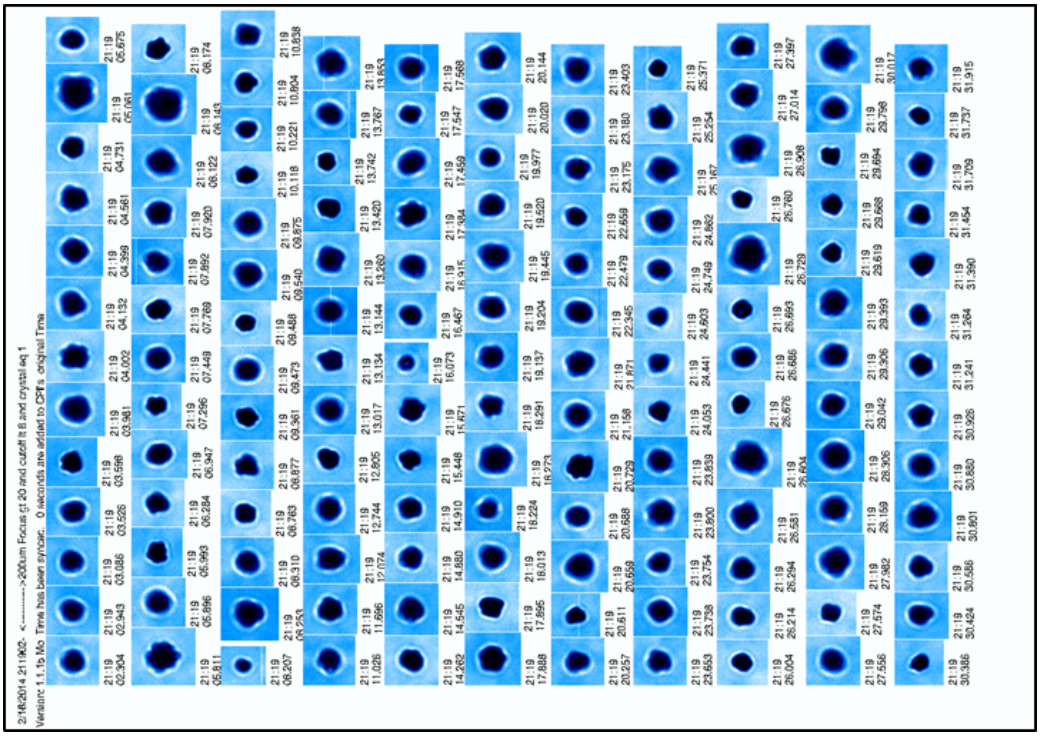

Figure 3.6: Examples of ice particles images provided by Hawkeye (T ~ 195K). Adapted from [59].

crystals habits and several other optical properties. Specifically the Hawkeye Fast Cloud Droplet Probe (FCDP) data[6] consist of

i. particles number concentrations;

ii. particles extinction coefficients (they are calculated assuming particles are spheres with the software version `ATTREX_FCDP_sp3cv11_SN01`);

iii. ice water contents (IWCs are calculated assuming all particles are spheres with density of $1.0[\mathrm{g/cm^3}]$);

iv. particle size distributions with particles radii in the interval $[0-50]\mu\mathrm{m}$.

[6] `https://espoarchive.nasa.gov/archive/browse/attrex/id2/GHawk`

The habits of particles mostly detected at a temperature of ~ 195K are spheroids particles, with particle size distributions peaked around $8-10\mu m$ [59], and small irregular particles which can not be classified with specific shapes. In Fig.3.6 typical particle habits from the ATTREX campaigns are shown. Also other shapes were found, but with lower probabilities ($< 3\%$) with respect to the spheroids or small irregular particles. These results, together with the earlier findings of [136, 6, 51] suggest that the low temperature cirrus particles in the TTL can be approximated by spheres and thus their optical properties are amenable to the Mie theory. Therefore, in order to setup properly the retrieval procedure, the description of ice crystals as spheres of equivalent mass can be considered a reasonable starting point.

3.4 The NOAA Water Data

The NOAA Water instrument [120] provides in situ measurements of water vapour concentrations and IWCs. The instrument measures water vapour (WV) and the enhanced total water (eTW). The total IWC (mixing ratios) is given by

$$IWC = \frac{(eTW - WP)}{AEF} \tag{3.2}$$

where AEF is the so-called aerosol enhancement factor [120]. The IWC mass ($[g/m^3]$) is calculated from the mixing ratios (Eq.3.2) using the measurements of temperature and pressure collected by the MMS instrument on board.
The resulting ice water content detection limit is $0.023-0.013ppm$ (i.e. $\sim 2\times10^{-6}[g/m^3]$), with an estimated overall uncertainty of 20%.

3.5 The UCATS and DLH Data

Within this work we make use of the water vapour concentrations data in order to explain the mini-DOAS inferred results. These data are provided by the UCATS

and DLH instruments on board the Global Hawk. These two instruments collect water vapour concentrations ([ppm]) as a function of time. The relative error on the measured water vapour mixing ratios is about 5% for both instruments.

4

Theory and Modeling

In this chapter the setup of the model is described and discussed.

First a brief description of the radiative tansfer equation and the radiative transfer model McArtim used for the spectral radiance simulations is provided.

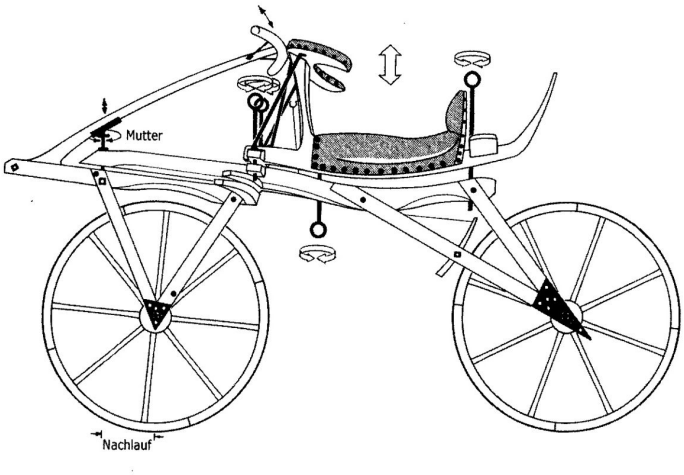

Figure 4.1: Baron Karl Drais' *Laufmaschine* (1819).

After, the setup of the whole atmosphere is described in terms of the specific quantities necessary to solve the radiative transfer equation: geometric coordinates, air parcels concentration profiles, the solar spectrum, and the ground albedo.

The next subsection discusses the absorption of the relevant molecules (O_2, CO_2, and H_2O) as well as the contribution of Rayleigh scattering. In the end, an extensive treatment about how cirrus cloud are represented in the radiative transfer model is given.

4.1 The Radiative Transfer Equation

The radiative transfer describes the energy transfer of electromagnetic radiation [15]. When the photons travel through a medium, their energy and direction change according to three processes that can occur: absorption, emission and scattering. The equation of radiative transfer describes these interactions mathematically.

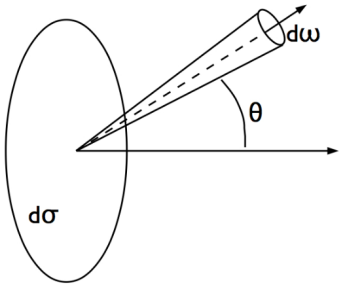

Figure 4.2: Sketch of the direction of the radiation.

The analysis of a radiation field crossing a medium starts considering the amount of the radiant energy dE_ν in a specific frequency interval $(\nu, \nu + d\nu)$ which is transported across an element of area $d\sigma$ and in directions confined to an element of solid angle $d\omega$, during a time dt (see Fig.4.2). This energy, dE_ν, is expressed in terms of the specific intensity, i.e. the spectral radiance I_ν, by

$$dE_\nu = I_\nu \cos\theta d\nu d\sigma d\omega dt \tag{4.1}$$

In a medium which absorbs, emits and scatters, the spectral radiance I_ν varies from point to point and also with direction through every point. Often the atmosphere, in radiative transfer analysis, is stratified in parallel planes in which all physical properties are invariant over a plane. Said that, we can start to consider the extinction caused by the atmospheric medium, in other terms the absorption and scattering processes.

When a photon crosses a medium, it is weakened by its interaction with matter. Traversing a thickness ds in the direction of propagation, changes the initial intensity I_ν of the radiation into $I_\nu + dI_\nu$ where

$$dI_\nu = -k_\nu \rho I_\nu ds \tag{4.2}$$

Here, ρ is the density of the medium and k_ν is the mass extinction coefficient. During the extinction process not all the energy is absorbed by the medium but a part of the energy

may reappear in other directions as scattered radiation. If we consider only scattering by a mass element of cross-section $d\sigma$ and thickness ds, i.e. $dm = \rho \cos\theta d\sigma ds$, the scattered energy rate is given by

$$\frac{dE_\nu}{dt} = k_\nu \rho ds \times I_\nu \cos\theta d\nu d\sigma d\omega \tag{4.3}$$

or, equivalently by $k_\nu I_\nu dm d\nu d\omega$. Since the scattering process is specified by an angular distribution, it is necessary to consider a 4π normalized phase function $p(\cos\Theta)$ in the previous formula, such that the energy rate becomes

$$\frac{dE_\nu}{dt} = k_\nu I_\nu p(\cos\Theta)\frac{d\omega'}{4\pi} dm d\nu d\omega \tag{4.4}$$

which describes the energy being scattered into an element of solid angle $d\omega'$ and in the direction inclined at an angle Θ to the direction of incident radiation. According to Eq.4.4 the loss of energy due to scattering processes can be evaluated in all directions performing an integration over the entire solid angle

$$\frac{dE_\nu}{dt} = k_\nu I_\nu dm d\nu d\omega \int p(\cos\Theta)\frac{d\omega'}{4\pi} \tag{4.5}$$

By linking Eq.4.3 and Eq.4.5, we infer that they agree only if the phase function is normalized to unity

$$\int p(\cos\Theta)\frac{d\omega'}{4\pi} = 1 \tag{4.6}$$

Considering now also the absorption and not only the scattering, it is possible to write the same Eq.4.5, but in this case the contribution coming from scattering must be less than 1, in other terms

$$\int p(\cos\Theta)\frac{d\omega'}{4\pi} = \varpi_0 \leq 1 \tag{4.7}$$

where ϖ_0 is the single scattering albedo (SSA) and indicates the fraction of the energy loss due to pure scattering.

In general the phase function can be expanded as a series of Legendre polynomials of the form

$$p(\cos\Theta) = \sum_{l=0}^{\infty} \varpi_l P_l(\cos\Theta) \tag{4.8}$$

where the ϖ_l's are constants.

After having considered the absorption and scattering processes of the radiation within a medium, it is necessary to consider now the contribution of emission. We can introduce the emission coefficient j_ν and define the amount of energy emitted in the frequency interval $(\nu, \nu + d\nu)$ at the time dt in the direction $d\omega$ by the mass element dm, as

$$dE_\nu = j_\nu dm d\omega d\nu dt \tag{4.9}$$

If scattering effects are already present in the medium, then there will be a contribution to the emission coefficient from the scattering of radiation happening in all other directions. In other terms, considering the direction of the scattering event (θ', ϕ') which contributes to the emission process occurring in the (θ, ϕ) direction, according to Eq.4.4, we have

$$\frac{dE_\nu}{dt} = k_\nu dm d\nu d\omega p(\theta, \phi; \theta', \phi') I_\nu(\theta', \phi') \frac{\sin\theta' d\theta' d\phi'}{4\pi} \tag{4.10}$$

Therefore the contribution to the emission coefficient performed by scattering processes $j_\nu^{(s)}$ can be expressed as

$$j_\nu^{(s)} = k_\nu \frac{1}{4\pi} \int_0^\pi \int_0^{2\pi} p(\theta, \phi; \theta', \phi') I_\nu(\theta', \phi') \sin\theta' d\theta' d\phi' \tag{4.11}$$

If the emission coefficient consists only of the contribution of scattering events, i.e. $j_\nu \equiv j_\nu^{(s)}$, the medium is called a pure scattering atmosphere, but still absorption processes may happen since the single scattering albedo can be smaller than the unity.

A case which is somehow opposite to the scattering atmosphere is the case of a medium in local thermodynamic equilibrium. In this case it is possible to define for each point

within the medium a local temperature T such that the emission coefficient is given in terms of the absorption coefficient, using Kirchhoff's law

$$j_\nu = k_\nu B_\nu(T) \tag{4.12}$$

where

$$B_\nu(T) = \frac{2h\nu^3}{c^2}\frac{1}{e^{h\nu/kT}-1} \tag{4.13}$$

is the Planck function, h is the Planck constant and k is the Boltzmann constant. Eq.4.12 essentially defines the parcels composing the atmosphere as black bodies with a certain temperature T; according to their capacity of absorbing radiation, given by k_ν, they are able to re-emit the absorbed energy as black bodies and therefore diffuse the radiation around according to the Planck function (Eq.4.13).

In the end, the ratio of the emission to the absorption coefficient defines the source function, i.e. $\mathcal{F}_\nu = j_\nu/k_\nu$, which in the case of pure scattering atmosphere (see Eq.4.11) is given by

$$\mathcal{F}_\nu = \frac{1}{4\pi}\int_0^\pi\int_0^{2\pi} p(\theta,\phi;\theta',\phi')I_\nu(\theta',\phi')\sin\theta' d\theta' d\phi' \tag{4.14}$$

and in the case of local thermodynamic equilibrium is equivalent to the Planck function (Eq.4.13)

$$\mathcal{F}_\nu = B_\nu(T) \tag{4.15}$$

Now, in order to derive the fundamental equation which governs the attenuation of the radiation in a medium, the so called radiative transfer equation (RTE), we have to consider a small cylindrical element of area $d\sigma$ and height ds; then the attenuated energy in the frequency interval $(\nu, \nu + d\nu)$ crossing the two cylinder faces normally, in the time dt and confined to a solid angle element $d\omega$, is given by

$$\frac{dI_\nu}{ds} ds d\nu d\sigma d\omega dt \tag{4.16}$$

Within the cylinder a part of the energy is absorbed according to Eq.4.3 and a part is emitted, see Eq.4.9. Finally, counting the gains and losses in the energy budget of the radiation, we end up with

$$\frac{dI_\nu}{ds} = -k_\nu \rho I_\nu + j_\nu \rho \tag{4.17}$$

that, as a function of the source function $\mathcal{F}_\nu$, provides the final form of the radiative transfer equation within the atmosphere

$$-\frac{dI_\nu}{k_\nu \rho ds} = I_\nu - \mathcal{F}_\nu \tag{4.18}$$

4.2 The McArtim Radiative Transfer Model

The radiative transfer model McArtim (Monte carlo Atmospheric radiative transfer inversion model) was developed in order to support the interpretation of spectroscopic data collected in remote sensing applications [20]. It is a forward model in the context of mathematical inversion and within this work it is used for spectral radiance calculations. In fact, by measuring the absorption of species with known atmospheric concentrations (e.g. oxygen in the near-IR region), optical properties of the atmosphere and its constituents (e.g. cloud particles) can be inferred [98].

The model solves a set of linear or non-linear equations [103], that link the information coming from the measurements $(\mathbf{y})$ to the information assembled in the so called *state vector* $(\mathbf{x})$, that represents the unknown quantities to be retrieved

$$\mathbf{y} = \mathbf{F}(\mathbf{x}) \tag{4.19}$$

the $\mathbf{F}(\mathbf{x})$ is the so called *forward model*. This function encapsulates the understanding of the physics of the measurement. In order to set up a good forward model it is fundamental to properly describe the device involved in the data collection, and to properly understand the relations linking the collected data and the quantities that have to be

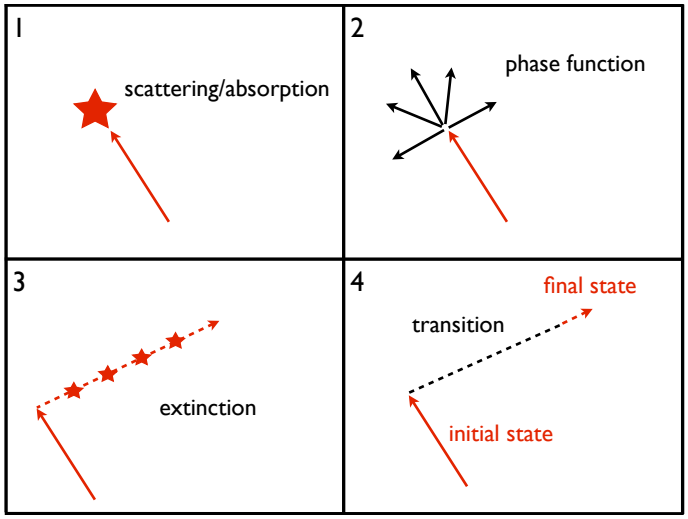

Figure 4.3: Sketch of the Monte Carlo raytracing method.

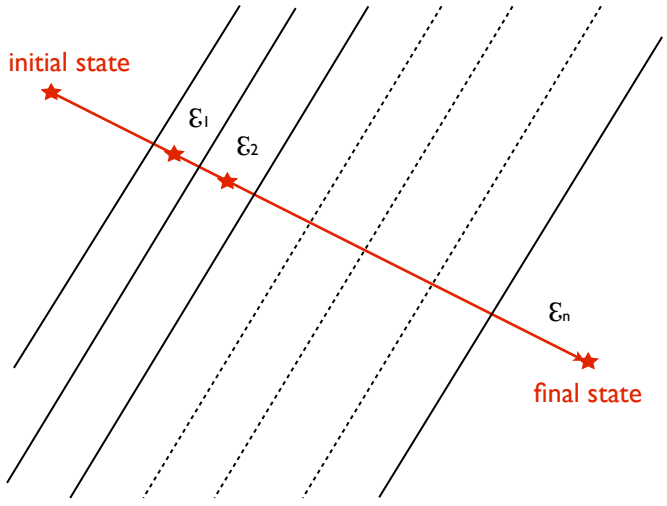

Figure 4.4: Sketch of the photon trajectory. The red stars highlight the extinction processes encountered by the photon.

retrieved (for a full description of the inverse problem solutions and methods refer to [103, 119]). In our case the equation to be solved is the radiative transfer equation (see Eq.4.18), discarding the term due to thermal emission. The McArtim model solves the radiative transfer equation via a backward Monte Carlo algorithm and the photons forming the radiation are treated independently. Consequently, the obtained solution is valid only in certain regimes where the wavelength of the radiation is much smaller than the photon free path.

The simulation starts with a certain amount of photons for each wavelength and ends providing the total amount of photons which survived traveling through the atmosphere. The Monte Carlo algorithm is a statistical process, so it is subjected to statistical noise; thus increasing the number of photons (N) translates to a decrease of the relative Poisson noise ($1/\sqrt{N}$), finally providing more accuracy to the results. On the other hand, increasing the number of photons increases the required computing

power, so it is necessary to find a compromise in between these two contrasting effects (see subsection 4.2.1 for the sensitivity studies).

The basic idea behind the Monte Carlo radiative transfer model is that each single photon performs a transition from an initial state to a final state (see Fig.4.4). During this transition two steps happen. First, there is a scatter event governed by a single scattering albedo, which accounts for all the contributions coming from molecules and particles. It can be interpreted as the probability of a photon to survive an absorption event. Second, according to the scattering process, it has to be considered the final direction of the photon expressed by the phase function. In this context, it is possible to build a probability density function of free paths length according to the total extinction of the medium, and subdivide the whole photon path trajectory in steps of free path lengths; finally in each step the extinction probability is considered.

In Fig.4.3 a sketch of the whole statistical process is shown. At the beginning (panel 1), the photon undergoes an extinction process and it has a certain probability to survive it (defined by the SSA); after, the algorithm selects the new photon direction according to the phase function. Hence, how far it can travel is characterized by the extinction along the path. Essentially the raytracer subdivides the medium into n-segments according to the spatial grid provided by the user and calculates the extinction of the medium in each segment (see Fig.4.4). Thus, when the photon enters one step-path it undergoes an extinction process which determines the prosecution of its trajectory in the next step-path. Finally in the fourth panel of Fig.4.3 the total transition, incorporating all these effects, ends with the final state reached by the photon.

The type of view direction that is selected for this work is the detector relative trajectory. This is essentially a backward trajectory, therefore the photon starts from the detector and travels through the atmosphere until it escapes from it. Passing through the medium it encounters all the extinction processes described above.

4.2.1 Photon Number Dependence

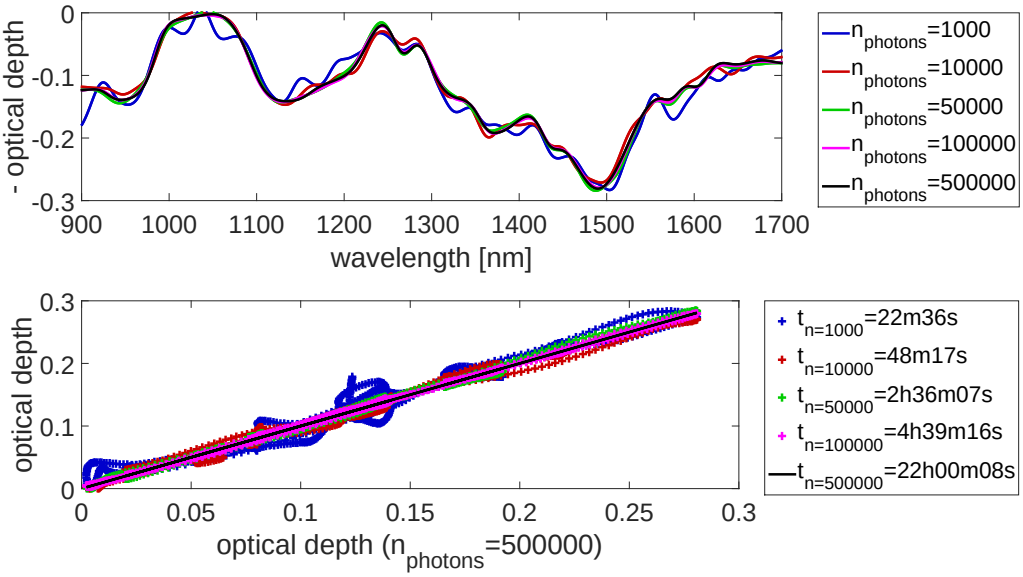

Figure 4.5: Upper panel: RTM simulations ($\log(I_{ext}/I_{sca})$) with different amount of photons in the initial state for each wavelength are shown. The assumed cloud optical depth is 0.48. Lower panel: the optical depths for each simulation are plotted against the simulation at higher spectral resolution (i.e. $n_{photons} = 5 \times 10^5$), in order to investigate the effect of random noise. The amount of photon used as well as the time necessary to provide the spectral radiance are shown in the legend. The indicated computing times are for 7 CPU running in parallel with a processor Intel(R) Core(TM) i7-4770 CPU @ 3.40Ghz.

In the radiative transfer model, the incoming radiation is described by a certain amount of photons. Varying the number of photons translates into a change of the precision for the simulated spectral radiance. In fact, the processes implemented in the Monte Carlo model are subjected to Poisson noise and in order to achieve high accuracy, it is necessary to increment the photon number. This translates into big time-consuming efforts for the calculations.

The sensitivity runs of the simulated spectral radiance as a function of photon number

Table 4.1: Photon number and mean relative error of the simulated spectral radiance.

Photon Number	Mean Relative Error
10^3	7.7%
10^4	2.8%
5×10^4	1.3%
10^5	0.9%
5×10^5	0.4%

are shown in Fig.4.5. Table 4.1 reports the mean relative errors of the simulated spectral radiance when a specific number of photons is run for each wavelength.

Since the relative error associated to the measurements is 3% [118], we adopt to run 10^5 photons for each wavelength in order to reduce the impact of the RTM uncertainty on the accuracy of the retrieval procedure.

4.3 The Detector

In the radiative transfer model the telescope's field of view (FOV) is accounted according to the instrumental characteristics of the mini-DOAS (see section 2.1.1 for more details).

Optically the telescope views a rectangle in the sky that is $\sim 0.25°$ in elevation and $\sim 1°$ in the azimuth direction [118]. Instead of using a constant rectangular field of view, a more realistic representation for the FOV in the RTM is a Gaussian function

$$f(x) = \frac{1}{\sigma\sqrt{2\pi}} \exp\left(-\frac{x^2}{2\sigma^2}\right) \tag{4.20}$$

Where a standard deviation of $\sigma = 0.1285°$ ($\sigma = 1.118°$) is selected for the vertical (azimuth) direction and x is the angle in degrees. In Fig.4.6 the vertical FOV of the detector is shown. The red sector highlights the constant FOV of $\sim 0.25°$ in elevation and the Gaussian function (in green) represents more realistically the slit of the instrument, where statistically the detector can collect photons coming from directions apart from

the constant rectangular slit.

Concerning the spectral resolution of the instrument, a Gaussian function ($\sigma = 10nm$) is applied to the simulated spectral radiance, in order to account for the instrument slit function (ISF). In fact, the radiative transfer model provides the radiance calculations at high resolution, while the measured radiances were collected with a low-resolution instrument, therefore in order to compare measured and simulated spectra it is required to convolve the high-resolved simulated spectra with the instrument resolution.

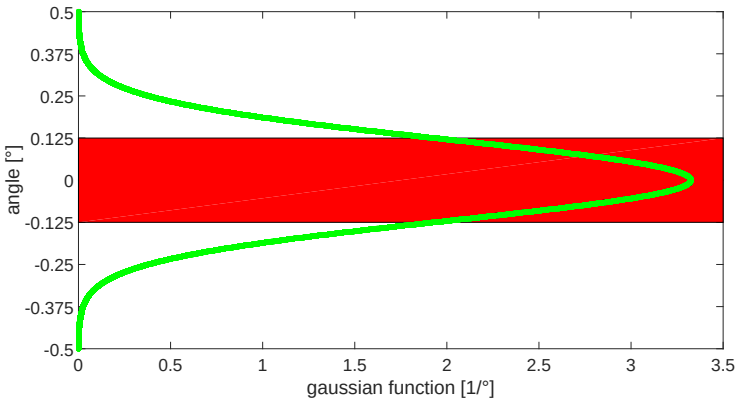

Figure 4.6: Modeling of the vertical field of view for the mini-DOAS instrument.

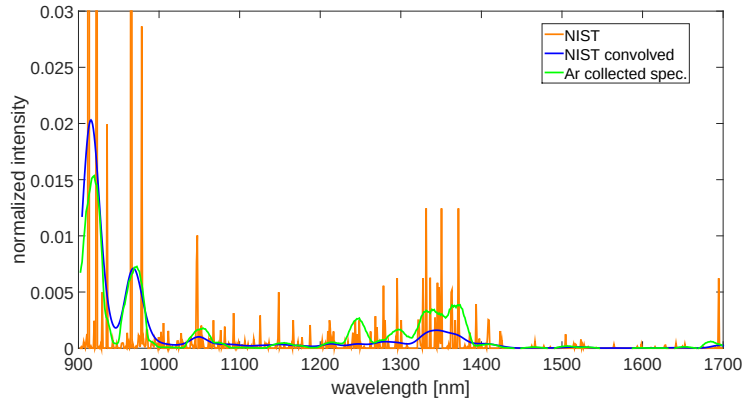

Figure 4.7: Argon spectra: in orange (blue) the NIST high-resolved (NIST convolved with a Gaussian function) spectrum is shown. In green the mini-DOAS collected spectrum is shown.

The common procedure in the differential optical absorption spectroscopy (DOAS) is to make use of the low-resolved lamp spectrum of an element (e.g. argon in the near-IR). By comparing the low-resolved spectrum with the known spectral transitions occurring

within the frequency range it is possible to infer the convolution function. For example, one transition line appears like a delta function with a high-resolution instrument while, with a low-resolution instrument, its image appears at a coarser spectral resolution like a Gaussian-type shape (or also other function-type shapes). For the near-IR wavelengths interval it is used the collected argon spectrum (shown in Fig.4.7 in green), and the spectral lines at high resolution for the argon element can be downloaded from an open source database such as NIST[1] (the spectrum is shown in Fig.4.7 in orange). It is arguable that in the argon collected spectrum, the number of lines forming a single broad peak can be more than one. Further, since the relative intensities are temperature dependent, if the high-resolved spectrum is not known at the same temperature of the collected one it becomes complicated to infer correctly the ISF. To overcome this issue, we decide to convolve the simulated spectral radiance with a Gaussian function with a standard deviation of $10nm$ which approximates the spectral resolution of the instrument. The convolved NIST spectrum obtained using this Gaussian function is shown in Fig.4.7 (blue). It is clear that the convolved NIST spectrum only approximates the peak heights of the measured spectrum, but the peak widths are reasonably reproduced.

Within this work all the simulations are convolved with this Gaussian function. The impact of the ISF on the high-resolved simulated spectral radiance for clear skies is shown in Fig.4.20. In the upper panel two simulations at high resolution are plotted and in the lower panel the relative convolved simulated spectra are shown.

4.4 Setup of the Atmosphere

The atmosphere is built using a 1 dimensional model (1D) which allows to change the concentrations of gases and particles along the z-axes, in other terms it is possible

[1] http://physics.nist.gov/PhysRefData/ASD/lines_form.html

to provide each profile as a function of the altitude. The 1D model builds the whole atmosphere as homogeneous parallel planes where the information about the concentrations are provided via altitude-profiles. The selected altitude grid ranges from the sea level (i.e., 0 km) up to 60 km, with different steps within this range. We select a $1\mathrm{km}$ step from 0 to $12\mathrm{km}$, a $0.1\mathrm{km}$ step from $12\mathrm{km}$ to $20\mathrm{km}$, a $1\mathrm{km}$ step from $20\mathrm{km}$ up to $60\mathrm{km}$. The altitude discretization is chosen to reflect best the investigated atmospheric layers, i.e. the TTL where the GH flew.

Modeling the atmosphere in the near-IR wavelength range ($[900-1700]\mathrm{nm}$) requires to consider the gases absorptions of water vapour ($2\nu+\delta$ at $\sim 1130\mathrm{nm}$ and 2ν at $\sim 1380\mathrm{nm}$), oxygen (${}^1\Delta_g \leftarrow {}^3\Sigma_g^-$ at $\sim 1270\mathrm{nm}$) and carbon dioxide ($21^02 \leftarrow 00^00$ at $\sim 1590\mathrm{nm}$) in the radiative transfer process.

Clouds are built-in as *blocks* containing all the optical properties of ice particles treated as an ensemble. In other terms, within the cloud altitude-profile, it is possible to change the vertical extension of the cloud (bottom and top layers). The model treats the cloud as an infinite horizontal homogeneous cloud described by specific optical properties which are: the extinction coefficient ($\epsilon_{ext}[\mathrm{km}^{-1}]$, see Eq.4.86), the single scattering albedo (ϖ_0, see Eq.4.83), defined as the ratio of scattering efficiency to total extinction efficiency, and the asymmetry parameter (g, see Eq.4.84), defined as the average cosine of the scattering angle. Not only one cirrus can be implemented in the model, but the user can also create multiple layers clouds, providing for each cloud layer specific optical properties and location, as well as superimposed layer clouds with different optical properties but, in this case, same location.

4.4.1 Geometric Coordinates

The mini-DOAS measurements were all collected at specific points in time and space, therefore each spectrum provides the exact geolocation to the radiative transfer model.

To setup the model, the information regarding the position of the detector and the sun are extracted from each collected spectrum. In Table 4.2 the geometric coordinates need for the simulations are listed.

Table 4.2: Geometric coordinates for the 1D RTM simulations.

Coordinate	**Abbreviation**
Altitude [km]	Alt
Colatitude [°]	CoLat
Longitude [°]	Long
Solar zenith angle [°]	SZA
Solar relative azimuth angle [°]	SRAA
Elevation angle [°]	EA

Briefly they are:

i. the altitude of the detector expressed in km over the sea level;

ii. the colatitude of the aircraft which goes from 0° at the north pole to 180° at the south pole;

iii. the longitude of the GH position is evaluated from 0° to 180° counterclockwise in the east direction and from 0° to −180° clockwise in the west direction;

iv. the solar zenith angle, i.e. the angle defining the sun position with respect to the zenith;

v. the solar relative azimuth angle, which accounts for the different heading of the aircraft relative to sun's azimuth; it is evaluated taking the difference between the absolute azimuth of the aircraft and the absolute azimuth of the sun;

vi. the elevation angle which accounts for the different viewing direction of the detector with respect to the horizon (placed at 0°).

4.4.2 Trace Gases Profiles

In order to provide good *a priori* information to the model, the temperature, pressure, and water vapour profiles are selected from a climatological data base of tropical regions [2]. The oxygen concentration profile is calculated using the temperature and pressure profiles and a fixed mixing ratio of 20.95%. Starting with the ideal gas law

$$PV = N_{air}kT \tag{4.21}$$

where P is the pressure, V the volume, N_{air} the number of air parcels, k the Boltzmann constant and T the temperature, it follows

$$\frac{N_{gas}}{V} = \frac{MR_{gas}P}{kT} \tag{4.22}$$

where $MR_{gas} = N_{gas}/N_{air}$ is the gas mixing ratio and N_{gas} is the number density of the gas, i.e. the concentration. In the same way the carbon dioxide profile is calculated

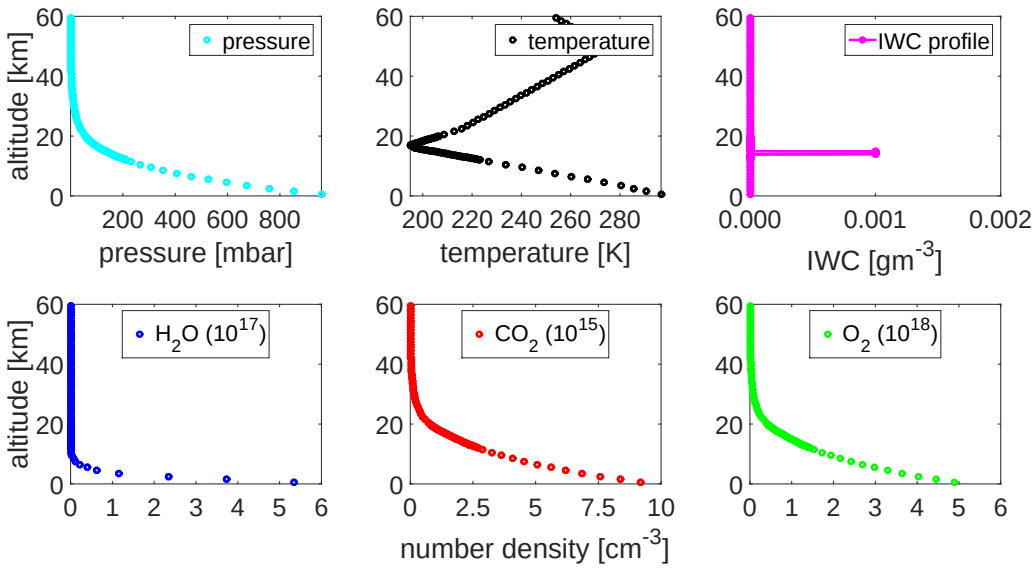

Figure 4.8: In the upper panels: pressure (left) and temperature (middle) profiles, and an example of a cirrus cloud (right). In the lower panels: water vapour (left), carbon dioxide (middle) and oxygen (right) concentration profiles.

using a fixed mixing ratio of 393ppm [88].

The optical properties of the cirrus cloud are assumed to be homogeneous and infinite in a certain altitude layer.

As explained in the following sections, the optical properties of ice particles are parameterized as a function of ice water content.

Fig.4.8 shows the altitude profiles involved in the radiative transfer calculations. The optical properties of the cirrus are chosen so that the cloud has no particles for the whole altitude range except for the layer placed between 13.9km and 14.9km where the density of ice particles is fixed to $10^{-3}[gm^{-3}]$ as an example.

4.4.3 Solar Spectrum

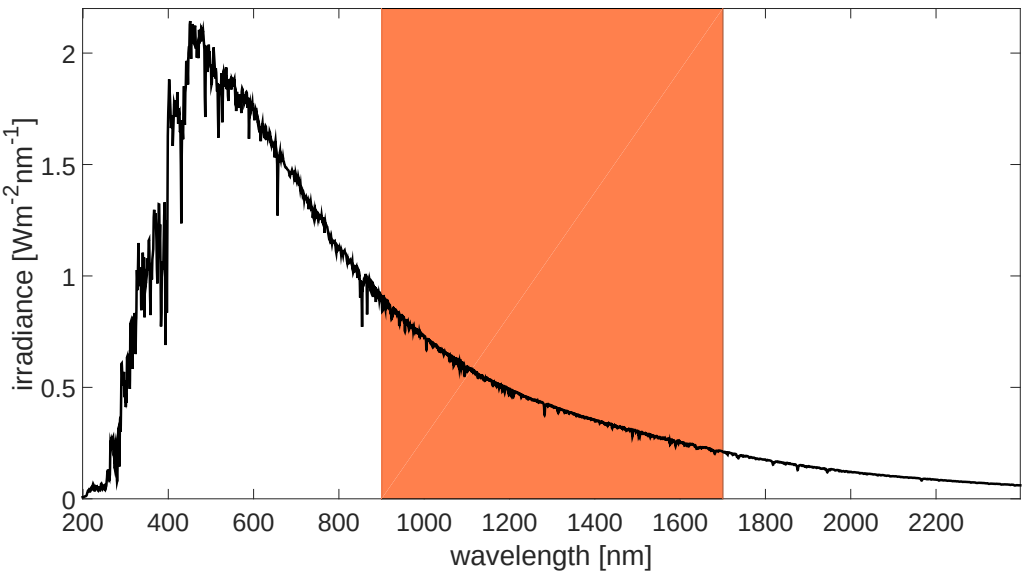

Figure 4.9: Solar irradiance spectrum from [121]. The orange sector highlights the near-IR wavelengths interval analyzed within this work.

The solar irradiance spectrum is obtained from *Thuillier et al.* [121], and it is shown in Fig.4.9. All the simulated spectral radiance are normalized with respect to

this solar spectrum.

The season dependent Earth-Sun distance is also accounted for in the radiative transfer model.

4.4.4 Ocean Surface Albedo

The Earth's surface albedo is a non-dimensional quantity which indicates how well the Earth's surface reflects solar energy. It is defined as

$$\begin{aligned} A &= \frac{\pi \cdot I(\lambda, \theta, \phi)}{E(\lambda)} \\ &= \frac{1}{E(\lambda)} \int_0^{2\pi} \int_0^{\pi/2} \rho_{E,\lambda}(\theta, \phi, \theta', \phi') I_{surface}(\lambda, \theta', \phi') \sin(\theta') d\theta' d\phi' \end{aligned} \tag{4.23}$$

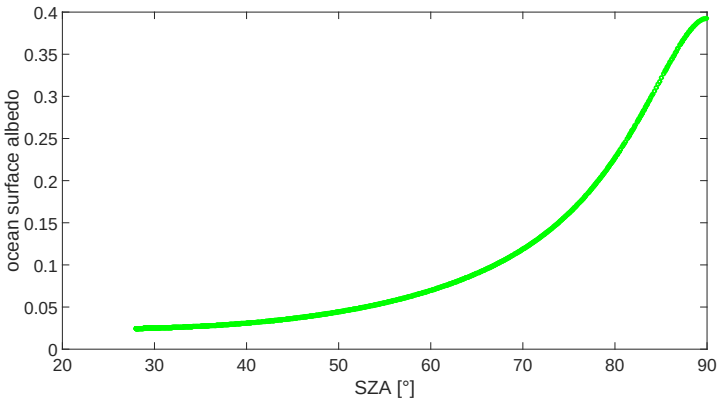

Figure 4.10: Ocean surface albedo as a function of the solar zenith angle [104]. Here, typical values for the SZA derived from SF2 – 2013 are plotted.

where $I(\lambda, \theta, \phi)$ is the upwelling radiance from the ground and $E(\lambda)$ is the downwelling irradiance. $\rho_{E,\lambda}(\theta, \phi)$ is the bi-directional reflection function.

The ground albedo varies between 0 and 1. Commonly a 0 albedo surface describes *black* surfaces, i.e. surfaces which can absorb all the incoming radiation while an albedo of 1 refers to *white* surfaces. All over the Earth, the surface changes due to different compositions like sea ocean, desert dust, vegetation, sea ice, urban clusters and so on.

Within the NASA ATTREX project, all the science flights were performed on the eastern and western pacific zones (see Table 2.3 and Fig.2.5 for more details), consequently

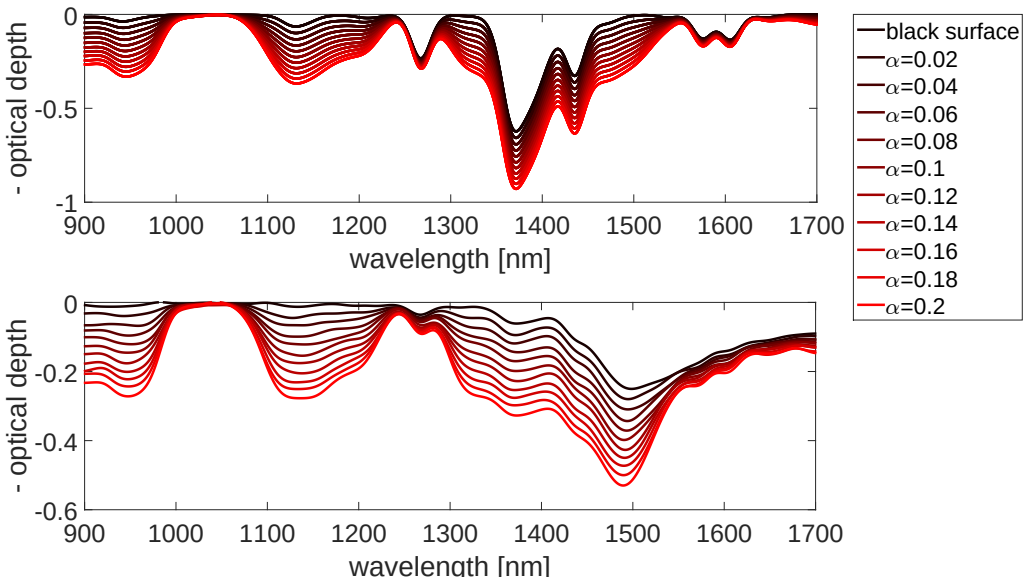

Figure 4.11: Ocean surface albedo simulations in clear sky (upper panel) and cloudy (lower panel) conditions. For the cloudy case a vertical optical depth of ~ 1 is used. The detector is located within the cirrus ($EA = -0.5$).

an ocean surface albedo is considered. A typical ocean albedo is approximately 0.06 but the ground albedo, besides having a wavelength dependency, could vary with the solar zenith angle, the wind speed on the surface level, cloud or aerosol covering and ocean chlorophyll concentration [60]. For water surfaces, the spectral albedo in the visible and near-infrared regions differs only slightly. Therefore the dependency on wavelength can be neglected, but it has a strong dependency in terms of the solar zenith angle. As shown in [104], the ocean surface albedo A_μ for the direct beam, under clear sky conditions, can be parameterized as a function of the solar zenith angle, such that

$$A_\mu = \frac{0.026}{\mu^{1.7} + 0.065} + 0.15(\mu - 0.1) \cdot (\mu - 0.5) \cdot (\mu - 1.0) \tag{4.24}$$

where $\mu = \cos(SZA)$ is the cosine of the solar zenith angle. The results for this parameterization are shown in Fig.4.10.

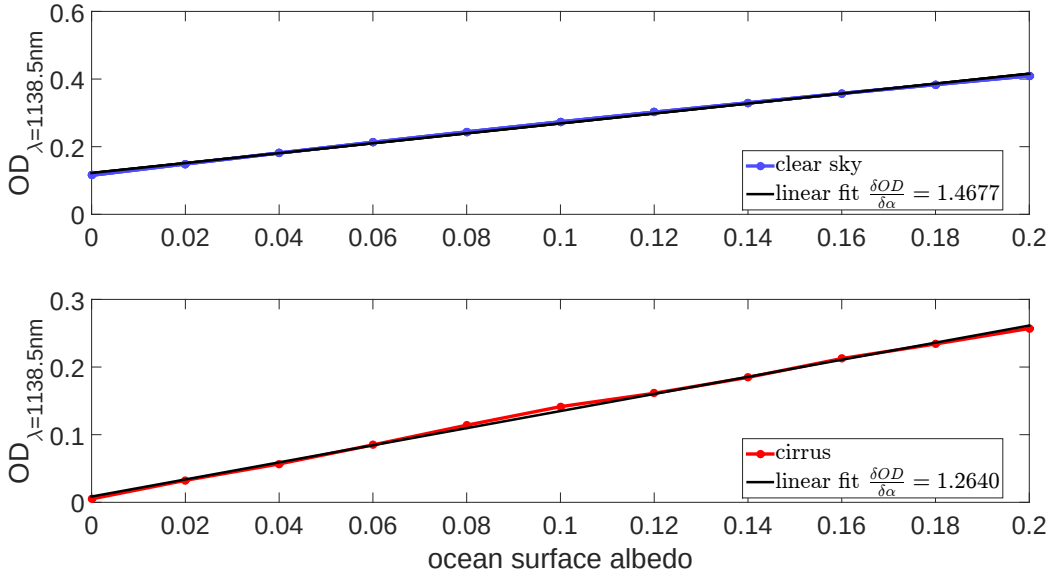

Figure 4.12: Variations of the optical depth ($\lambda = 1138.5nm$, H_2O absorption band) as a function of the ocean surface albedo in clear sky (upper panel) and cloud (lower panel) conditions. A linear fit is applied on the results for the simulated optical depths; the angular coefficients are reported in the legends.

As demonstrated in [60], the wind effect on albedo for clear skies is more significant for large SZA. Therefore, the SZA dependence is only taken into account, since the direct analysis on the collected spectra involved mostly solar zenith angle ranged between 30 and 60 degrees. As generally done in general circulation models (GCMs) the concentration of the chlorophyll can be assumed of $0.2mg/m^3$, which is about the average for the global ocean and therefore it can be neglected in ocean surface albedo parameterizations.

Some sensitivity studies are conducted in order to investigate the impact of the ground albedo on the simulated spectral radiance. These results are shown in Fig.4.11 for clear sky (upper panel) and cloudy (lower panel) conditions. When the ground albedo increases, more photons are reflected thus the absorption of H_2O, CO_2, and O_2 in the

lower atmosphere relatively contributes to the total absorption observed in limb. The same process occurs in presence of a cirrus cloud. In this case, due to the presence of particles scattering, the ground albedo effect on the molecular absorption band is less strong with respect to the clear sky case, as shown in Fig.4.12. This is a consequence of the different contribution of Rayleigh and Mie scattering to the total absorption observed in limb.

4.5 Molecular Extinction

4.5.1 Molecular Absorption

The molecular absorption cross-sections used in the radiative process are evaluated via the HITRAN database [106]. This database provides for each trace gas the spectral lines intensities S_{ij} (see Fig.4.13) as a function of the relative transition wavenumber $\nu_{ij} = E_i - E_j$ (cm^{-1}) at the reference temperature $T_{ref} = 296K$ and pressure $p_{ref} = 1atm$

$$S_{ij}(T_{ref}) = I_a \frac{A_{ij}}{8\pi c \nu_{ij}^2} \frac{g' e^{-c_2 E_i/T_{ref}}(1 - e^{c_2 \nu_{ij}/T_{ref}})}{Q(T_{ref})} \tag{4.25}$$

where A_{ij} (s^{-1}) is the Einstein coefficient for spontaneous emission, g' is the upper state statistical weight and E_i the lower state energy [112]. The constants involved in the calculations are the Planck constant h, the speed of light c and the Boltzmann constant k. The second radiation constant is defined as $c_2 = hc/k$.

The spectral lines intensities are weighted according to the natural terrestrial isotopic abundances I_a; the total internal partition sum at a certain temperature, $Q(T)$, is given by

$$Q(T) = \sum_k g_k exp\left(-\frac{c_2 E_k}{T}\right) \tag{4.26}$$

where g_k and E_k are the statistical weight and the energy of the level k, respectively. The sum is performed over all the possible states k. To calculate the line intensity of

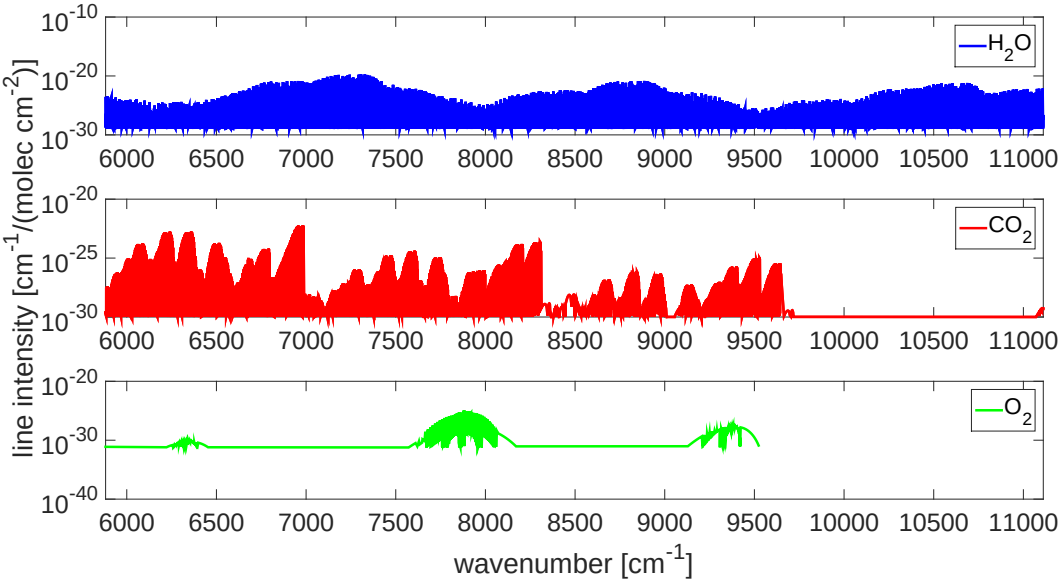

Figure 4.13: Spectral lines intensities from HITRAN database for water vapour (upper plot), carbon dioxide (middle plot) and oxygen (lower plot). The selected wavenumber interval corresponds to the near-IR wavelength range $[900-1700]nm$ ($T = 296K$).

the line strength at a temperature different from the reference temperature of $296K$, one uses the following expression, which is derived from Eq.4.25

$$S_{ij}(T) = S_{ij}(T_{ref})\frac{Q(T_{ref})}{Q(T)}\frac{\exp(-c_2E_i/T)}{\exp(-c_2E_i/T_{ref})}\frac{[1-\exp(-c_2\nu_{ij})/T]}{[1-\exp(-c_2\nu_{ij})/T_{ref}]} \tag{4.27}$$

The ratio of the total internal partition function can be calculated using the respective information provided by the HITRAN database. The provided data are an improvement over the casual classical approximation using a product of the independent temperature variation of the rotational and vibrational components of the partition function. The third factor in Eq.4.27 accounts for the ratio of Boltzmann distributions, and the fourth factor accounts for the effect of stimulated emission. In the limit $c_2\nu_{ij} >> T$ this factor is approximately 1.

In order to obtain the absorption cross-section for each trace gas, one has to evaluate the line shape function $F(\nu_{ij})$ for every line intensity. In fact a spectral line extends over a range of frequencies, not a single frequency as provided by the database.
There are three relevant phenomena which modify the line shape:

i. the lifetime of the transition given by the uncertainty principle;

ii. the Doppler broadening;

iii. the pressure broadening.

The **uncertainty principle** relates the lifetime of an excited state with the uncertainty of its energy

$$\Delta E \Delta t \gtrapprox \frac{\hbar}{2} \tag{4.28}$$

A short lifetime leads to large energy uncertainty and a broad emission. This broadening effect results in an unshifted Lorentzian profile. However this phenomenon is negligible compared to the other two in the lower and middle atmosphere.

The **Doppler broadening** of spectral lines is due to the Doppler effect caused by the velocity distribution of molecules. Different velocities of the particles result in different Doppler shifts, the cumulative effect of which is the line broadening.
A particular case is the thermal Doppler broadening due to the thermal motion of particles. This effect can be described by the Maxwell distribution of velocities $p(u)$, where u is the speed of the molecule relative to the observer and, in terms of Doppler shift (see Eq.4.30), it depends only on the frequency ν_{ij} of the spectral line, the mass m of the molecule and the temperature T

$$p(u)du = \sqrt{\frac{m}{2\pi kT}} \exp\Big[-\frac{mu^2}{2kT}\Big] du \tag{4.29}$$

For non-relativistic thermal velocities, the Doppler shift in frequency is

$$\nu = \nu_{ij}\left(1 + \frac{u}{c}\right) \tag{4.30}$$

Combining Eq.4.29 with Eq.4.30 leads to the frequency distribution, i.e. the line shape function, due to thermal Doppler broadening

$$f_G(\nu; \nu_{ij}, T)d\nu = \sqrt{\frac{mc^2}{2\pi kT\nu_{ij}}} \exp\Big(-\frac{mc^2(\nu - \nu_{ij})^2}{2kT\nu_{ij}^2}\Big)d\nu \tag{4.31}$$

The frequency distribution follows a Gaussian function with expected value $\mu = \nu_{ij}$ and variance $\sigma^2 = kT\nu_{ij}^2/mc^2$. From the variance it is possible to define the half-width at half-maximum $\alpha_D(T)$ as

$$\alpha_D(T) = \frac{\nu_{ij}}{c}\sqrt{\frac{2kT\log 2}{m}} \tag{4.32}$$

The third phenomenon is the so called **pressure broadening**. This process is caused by the collision of other particles with the emitting molecule. The collision shorts the characteristic lifetime of the transition and increases the uncertainty in the energy emitted (as occurs in natural broadening). The total effect depends on both the density and the temperature of the gas.

The pressure broadening, for a given pressure p and temperature T, is described by a Lorentzian profile and the associated shift is defined as

$$f_L(\nu; \nu_{ij}, T, p) = \frac{1}{\pi}\frac{\gamma(p, T)}{\gamma(p, T)^2 + [\nu - (\nu_{ij} + \delta(p_{ref})p)]^2} \tag{4.33}$$

where the location parameter of the Lorentzian function is $\nu_{ij} + \delta(p_{ref})p$. It specifies the location of the peak of the distribution and identifies the shifted transition frequency for the selected spectral line. The pressure shift $\delta(p_{ref})$ is provided by the HITRAN database.

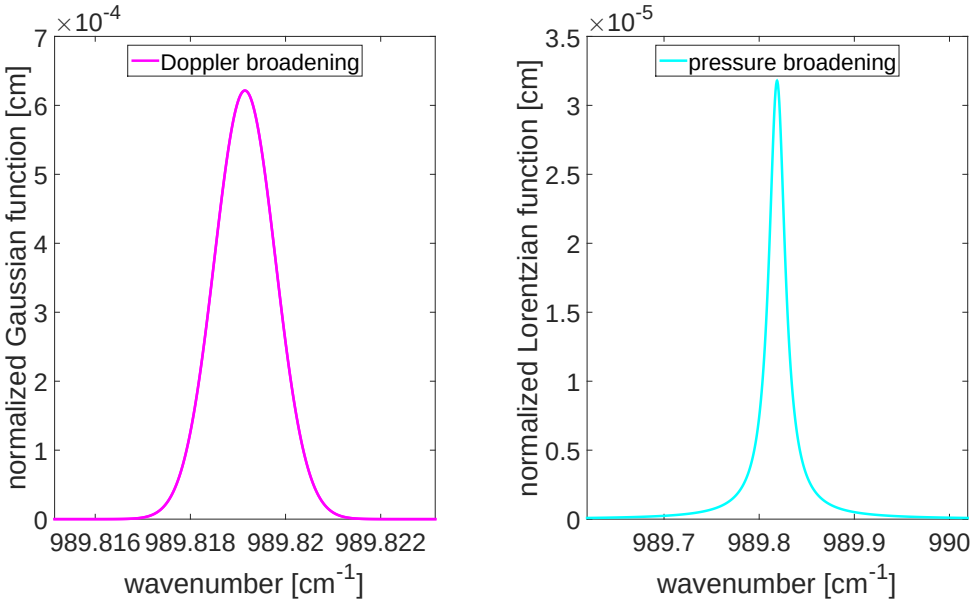

Figure 4.14: Doppler broadening and pressure broadening effects on the line shape for the transition at $\nu_{ij} = 989.8191\ cm^{-1}$ ($\lambda_{ij} \sim 1010.3\ nm$) occurring in the carbon dioxide isotope $^{12}C^{16}O_2$. The calculations are done for typical pressure and temperature values in the TTL, $p = 0.1 atm$ and $T = 200K$.

The scale parameter of the distribution is $\gamma(p, T)$, that specifies the half-width at half-maximum

$$\gamma(p, T) = \left(\frac{T_{ref}}{T}\right)^{n_{air}} (\gamma_{air}(p_{ref}, T_{ref})(p - p_{self}) + \gamma_{self}(p_{ref}, T_{ref})p_{self}) \tag{4.34}$$

where $\gamma_{air}(p_{ref}, T_{ref})$ and $\gamma_{self}(p_{ref}, T_{ref})$ are the air-broadened and self-broadened half-width at half-maximum evaluated for the reference pressure and temperature. These parameters are provided directly by the HITRAN database for each gas, as well as the coefficient of the temperature dependence n_{air}. The partial pressure of the considered gas, called p_{self}, is equivalent to the gas mixing ratio. Fig.4.14 shows, as an example, the Doppler (left panel) and pressure (right panel) line shapes for a specific transition occurring in the carbon dioxide molecule.

In the atmosphere, the pressure broadening is more relevant in the lower layers where the pressure is higher, while the Doppler broadening is more relevant in the middle and upper atmosphere, specifically in the stratosphere and the mesosphere, as shown in Fig.4.15.

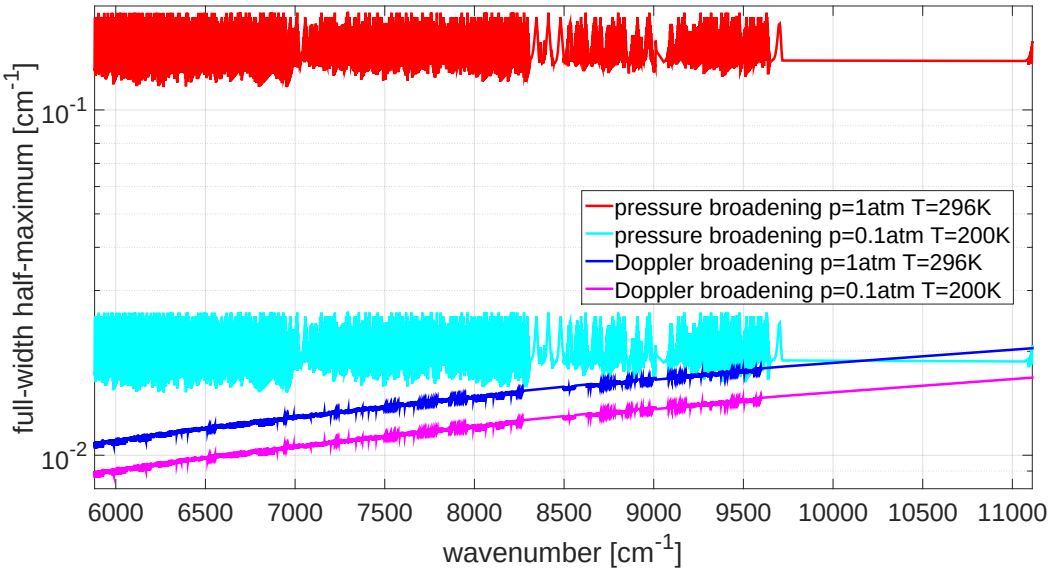

Figure 4.15: Full-width half-maximum calculations using different pressure and temperature values for the Doppler broadening effect (Gaussian function) and the pressure broadening effect (Lorentzian function). The calculations are for the carbon dioxide molecule using the wavelengths interval $[900 - 1700]nm$.

Since the measurements were collected in the TTL, where temperature and pressure are about 200K and $0.1atm$, it is fundamental to take into account both the profiles for the resulting line shape function.

The convolution of the two broadening mechanisms results in a Voigt profile [42]. Due to the computational expense of the convolution operation, the Voigt profile is often approximated using a pseudo-Voigt profile. The method used for the approximation is based on the Humlicek's algorithm [67].

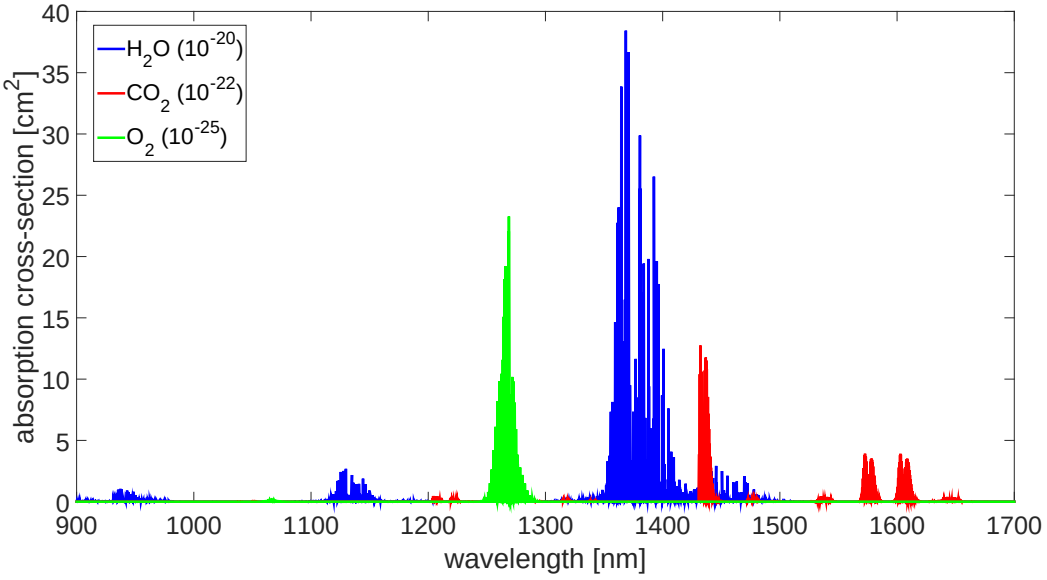

Figure 4.16: Absorption cross-sections for water vapour, carbon dioxide and oxygen in the $[900-1700]nm$ wavelength interval. The calculations are performed for typical TTL pressure and temperature conditions of $0.13atm$ and $204K$ using a $0.001nm$ wavelength increment.

Following [48], the Voigt profile function is expressed as

$$K(x,y) = \frac{y}{\pi}\int_{-\infty}^{\infty}\frac{\exp(-t^2)}{(x-t)^2+y^2}dt \tag{4.35}$$

where x is expressed in units of Doppler half-widths (Eq.4.32) and y is the ratio of the Doppler half-width to the Lorentzian half-width (Eq.4.34). The Humlicek's algorithm expresses the Voigt profile in terms of the complementary error function $erfc(z)$, as

$$K(x,y) = \Re[\exp(z^2)erfc(z)], \qquad z = y - ix \tag{4.36}$$

This relation allows for approximations of the error function which are applicable also for the Voigt profile. The algorithm divides the x,y space into four regions and it approximates the complex expression of Eq.4.36 by appropriate polynomials.

Once the Voigt profile is evaluated for every line of the spectrum, the absorption cross-

Table 4.3: Pressure and temperature grid points for the absorption cross-sections calculations.

Pressure [atm]	**Temperature [K]**
0.09	194.00
0.13	204.03
0.17	214.66
0.21	223.27
0.36	246.95
0.40	253.95
0.52	266.95
0.60	273.65
0.76	285.70
0.96	296.70

section is calculated by multiplying the line shape function with the intensity of the specific line and then interpolating to equally distant wavelength intervals.

The absorption cross-sections used in the present study are evaluated for different pressures and temperatures (see Table 4.3) extracted from the atmospheric profiles involved in the radiative transfer model (see subsection 4.4.2). For each gas the absorption cross-section is calculated using a fixed wavelength increment of $0.001nm$ (see Fig.4.16).

In order to get the best representation of the atmospheric absorption of the respective trace gas, a matrix containing all the cross-sections as a function of temperature and pressure is provided as input in the radiative transfer model. The model is able to interpolate linearly in between the different cross-sections in order to get the proper absorptions at a given pressure and temperature.

Since for the present study a full spectral retrieval is needed in the whole wavelengths interval $[900 - 1700]nm$, the RTM has to be run for several wavelengths, at least this can be done for the number of pixels of the spectrometer (i.e., 512). However, the input absorption cross-sections are available with a $0.001nm$ step, which means that the RTM linearly interpolates within the wavelengths interval to obtain the, e.g. 512,

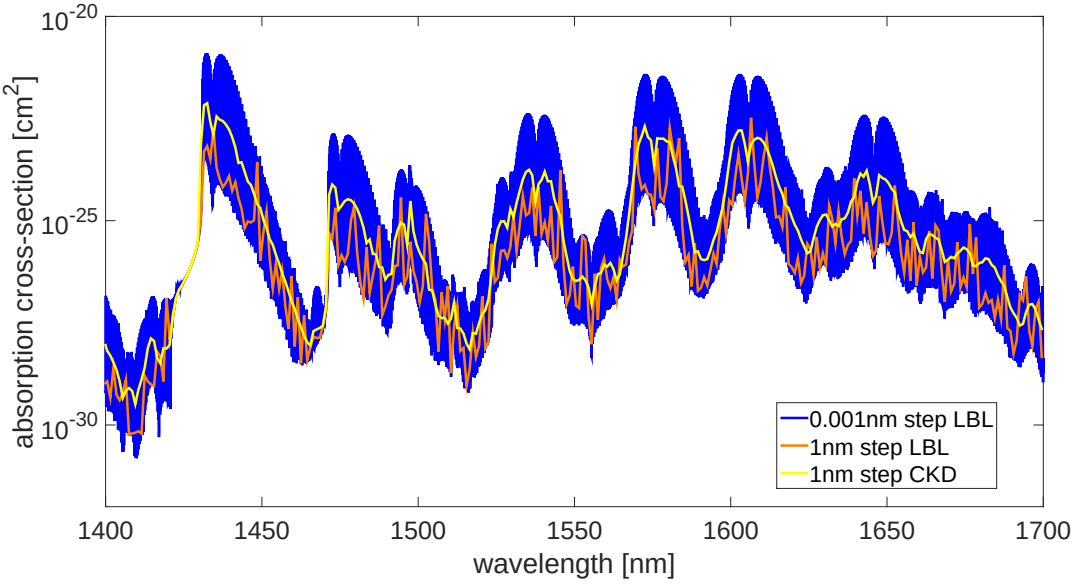

Figure 4.17: Absorption cross-section for carbon dioxide at $T = 204.03K$ and $p = 0.13atm$. Here, a zoom-in of the whole wavelengths interval used ($[900 - 1700]nm$) is shown. In one case (blue line), the cross-section is directly evaluated from the *line by line* intensities multiplied with the corresponding Voigt profile and then interpolated using a $0.001nm$ step. The orange line shows the same approach but using a $1nm$ step interpolation in order to reduce the consuming time in performing the following simulations. Finally, the yellow line shows the correlated-k distribution method which is evaluated using a $1nm$ wavelength increment.

wavelengths necessary for the calculations.

In this perspective, the RTM accounts only for a little part of the total available transitions (512 wavelengths vs. the $\sim 8 \times 10^5$ calculated wavelengths for the cross-sections), causing a loss of information in the retrieval procedure.

In order to avoid the loss of information, a procedure is developed following the works of *Goody et al.* and *Fu et al.* [36, 27] on the so called correlated-k distribution.

The main idea is to perform the radiative transfer calculations in steps of $1nm$ in the wavelengths interval $[900 - 1700]nm$. For each bin ($1nm$ wide) the cross-section

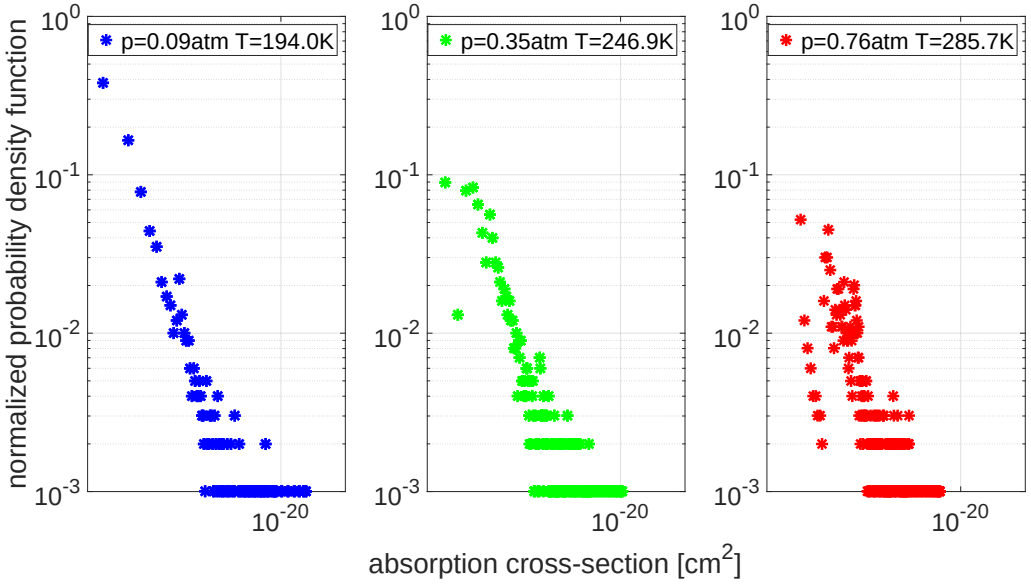

Figure 4.18: Probability density functions for water vapour in the wavelengths interval $[1400-1401]nm$, for different pressure and temperature conditions.

$k(\lambda, p, T)$ is divided into 1000 steps (n_{step}) with same increment $dk = (k_{max}-k_{min})/1000$, ranging from the absolute local minimum value (k_{min}) to the absolute local maximum value (k_{max}).

Finally, the occurrence frequency is counted, i.e. the probability density function $pdf(k+dk)$, of finding $k(\lambda, p, T)$ within the interval $[k_{min}+(n_{step}-1)dk, k_{min}+n_{step}dk]$. In the end a weighted average is performed that adds the different k_i values properly weighted with the correlated normalized probability density function

$$k_{CKD} = \sum_{i=1}^{1000} k_i \times pdf_i \tag{4.37}$$

One single k_{CKD} for each nanometer is obtained, which conserves the information of all the absorption lines within the considered wavelengths interval ($1nm$ wide). Using the correlated-k distributions, the RTM can be run for 800 wavelengths, but now for each nanometer all the spectral information available on the absorption cross-section for each

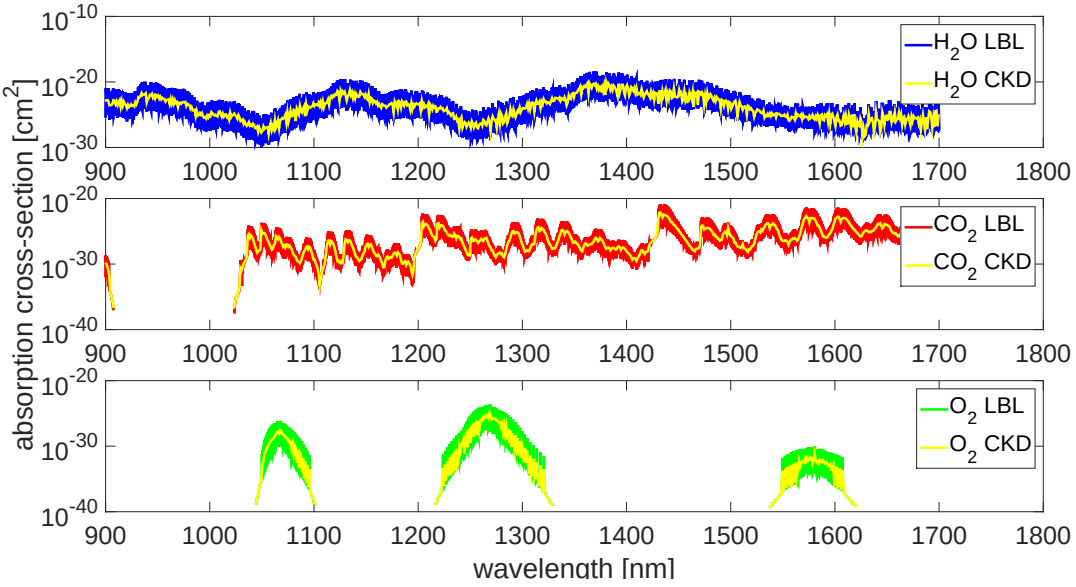

Figure 4.19: Correlated-k distribution of water vapour (upper plot), carbon dioxide (middle plot) and oxygen (lower plot). LBL denotes the *line by line* absorption cross-section, i.e. the evaluation of $k(\lambda, p, T)$ using a step of $0.001nm$, while the CKD indicates the procedure which takes advantage of the probability density functions of $k(\lambda, p, T)$. This method provides an averaged value k_{CKD} using a step of $1nm$. The calculations are performed for a pressure of $0.13atm$ and temperature of $204.03K$.

gas is preserved, see Fig.4.17.

Fig.4.18 shows the probability density functions (pdf_i) for water vapour, in the wavelengths interval $[1400 - 1401]nm$ for different pressure and temperature conditions. Fig.4.19 shows the results based on the correlated-k distribution method for water vapour (upper panel), carbon dioxide (middle panel) and oxygen (lower panel). Finally, Fig.4.20 shows the impact of the correlated-k method on the simulated spectral radiance.

For the present work, the molecular absorption cross-sections are evaluated using the correlated-k distributions for all the pressure and temperature conditions reported in Table 4.3.

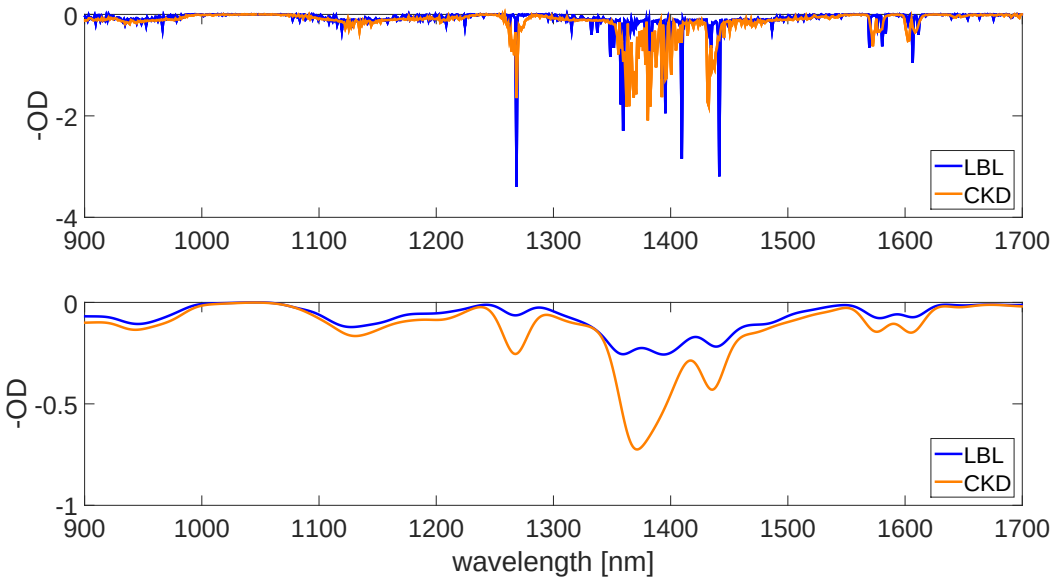

Figure 4.20: Results for the simulations using the correlated-k distribution method (CKD) and the linear interpolation (LBL) with $1nm$ step. The simulations are run under clear sky conditions including the near-IR absorption bands of : H_2O, CO_2 and O_2. In the upper panel no usage of the ISF is done while in the lower panel both simulations are convolved with a Gaussian function ($\sigma = 10nm$).

4.5.2 Rayleigh Scattering

The molecular scattering is described by Rayleigh scattering. The Rayleigh scattering is the elastic scattering of electromagnetic radiation by particles much smaller than the wavelength of the radiation. This process results from the electric polarizability of the particles (particles may be individual atoms or molecules). The oscillating electric field of a light wave acts on the charges within a particle, causing them to move at the same frequency. The particle becomes a small radiating dipole whose radiation is seen as scattered light.

The size of a scattering particle is often parameterized by the ratio

$$x = \frac{2\pi r}{\lambda} \tag{4.38}$$

where r is the characteristic length, equivalently the radius of the molecule, and λ the wavelength of light. In this study the molecules involved in the calculations are oxygen, carbon dioxide and water vapour. These molecules have typical sizes which range from ca. $0.06nm$ (oxygen molecule) to ca. $0.12nm$ (carbon dioxide). Since Rayleigh scattering applies to the case when the scattering particles is very small ($x << 1$) and the whole surface re-radiates with the same phase, the approximation is largely satisfied for the molecules involved in the near-IR range.

For the Rayleigh approximation the scattering cross-section can be written using the analytic function [92]

$$\sigma_{Ray} = \frac{24\pi^3(n_s^2-1)^2}{\lambda^4 N_s^2(n_s^2+2)^2}\left(\frac{6+3\rho}{6-7\rho}\right) \tag{4.39}$$

where σ_{Ray} is the scattering cross-section per molecule; N_s is the molecular density; n_s is the refractive index of air; λ is the wavelength; the term $(6+3\rho)/(6-7\rho)$ is called the depolarization term; and ρ is the depolarization factor, which describes the effect of molecular anisotropy. The depolarization factor is the least known for purposes of Rayleigh scattering calculations and it is responsible for the most uncertainty.

In order to have a precise representation for the Rayleigh scattering cross-section many different techniques have been developed. In *Bodhaine et al.* [11], a survey of the literature is conducted in order to determine the physical constants necessary for the calculations of Rayleigh optical depth. They come up with a final parametrization for the Rayleigh scattering cross-section which is based on a five-parameters equation as a function of wavelength

$$\sigma(\times 10^{-28} cm^2) = \frac{1.0455996 - 341.29061\lambda^{-2} - 0.90230850\lambda^2}{1 + 0.0027059889\lambda^{-2} - 85.968563\lambda^2} \tag{4.40}$$

This parameterization falls in the class of ratio of polynomials commonly used in curve-fitting. For the refractive index of dry air with 300 ppm CO_2 concentration, they used

the *Peck and Reeder* [91] formula

$$(n_{300} - 1) \times 10^8 = 8060.51 + \frac{2480990}{132.274 - \lambda^{-2}} + \frac{17455.7}{39.32957 - \lambda^{-2}} \tag{4.41}$$

scaled for the desired CO_2 concentration [23]

$$\frac{(n-1)_{CO_2}}{(n-1)_{300}} = 1 + 0.54(CO_2 - 0.0003) \tag{4.42}$$

where the CO_2 concentration is expressed as parts per volume. Therefore, for Rayleigh cross-section calculations (Eq.4.39), it is necessary to evaluate the correct refractive index, in terms of carbon dioxide concentration and finally use a parameterization for the polarization term. In this respect *Bodhaine et al.* have parameterized the polarization term of the air, following [10], as

$$\frac{(6+3\rho)}{6-7\rho} = \frac{78.084 \times F(N_2) + 20.946 \times F(O_2) + 0.934 \times F(Ar) + C_{CO_2} \times F(CO_2)}{78.084 + 20.946 + 0.934 + C_{CO_2}} \tag{4.43}$$

where the polarization terms $F(molecule)$, for each gas, are given by

$$\begin{aligned} F(N_2) &= 1.034 + 3.17 \times 10^{-4}\lambda^{-2} \\ F(O_2) &= 1.096 + 1.385 \times 10^{-3}\lambda^{-2} + 1.448 \times 10^{-4}\lambda^{-4} \\ F(Ar) &= 1.00 \\ F(CO_2) &= 1.15 \end{aligned} \tag{4.44}$$

Within this work, the radiative transfer model simulations are all executed using Eq.4.40 in order to account for the Rayleigh scattering caused by molecules in the atmosphere. Eq.4.40 is accurate to better than 0.001% over the $[250-850]nm$ range, and still better than 0.05% out of it.

Beyond the elastic scattering, photons may scatter inelastically. This process relates to the so called Raman scattering [102]. In this case the scattered photon does not preserve its initial energy and the molecule changes its internal energy due to a transition

to another rotational or vibrational energy level. When the molecule absorbs energy, the process is called Stokes Raman scattering, and the scattered photon has less energy than the incident photon; vice versa, when the scattered photon has more energy than the incident one, then the molecule has lost energy due to an emission process, and in this case we refer to anti-Stokes Raman scattering.
In the atmosphere, the Raman scattering (called Ring effect) was noted as a filling in broadening and reduction of depth in the solar Fraunhofer lines when viewed from the ground in scattered sunlight [37]. This effect impacts mostly the UV/vis wavelengths intervals due to the wavelengths dependency of Rayleigh scattering and the predominance of Mie scattering in the near-IR range [14]. Therefore, it can be neglected in the present study.

The Rayleigh's Phase Function

To a first approximation, scattering by clear air is isotropic. However, an accurate calculation of Rayleigh differential cross-section for unpolarized radiation leads to

$$p(\cos\Theta) = \frac{3}{16\pi}(1+\cos^2\Theta) \tag{4.45}$$

which can be obtained starting from the scattered electric field of a dipole [52]. The integration over the solid angle, according to Eq.4.6, provides a phase function which is normalized to unity (example of conservative scattering).
Considering only the Rayleigh cross-section in radiative transfer calculations implies that all the air molecules act as perfect diffusers, i.e. there is no loss of energy in terms of absorption but only a redistribution of energy due to scattered photons.
The Rayleigh phase function in polar coordinates is shown in Fig.4.21. E_x (in blue) indicates the electric field polarized along the x direction (i.e., $p(\cos\Theta) = const$), while E_y

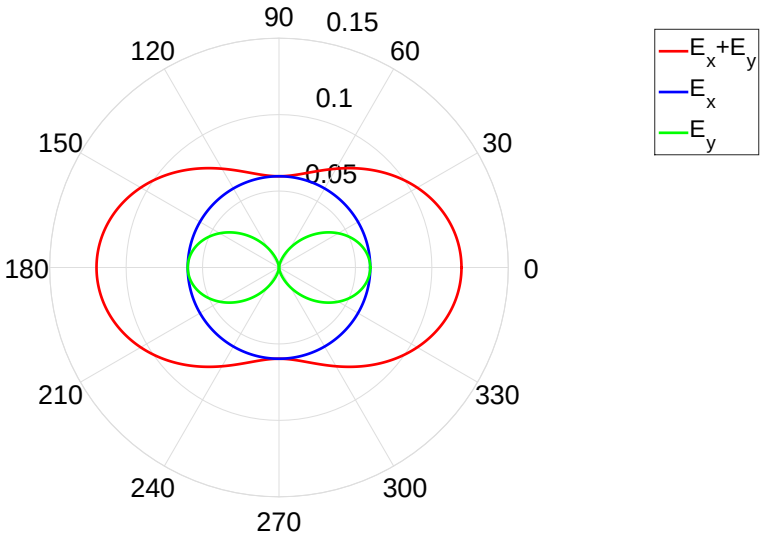

Figure 4.21: Rayleigh's phase function in polar coordinates.

(in green) is the polarization along the y direction (i.e., $p(\cos\Theta) = const \times \cos^2\Theta$). The unpolarized radiation ($E_x + E_y$, in red) takes into account both polarizations (i.e., Eq.4.45).

For unpolarized radiation, the redistribution of energy occurs almost with the same probability in all the 360-degrees directions. What is different from a perfect isotropic diffuser (e.g., E_x in Fig.4.21) is the presence of two equidistant lobes which merge in the center of the phase diagram.

4.6 Ice Particle Extinction

After the description about the calculations performed for the atmospheric gases, the discussion should address the representation of particles forming the tropical cirrus. Ice particles represent an ensemble of different dimensions and shapes, therefore they can be treated statistically. The first step in their characterization is the definition of a function which describes the probability of finding a particle with a certain dimension in the total ensemble. This probability function is usually called particle size distribution (PSD). In first approximation ice crystals, that may appear with several different shapes like aggregates, bullets, rosettes, columns and plates, can be treated as mass-equivalent spheres with radius r [81, 6]. As shown in [136] the optical properties of different

crystals change only slightly in the near-IR wavelengths range. The major difference in the optical properties derives from the dimension of the crystal, regardless of its shape. Large particles absorb more energy because they have a larger geometric cross-section, i.e. mass, with respect to small particles.

Following the work of [81], tropical cirrus ice particles can be characterized using two different particle size distributions: the gamma distribution for small particles (i.e. $r \in [0-50]\mu m$) and the lognormal distribution for large particles (i.e. $r \in [50-200]\mu m$). Their parameterization concept is based on four major requirements that here we would recall as it is written in their work:

i. the optical and radiative properties from the parameterized size distributions had to replicate those from the observed size distributions as closely as possible;

ii. mass conservation is required;

iii. the contributions of the smaller ice crystals had to be realistically represented;

iv. the parameterization had to be easily integratable over all possible crystal sizes and converge.

4.6.1 The Gamma Distribution

The gamma distribution is a two-parameter continuous probability distribution characterized by a shape parameter k and a scale parameter θ

$$f_G(r; k, \theta) = \frac{r^{k-1} e^{-\frac{r}{\theta}}}{\theta^k \Gamma(k)} \tag{4.46}$$

where $\Gamma(k) = (k-1)!$ is the gamma function, extension of the factorial function. In order to connect the two parameters of the gamma distribution with other specific physical parameters of cirrus clouds, *McFarquhar and Heymsfield* [81] suggest a parameterization of the gamma distribution according to the amount of ice water content ($IWC_{<50}$)

within the cloud

$$n_G(r; IWC_{<50}) = \frac{12 IWC_{<50} \alpha_{<50}^5 r}{\pi \rho_{ice} \Gamma(5)} \exp(-2\alpha_{<50} r) \tag{4.47}$$

where ρ_{ice} is the mass density of ice, i.e. $0.91 \times 10^6 gm^{-3}$, and $IWC_{<50}$ is the total amount of ice crystals ($[gm^{-3}]$) having a radius smaller than $50\mu m$. The parameter $\alpha_{<50}$ is defined as

$$\alpha_{<50} = b - m \log_{10}\left(\frac{IWC_{<50}}{IWC_0}\right) \tag{4.48}$$

where $b = (-4.99 \pm 5.50) \times 10^{-3} \mu m^{-1}$, $m = 0.0494 \pm 0.0029 \mu m^{-1}$ and $IWC_0 = 1 gm^{-3}$. The Eq.4.47 is written in the form so that the integral over all crystals sizes $(0 \rightarrow \infty)$ is equal to $IWC_{<50}$.

Comparing Eq.4.46 with Eq.4.47 leads to the shape parameter and the scale parameter of the gamma distribution as a function of $\alpha_{<50}$ or equivalently, see Eq.4.48, as a function of $IWC_{<50}$

$$\begin{aligned} k &= 2 \\ \theta &= \frac{1}{2\alpha_{<50}} \end{aligned} \tag{4.49}$$

4.6.2 The Lognormal Distribution

For larger ice crystals ($r \in [50 - 200]\mu m$), a lognormal distribution is used. The lognormal distribution is a continuous probability distribution of a variable whose logarithm is normally distributed

$$f_{LN}(r; r_m, S) = \frac{const}{\sqrt{2\pi}\ln(S)} \frac{1}{r} \exp\left[-\frac{(\ln r - \ln r_m)^2}{2\ln^2(S)}\right] \tag{4.50}$$

where S is the geometric standard deviation related to r as well as r_m represents the median radius. In this case, the parameterization [81] depends on ice water content

($IWC_{>50}$) and temperature (T) of the cloud, such that

$$n_{LN}(r; IWC_{>50}, T) = \frac{6IWC_{>50}}{\pi^{3/2}\rho_{ice}\sqrt{2}\exp(3\mu_{>50} + (9/2)\sigma_{>50}^2)2r\sigma_{>50}D_0^3} \times \exp\left[-\frac{1}{2}\left(\frac{\ln(2r/D_0) - \mu_{>50}}{\sigma_{>50}}\right)^2\right] \tag{4.51}$$

where $D_0 = 1\mu m$ and $\mu_{>50}$ and $\sigma_{>50}$ are two parameters depending on $IWC_{>50}$ and T, defined as following

$$\begin{aligned} \mu_{>50} &= a_\mu(T) + b_\mu(T)\log_{10}\left(\frac{IWC_{>50}}{IWC_0}\right) \\ \sigma_{>50} &= a_\sigma(T) + b_\sigma(T)\log_{10}\left(\frac{IWC_{>50}}{IWC_0}\right) \end{aligned} \tag{4.52}$$

again $IWC_0 = 1gm^{-3}$, and $IWC_{>50}$ represents the ice water content of ice crystals having a radius longer then $50\mu m$. a_μ, b_μ, a_σ and b_σ can be expressed as linear functions of the temperature as following

$$\begin{aligned} a_\mu(T) &= a_{a_\mu} + b_{a_\mu}T \\ b_\mu(T) &= a_{b_\mu} + b_{b_\mu}T \\ a_\sigma(T) &= a_{a_\sigma} + b_{a_\sigma}T \\ b_\sigma(T) &= a_{b_\sigma} + b_{b_\sigma}T \end{aligned} \tag{4.53}$$

with the coefficients given in Table 4.4. The units of the a terms are the natural logarithm of μm; for the b terms, the natural logarithm of $\mu m°C^{-1}$. For typical tem-

Table 4.4: Coefficients of the temperature dependent terms of Eq.4.53.

a_{a_μ}	5.20 ± 0.02
b_{a_μ}	0.0013 ± 0.0005
a_{b_μ}	0.026 ± 0.023
b_{b_μ}	$-1.2 \pm 0.5 \times 10^{-3}$
a_{a_σ}	0.47 ± 0.02
b_{a_σ}	$2.1 \pm 0.5 \times 10^{-3}$
a_{b_σ}	0.018 ± 0.023
b_{b_σ}	$-2.1 \pm 4.7 \times 10^{-4}$

peratures of cirrus in the TTL, i.e. for temperatures ranging from $-70°C$ to $-60°C$, the parameters involved in Eq.4.52 are fixed to

$$\begin{aligned} a_\mu &= 5.156 \pm 0.007 \\ b_\mu &= 0.091 \pm 0.005 \\ a_\sigma &= 0.370 \pm 0.004 \\ b_\sigma &= 0.030 \pm 0.002 \end{aligned} \tag{4.54}$$

Given any temperature and ice water content, the size distribution can be determined using the sum of the gamma and lognormal distribution. Comparing Eq.4.50 with Eq.4.51 is possible to find the geometric standard deviation and the median radius of the lognormal distribution as a function of $\sigma_{>50}$ and $\mu_{>50}$

$$\begin{aligned} S &= \exp(\sqrt{\sigma_{>50}}) \\ r_m &= \frac{D_0}{2}\exp(\mu_{>50}) \end{aligned} \tag{4.55}$$

The total amount of ice water content, IWC_T, is given by the sum of the ice water content of small crystals and the ice water content of larger crystals, i.e. $IWC_T = IWC_{<50} + IWC_{>50}$. Starting from the data on tropical cirrus collected during the CEPEX experiment, *McFarquhar and Heymsfield* [81] found a parametrization of the ice water content for small crystals in terms of the total ice water content

$$IWC_{<50} = \min\left[IWC_T, a\left(\frac{IWC_T}{IWC_0}\right)^b\right] \tag{4.56}$$

where $a = 0.252 \pm 0.068 gm^{-3}$ and $b = 0.837 \pm 0.054$; in Fig.4.22 the behavior of the IWCs for small and large crystals as a function of the total amount, is shown. Fig.4.23 shows the total particle size distribution, i.e. the resulting distribution deriving from the small particles contribution (accounted by the gamma distribution), and the large particles contribution (accounted by the lognormal distribution). The resulting particle size distribution is totally determined when a total amount of ice water content and the

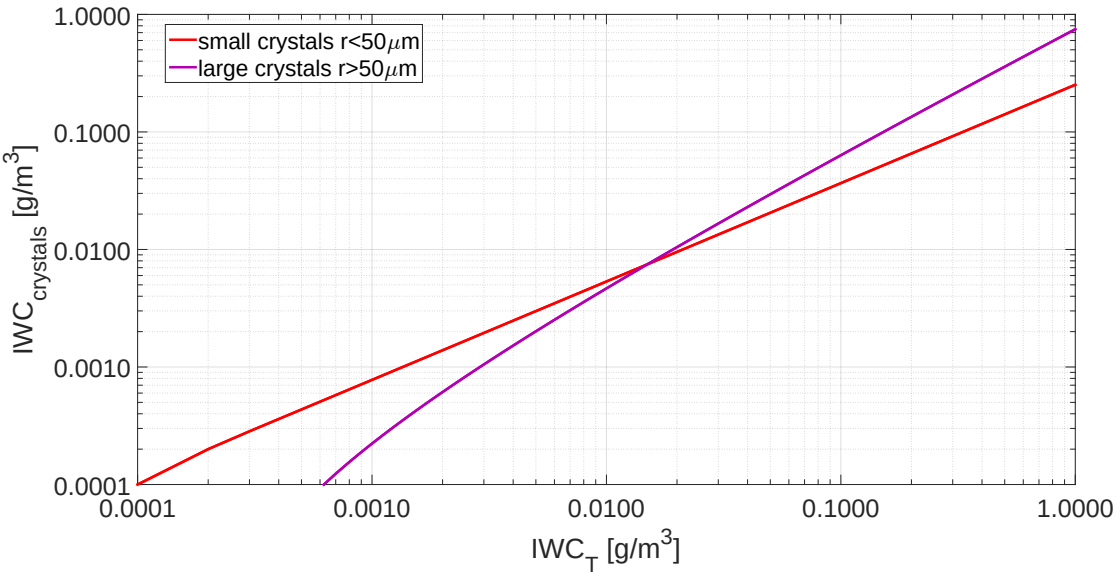

Figure 4.22: Parameterization of the ice water content assuming a gamma distribution for small crystals ($r < 50\mu m$), and a lognormal distribution for large crystals ($r > 50\mu m$) from [81].

temperature of the cloud are selected.

To facilitate the inversion of radiation measurements, it is convenient to describe the size distributions with the minimum number of parameters. The first parameter should be a measure of the mean particle size. The arithmetic mean is

$$\bar{r} = \frac{\int_{r_{min}}^{r_{max}} r n(r) dr}{\int_{r_{min}}^{r_{max}} n(r) dr} = \frac{1}{N} \int_{r_{min}}^{r_{max}} r n(r) dr \tag{4.57}$$

where N is the total number of particles per unit volume and $n(r)$ is the selected particle size distribution. Since each particle scatters an amount of light proportional to $\sigma_{sca} = \pi r^2 Q_{sca}$, where σ_{sca} is the scattering cross-section and Q_{sca} represents the scattering efficiency factor, a better parameter describing the scattered light is the mean radius for scattering,

$$r_{sca} = \frac{\int_{r_{min}}^{r_{max}} r \pi r^2 Q_{sca} n(r) dr}{\int_{r_{min}}^{r_{max}} \pi r^2 Q_{sca} n(r) dr} \tag{4.58}$$

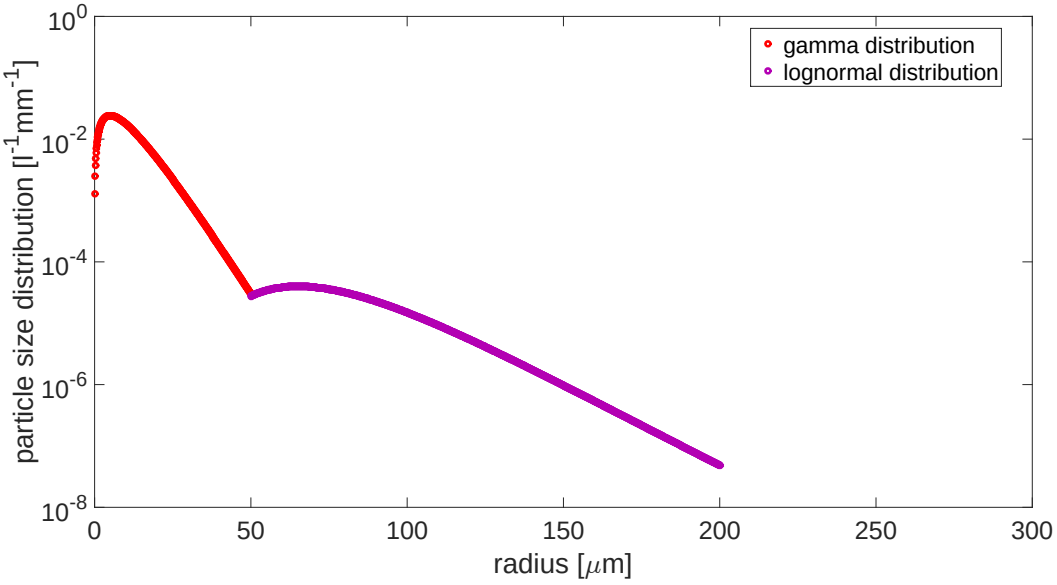

Figure 4.23: Particle size distributions for small crystals (gamma distribution) and large crystals (lognormal distribution) for a fixed amount of $IWC = 0.015 gm^{-3}$. The temperature of the cloud particles ranges in the interval $[-70, -60]°C$.

The dependency of the mean radius for scattering from the scattering efficiency factor, renders the parameter not a good candidate in order to retrieve particles optical properties because the scattering efficiency factor is itself an unknown quantity. As suggested by [38], if r_{sca} is larger than the wavelength, a parameter which is still significant for radiative transfer calculations can be obtained by omitting Q_{sca} in Eq.4.58.

Thus we define the effective radius as

$$r_{eff} = \frac{\int_{r_{min}}^{r_{max}} r\pi r^2 n(r)dr}{\int_{r_{min}}^{r_{max}} \pi r^2 n(r)dr} = \frac{1}{G}\int_{r_{min}}^{r_{max}} r\pi r^2 n(r)dr \tag{4.59}$$

where G is the geometric cross-section of particles per unit volume. In Fig.4.24 the behavior of the effective radius as well as the mean radius as a function of the ice water content is shown. In the left (right) panel calculations using the gamma (lognormal) distribution are presented.

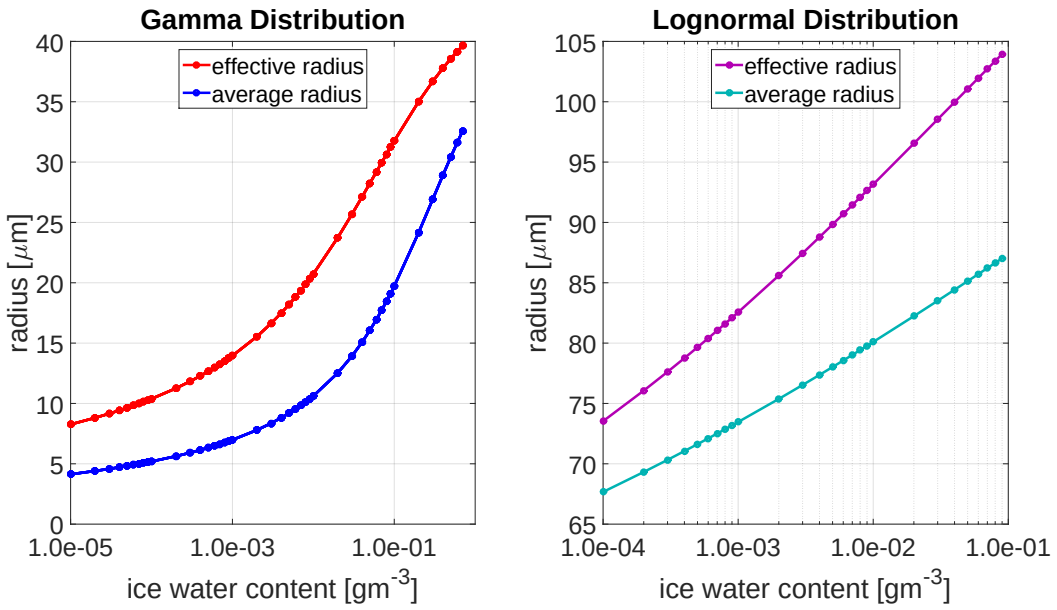

Figure 4.24: The effective radius and the mean radius as a function of the ice water content for small particles (left panel) and large particles (right panel). The calculations are performed using the parameterization of Eq.4.47 for the gamma distribution (small particles) and of Eq.4.51 for the lognormal distribution (large particles) for temperature in the range of $[-70, -60]°C$ for the latter case.

After describing the particle size distributions of mass-equivalent ice spheres, it is necessary to apply a rigorous scattering theory which treats the scattering of light by homogeneous spheres using the formal solution of Maxwell's equations with appropriate boundary conditions, in other terms the Mie theory.

4.6.3 The Mie Theory

In the following some basic concepts of the Mie theory, also known as Lorenz-Mie theory, are reported. They are the direct solutions to Maxwell's equations and the resulting efficiency factors for absorption and scattering, which are the main core of radiative transfer calculations under cloudy conditions. A thorough treatment of Maxwell theory as well as Mie theory is beyond the scope of this thesis, but both are widely

treated in the following references [47, 86, 84, 52].

The theory of Mie is a comprehensive, mathematically rigorous solution describing the scattering of an electromagnetic wave by a sphere [84]. Mie scattering applies to scatters of any size and, in the limit of scatter sizes very small with respect to the incident wavelength, the Mie solution collapses into Rayleigh scattering (see subsection 4.5.2). The solution is composed by an infinite series of spherical multipole partial waves and, due to the spherical symmetry of the particles, it can be applied to all those geometries where it is possible to separate the equations describing the radial and angular components of the solution. For more general shaped particles the so-called T-matrix method can be applied [129], which is a generalization of the Mie theory.
The starting point of Mie theory are Maxwell's equations, which constitute the fundamental laws governing the interaction of the electromagnetic field with matter. They can be expressed using the Gaussian units as following

$$\begin{aligned} \vec{\nabla} \times \vec{E} &= -\frac{1}{c}\frac{\partial \vec{H}}{\partial t} & \vec{\nabla} \cdot \vec{D} &= 4\pi\rho \\ \vec{\nabla} \times \vec{H} &= \frac{4\pi\vec{J}}{c} + \frac{1}{c}\frac{\partial \vec{D}}{\partial t} & \vec{\nabla} \cdot \vec{H} &= 0 \end{aligned} \tag{4.60}$$

where t is the time, c is the velocity of light, $\vec{H}$ is the magnetic field strength, $\vec{E}$ is the electric field strength, $\vec{D}$ is the dielectric displacement, $\vec{J}$ is the current density and ρ is the density of charge. For atmospheric applications, where the magnetic permeability of the air (μ), as well as of water, is close to 1 (in Gaussian units), we can employ in Maxwell's equations equivalently the magnetic field inside matter $\vec{H}$ or the magnetic induction field $\vec{B}$, since they are linearly dependent, i.e. $\mu\vec{H} = \vec{B}$. Both the dielectric displacement and the current density are a linear function of the electric field

$$\vec{D} = \epsilon\vec{E} \qquad \vec{J} = \sigma\vec{E} \tag{4.61}$$

where ϵ is the dielectric constant and σ is the conductivity. Another independent

equation that can be obtained with an easy manipulation of Maxwell's equations is the law expressing the conservation of charge

$$\vec{\nabla} \cdot \vec{J} + \frac{\partial \rho}{\partial t} = 0 \tag{4.62}$$

Following the book of *Van de Hulst* [47], we can consider periodic fields with frequency ω which describe the periodic phenomena involved in the electromagnetic interaction, then the vectorial quantities can be expressed as complex functions of the time in the form

$$A = (\alpha + i\beta)e^{i\omega t} \tag{4.63}$$

Applying these periodic fields to Maxwell's Eq.4.60 brings to the simpler forms

$$\vec{\nabla} \times \vec{E} = -ik\vec{H} \tag{4.64}$$

$$\vec{\nabla} \times \vec{H} = ikm^2\vec{E} \tag{4.65}$$

where $k = \omega/c = 2\pi/\lambda$ is the wavenumber in vacuum and m is the complex refractive index of the medium at the frequency ω

$$m^2 = \epsilon - i\frac{4\pi\sigma}{\omega} \tag{4.66}$$

The refractive index m describes how the light propagates through a medium. This is represented by the real part of the complex number in Eq.4.66 which accounts for refraction, while the imaginary term describes the attenuation, i.e. the absorption.

In our case the medium is made of ice crystals of different sizes and, using the *Warren and Brandt* compilation [128], the real and imaginary parts of the refractive index of ice can be extracted and they are displayed in Fig.4.25. The values are tabulated for a nominal temperature of 266K.

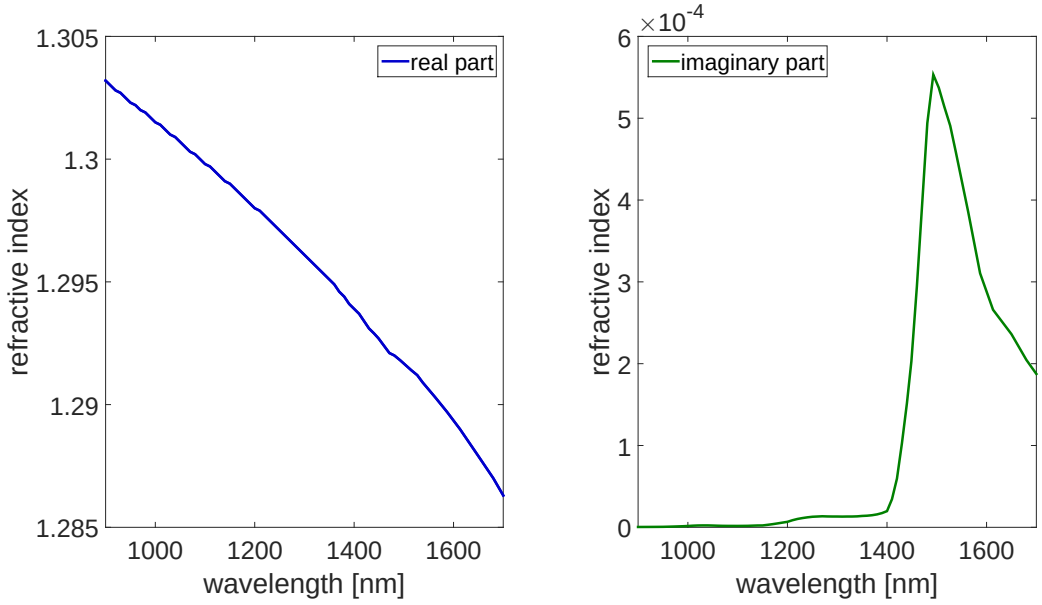

Figure 4.25: The refractive index of ice from [128]. In the left panel (right panel) the real (imaginary) part of the refractive index, or equivalently the refraction (absorption) term, is shown.

The divergence of Eq.4.65, i.e. $\vec{\nabla}(m^2\vec{E}) = 0$ in a homogeneous medium ($m = const$) translates into the vanishing of the divergence of $\vec{E}$ itself, so that the charge density $\rho = 0$. Another consequence is that any rectangular component of $\vec{E}$ and $\vec{H}$ satisfies the scalar wave equation

$$\triangle \psi = -k^2 m^2 \psi \tag{4.67}$$

which has as simplest solution a plane wave equation traveling in the z-direction

$$\psi = e^{ikmz+i\omega t}. \tag{4.68}$$

Using the spherical coordinates (r, θ, ϕ) instead of the Cartesian coordinates (x, y, z), leads to the following solutions for the scalar wave (Eq.4.67) which are separable and of the type:

$$\psi_{ln} = \begin{cases} \cos(l\phi) \\ \sin(l\phi) \end{cases} \quad P_n^l(\cos\theta) j_n(mkr). \tag{4.69}$$

Here n and l are integers ($n \geq l \geq 0$), P_n^l is an associated Legendre polynomial and j_n may be any spherical Bessel function, defined by

$$j_n(x) = \sqrt{\frac{\pi}{2x}} J_{n+\frac{1}{2}}(x) \tag{4.70}$$

in terms of ordinary Bessel functions J_n.

Applying the same approach to the (θ, ϕ) components of the vector fields $\vec{E}$ and $\vec{H}$, and taking into account the boundary conditions of the medium where the electromagnetic field is propagating, the resulting field components can be written in the form:

$$\begin{aligned} E_\theta = H_\phi &= -\frac{i}{kr} e^{-ikr+i\omega t} \cos(\phi) S_2(\theta) \\ -E_\phi = H_\theta &= -\frac{i}{kr} e^{-ikr+i\omega t} \sin(\phi) S_1(\theta) \end{aligned} \tag{4.71}$$

where $S_1(\theta)$ and $S_2(\theta)$ are the amplitude functions. The amplitude functions can be expressed as functions of the Mie solutions a_n and b_n and of the scattering angle functions $\pi_n(\cos\theta)$ and $\tau_n(\cos\theta)$, such that

$$\begin{aligned} S_1(\theta) &= \sum_{n=1}^{\infty} \frac{2n+1}{n(n+1)} \{a_n \pi_n(\cos\theta) + b_n \tau_n(\cos\theta)\} \\ S_2(\theta) &= \sum_{n=1}^{\infty} \frac{2n+1}{n(n+1)} \{b_n \pi_n(\cos\theta) + a_n \tau_n(\cos\theta)\} \end{aligned} \tag{4.72}$$

where the scattering angle functions are

$$\begin{aligned} \pi_n(\cos\theta) &= \frac{1}{\sin\theta} P_n^1(\cos\theta) \\ \tau_n(\cos\theta) &= \frac{d}{d\theta} P_n^1(\cos\theta) \end{aligned} \tag{4.73}$$

and the Mie solutions are

$$\begin{aligned} a_n &= \frac{\psi_n'(y)\psi_n(x) - m\psi_n(y)\psi_n'(x)}{\psi_n'(y)\zeta_n(x) - m\psi_n(y)\zeta_n'(x)} \\ b_n &= \frac{m\psi_n'(y)\psi_n(x) - \psi_n(y)\psi_n'(x)}{m\psi_n'(y)\zeta_n(x) - \psi_n(y)\zeta_n'(x)} \end{aligned} \tag{4.74}$$

ψ_n and ζ_n are the Riccati-Bessel functions, the derivatives of these functions are denoted by primes, and the arguments x and y are functions of the sphere radius r

$$x = \frac{2\pi r}{\lambda} \qquad y = mkr \tag{4.75}$$

The amplitude functions describe the amplitude and phase of a scattered scalar wave. They are decisive for the extinction calculations for example in forward scattering direction $\theta = 0$. In general, the amplitude functions are four equations forming a matrix of four elements which defines the scattering in any directions (θ, ϕ). In the case of Mie theory where the particle have a spherical shape, considerations about the symmetry of the problem reduce the amplitude functions to two elements where $S_3(\theta)$ and $S_4(\theta)$ vanish.

The amplitude functions expressed in Eq.4.72 are fundamental for the efficiency factors calculations. The efficiency factors are defined in terms of the relative cross-sections as function of the geometric cross-section $G = \pi r^2$

$$\begin{aligned} Q_{ext} &= C_{ext}/G \\ Q_{sca} &= C_{sca}/G \\ Q_{abs} &= C_{abs}/G \end{aligned} \tag{4.76}$$

where the C terms are the cross-sections for extinction, scattering and absorption, respectively. In general these factors depend on the orientation of the particle and on the state of polarization of the incident light. In the case of spheres they are independent of both and in all cases we have

$$Q_{ext} = Q_{sca} + Q_{abs} \tag{4.77}$$

The extinction efficiency factor can be determined from the amplitude functions for $\theta = 0$, i.e. analyzing the light attenuated in the forward direction with respect to the incident direction. Both $S_1(\theta = 0)$ and $S_2(\theta = 0)$ assume the same expression

$$S(0) = \frac{1}{2}\sum_{n=1}^{\infty}(2n+1)(a_n + b_n) \tag{4.78}$$

where, for $\theta = 0$, one can use the relations

$$\pi_n(1) = \tau_n(1) = \frac{1}{2}n(n+1) \tag{4.79}$$

When we apply Eq.4.78 to the fundamental extinction formula for one interacting particle [47], given by

$$C_{ext} = \frac{4\pi}{k^2}\Re\{S(0)\} \tag{4.80}$$

It provides the equation for the extinction efficiency factor Q_{ext} expressed in term of the Mie coefficients

$$Q_{ext} = \frac{2}{x^2}\sum_{n=1}^{\infty}(2n+1)\Re(a_n + b_n) \tag{4.81}$$

Finally the expression providing the efficiency factor for scattering is described by

$$Q_{sca} = \frac{2}{x^2}\sum_{n=1}^{\infty}(2n+1)\{|a_n|^2 + |b_n|^2\} \tag{4.82}$$

This relation in terms of Mie coefficients had been investigated by Debye.
For a comprehensive treatment of all the formula involved in Mie scattering calculations see the references [84, 47, 86].

Once the efficiency factors are known using the analytical solutions of Mie theory, it is possible to build up a code which evaluates these properties for a single sphere. In the case of an ensemble of particles, the properties of the whole ensemble can be evaluated according to a specific particle size distribution and assuming the particle are independent scatterers.
Essentially, the particle size distribution statistically defines how much a particle of a certain size contributes to the extinction. In this respect the whole range of particle sizes is divided in equal steps and for each step the optical properties are evaluated; consequently all the contributions are added together, according to their *weight* given

by the particle size distribution. Finally, the optical properties are obtained that characterize a cloud formed by an ensemble of spherical particles with different sizes and made of ice.

4.6.4 The Double-Precision Lorenz-Mie Scattering Code

There are several open source codes that evaluate the efficiency factors of spheres using the solutions of Mie theory. Within this work the code used for the optical properties calculations of spherical particles is the so called double-precision Lorenz-Mie scattering code[2] developed by M. Mishchenko [86].
The program computes far-field light scattering by polydisperse homogeneous spherical particles using the Lorentz-Mie theory. The input parameters involved in the calculations are [85]:

i. the particle size distribution;

ii. the wavelength of incident light;

iii. the real and imaginary part of the refractive index;

iv. the desired numerical accuracy;

v. the number of integration subintervals on the interval of particle radii;

vi. the number of Gaussian division points on each of the integration subintervals;

vii. the number of scattering angles at which the scattering matrix is computed.

For the calculations of ice particles forming cirrus in the tropical tropopause layer, the input parameters are determined in the following way.

[2] http://www.giss.nasa.gov/staff/mmishchenko/t_matrix.html

For the particle size distributions, two different distributions are used. According to Eq.4.47, the gamma distribution is selected to describe small spheres, i.e. radii ranging in the interval $[0-50]\mu m$, while for larger particles the lognormal distribution is used. For the lognormal distribution, defined in Eq.4.51 as a function of the $IWC_{>50}$ and the temperature, the radii interval is $[50-200]\mu m$. It has to be emphasized that the particle size distributions are parameterizations of the IWCs, therefore the optical properties calculated via Mie theory are fully determined for any given IWC or equivalently any given particle size distribution (PSD). In this respect, we select several $IWCs_{<50}$ for small particles in the interval $[10^{-5}-0.7]gm^{-3}$ with different steps providing 43 different gamma distributions as inputs to the Lorentz-Mie code. The steps follow a base-10 logarithmic scale, since the $IWCs_{<50}$ interval has to cover several orders of magnitude. Similarly, the lognormal distributions generated as a function of the $IWCs_{>50}$ for large particles are 28 with the $IWCs_{>50}$ ranging with different steps in the interval $[10^{-4}-0.1]gm^{-3}$. Also in this case, the steps follow a base-10 logarithmic scale. The relative effective radii for the gamma and the lognormal distributions, evaluated via Eq.4.59, are plotted in Fig.4.24 where each point represents a specific IWC.

Regarding the wavelengths interval, the calculations are performed for 512 wavelengths equally spaced in the interval $[900-1700]nm$.

The real and imaginary parts of the refractive index for ice are chosen according to [128]. They are plotted in Fig.4.25 and, as input to Mishchenko's code, the values are linearly interpolated on the 512 wavelengths of the interval $[900-1700]nm$.

The numerical accuracy required for the optical properties calculations is fixed, for each wavelength, to 10^{-7}. This choice guarantees an accuracy several times better than

the RTM simulations, which is commensurate to the $S/N \sim 300$ of the low-resolution instrument.

The number of integration subintervals on the whole interval of particle radii is fixed to 100.

The number of Gaussian division points on each of the integration subintervals is fixed to 100. The Gaussian quadrature evaluates the Legendre polynomials. It means that in each subinterval, the phase function can be expressed as an expansion of Legendre polynomials weighted with the standard expansion coefficients (see the general form of the phase function in Eq.4.8). The computation of the expansion coefficients requires to solve an integral which is replaced by a Gaussian quadrature formula. The user can change the number (N) of the division points keeping in mind that the computing time largely increases with N [85].

Finally, the scattering matrix is computed for 19 different scattering angles. The formula used for the angle division is given by $180(I-1)/(NPNA-1)$ where the angles are expressed in degree. The parameter NPNA is the number of different scattering angles and in the present calculations is fixed to 19. The index I numbers the angles so that the computation is made dividing the 180° in 18 parts or, equivalently, a step of 10° from 0° to 180° is used in order to compute the scattering matrix.

Next, the outputs of the Mishchenko's code are described. Briefly, they are:

i. the effective radius of the size distribution, i.e. r_{eff};

ii. the average extinction and scattering cross-sections per particle, i.e. C_{ext} and C_{sca};

iii. the single scattering albedo, i.e ϖ_0.

iv. the asymmetry parameter, i.e. g;

The effective radius is calculated according to Eq.4.59 and the resulting effective radii as a function of the IWC and assumed PSDs are displayed in Fig.4.24.
Once the cross-sections are computed, for each particle size distribution, it is easy to obtain the efficiency factors for extinction and scattering (Eq.4.76). In the case of many particles with different sizes, G is given by the average projected area per particle (the average radius is an output of the code but it can also be calculated outside the code starting from the particle size distribution). The efficiency factor for absorption is easily obtained via the energy conservation law expressed by Eq.4.77.
The single scattering albedo ϖ_0 (see Eq.4.7) can be obtained directly from the cross-sections, or equivalently from the efficiency factors, as

$$\varpi_0 = C_{sca}/C_{ext} = Q_{sca}/Q_{ext} \tag{4.83}$$

Finally, the asymmetry parameter g, is the average cosine of the scattering angle

$$g \equiv < \cos\theta > = \int_0^{2\pi}\int_0^{\pi} p(\theta,\phi)\cos\theta\sin\theta d\theta d\phi \tag{4.84}$$

where $p(\theta,\phi)$ is the phase function. The asymmetry parameter specifies the degree of scattering in the forward direction ($\theta = 0°$). It varies from -1 (i.e. all radiation is backward scattered like a *mirror*) to 1 (for pure forward scattering). Generally speaking, if a particle scatters more light toward the forward direction, $g > 0$; $g < 0$ if the scattering is directed more toward the back direction; $g = 0$ if it scatters light isotropically (e.g. small particles in the Rayleigh regime, see section 4.5.2).

4.6.5 The Henyey-Greenstein Phase Function

In radiative transfer modeling, the empirical Henyey-Greenstein (HG) phase function it is often used to represent the anisotropic scattering properties of particles [39]

$$p(\cos\Theta) = \frac{1}{4\pi}\frac{1}{(1+g^2-2g\cos\Theta)^{3/2}} \tag{4.85}$$

where g is the asymmetry parameter. The Henyey-Greenstein phase function is normalized such that the integral over the solid angle is equal to 1. In Fig.4.26 the HG phase function in polar coordinates is shown. For the calculations an average asymmetry parameter of 0.85 is used which is a typical value derived from the optical properties of ice particles (see Fig.4.27, bottom right panel).

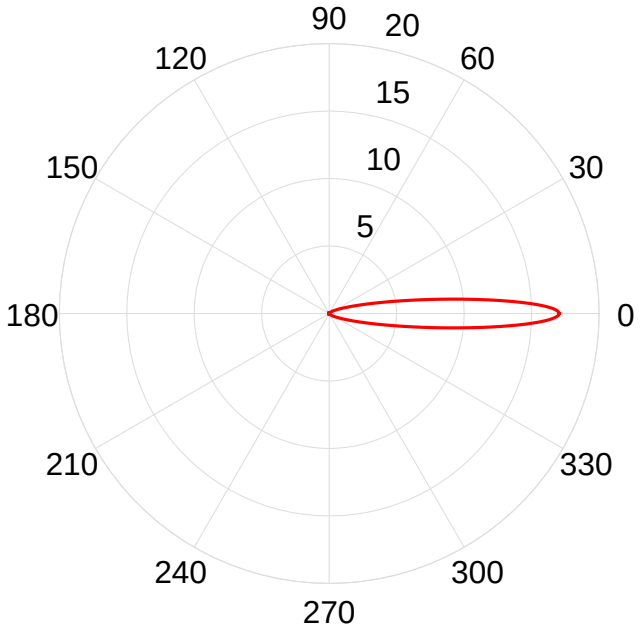

Figure 4.26: Henyey-Greenstein's phase function in polar coordinates ($g = 0.85$).

The phase diagram (Fig.4.26) shows the strong anisotropy characteristic of particles made of ice. The unpolarized radiation is scattered basically in the forward direction ($\theta = 0°$). In fact, the 1-parameter (g) modeled HG phase function is a probability density function in angle space. Any deviation of the phase function from isotropy corresponds to a directional correlation between incident and scattered photons [79].

This optical property of ice particles is fundamental in the following discussions because

it supports the sensitivity of limb observation for optical cloud detection. In fact, the anisotropic scattering behavior allows to have a privileged observation direction when the detector is looking horizontally within a cirrus cloud.
In this work we use the Henyey-Greenstein phase function in order to account for the anisotropic scattering caused by the assumed spherical cirrus particles.

4.6.6 The Optical Properties of Ice Spheres

The input parameters for the RTM spectral radiance simulations in cloudy sky are: the asymmetry parameter, the single scattering albedo, and the extinction coefficient (km^{-1}). The extinction coefficient in terms of the optical properties of an ensemble of particles is evaluated from

$$\epsilon_{ext} = C_{ext} \times \frac{IWC}{\rho \frac{4}{3}\pi \bar{r}^3} \tag{4.86}$$

where the IWC has to be the same used in the particle size distribution parameterization (see Eq.4.47 and Eq.4.51), ρ is the density of ice ($0.91[g/cm^3]$) and $\bar{r}$ is the average radius retrieved from the selected particle size distribution. The second factor in Eq.4.86 represents the concentration of the ice particles within the cloud.
In Fig.4.27 the optical properties obtained from the Mishchenko's code for Mie scattering calculations are displayed as function of the indicated parameters. The small particles are described by a gamma distribution with an ice water content of $0.001 g m^{-3}$, while the larger particles are described by a lognormal distribution with the same amount of ice water content and a temperature ranging in the interval $[-70, -60]°C$.
The simulations indicate that for the same amount of ice the bigger particles tend to absorb more radiation compared to smaller particles (see the behavior of the single scattering albedo). Further, the bigger particles scatter more anisotropically than the smaller particles (see the asymmetry parameter). These are very important properties since once knowing the optical depth of the cloud (i.e. ϵ_{ext} and the cloud bottom/top)

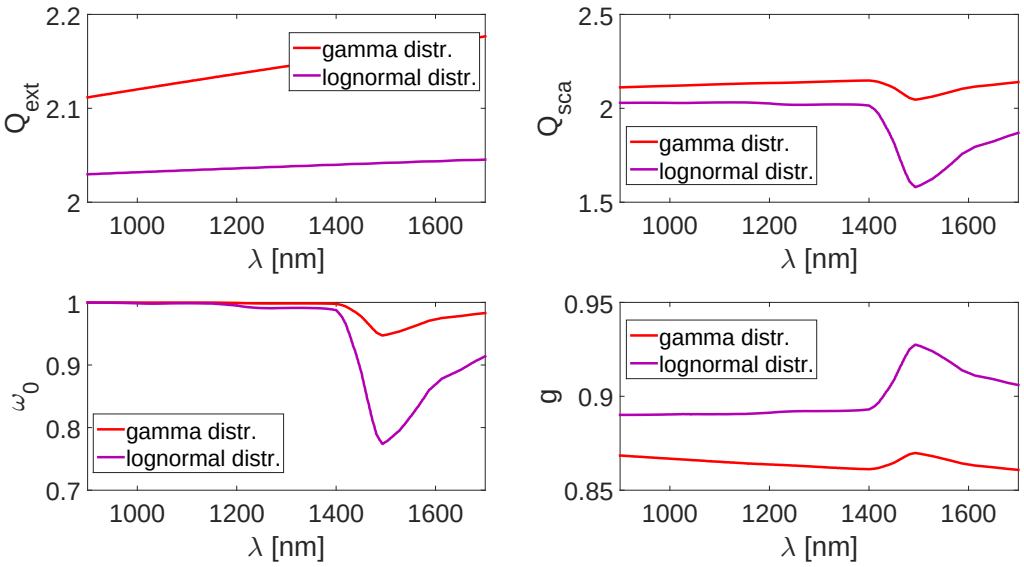

Figure 4.27: Efficiency factors for extinction (top left) and for scattering (top right), single scattering albedo (bottom left) and asymmetry parameter (bottom right) as a function of wavelength. The small particles are described by the gamma distribution for an IWC of $0.001\,\mathrm{g\,m^{-3}}$. Similarly, the parameters are shown for the lognormal distribution and an IWC of $0.001\,\mathrm{g\,m^{-3}}$, with a temperature ranging in the interval $(-70°, -60°)$.

the absorption of ice particles can be studied. As clearly visible in Fig.4.27 the absorption of ice has a peak around $1490\,\mathrm{nm}$ and inspecting the behavior of the scattering efficiency factor as well as the single scattering albedo, it is possible to find the correct mixing ratio of small and large particles. In the following chapter this approach is investigated.

Evidently for the same amount of ice, small particles have higher concentrations than large particles since the mean radius is smaller. Using the second factor of Eq.4.86 and fixing an ice water content of $0.001\,\mathrm{g\,m^{-3}}$ for both sizes of particles, the concentration for small particles would be $\sim 0.77\,\mathrm{cm^{-3}}$, and for larger particles $\sim 6.62 \times 10^{-4}\,\mathrm{cm^{-3}}$. Hence, the difference in the number density is more or less of three orders of magnitude. Therefore, the extinction coefficient (see Eq.4.86) differ for both types of particles, assuming

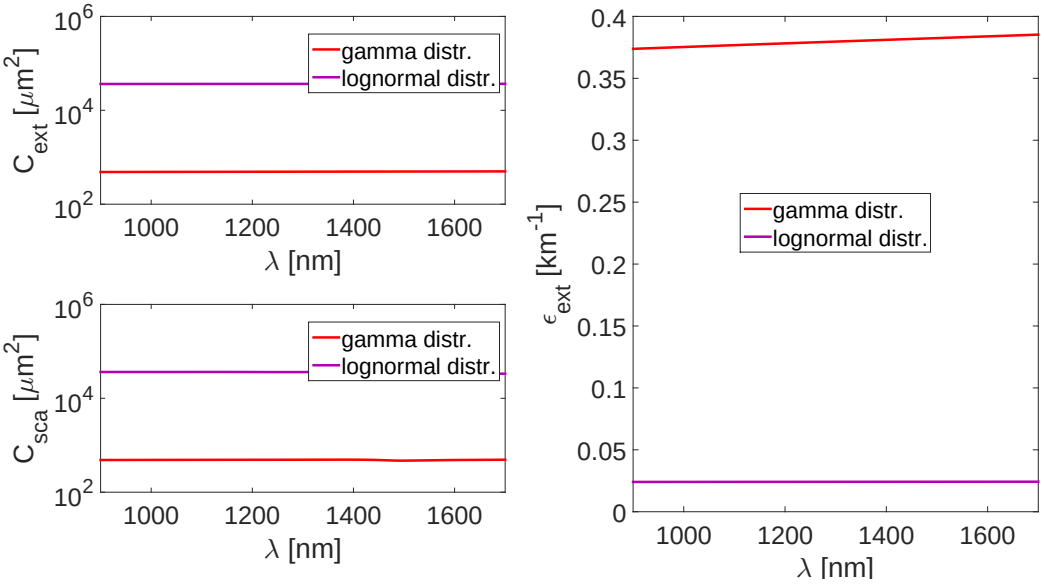

Figure 4.28: The cross-sections for extinction (top left), for scattering (bottom left) and the extinction coefficients (right) are shown. The results are obtained using an $IWC_{<50} = 0.001 g m^{-3}$ for small particles with $r_{eff} = 13.95 \mu m$. Similarly, the results for large particles ($r_{eff} = 82.55 \mu m$) are obtained for an $IWC_{>50} = 0.001 g m^{-3}$ and a temperature ranging the interval $(-70°, -60°)$.

the same amount of IWC.

Fig.4.28 displays the extinction and scattering cross-sections as well as the extinction coefficients calculated from Eq.4.86.

As pointed out before, the larger extinction cross-section for bigger particles intuitively derive from their larger geometric area as compared to small particles. Large particles can extinct more radiation, but fixing the ice water content, the concentration of larger particles is lower resulting in a smaller extinction for the ensemble of big particles as compared to small particles. This result derives from the parameterizations in terms of IWCs involved in the particle size distributions and their averaged properties in the treatment of an ensemble.

4.7 Flowchart of the RTM Simulations

The flowchart in Fig.4.29 summarizes how the simulations of the radiative transfer model are performed in the present work. They represent the basis for the simulations of spectral radiance with which the near-IR measurements are compared. Together they form the pillars of the final results of this work.

The algorithm is written in Matlab and runs in a completely automatic way once the initial parameters are given.

It first loads the detector characteristic and the solar spectrum, then it loads the geometric coordinates specified by the selection of a particular spectrum (the number of the spectrum is one of the input parameters).

After, it evaluates the ocean surface albedo and it loads the cross-sections of the different gases depending on pressure and temperature.

Here, the user can select in between the line by line cross-sections and the cross-sections evaluated via the CKD method.

Finally, the optical properties of ice particles can be selected by choosing in between small or big particles (i.e. gamma or lognormal distribution) as well as both sizes; the input parameters in this case are: the ice water content for small and large particles, and the cloud bottom/top. Thus, the code interpolates the optical properties of ice particles between the ice water contents (i.e. between the PSDs) and uploads, for each wavelength, the specific optical parameters.

When the simulation ends, the spectral radiance is convolved with the instrument slit function (Gaussian function, $\sigma = 10nm$).

In the beginning of the simulation the user can choose the number of photons for each wavelength, as well as the numbers of computer cores for the calculations in parallel. The code also reports the total time (in seconds) for the simulation.

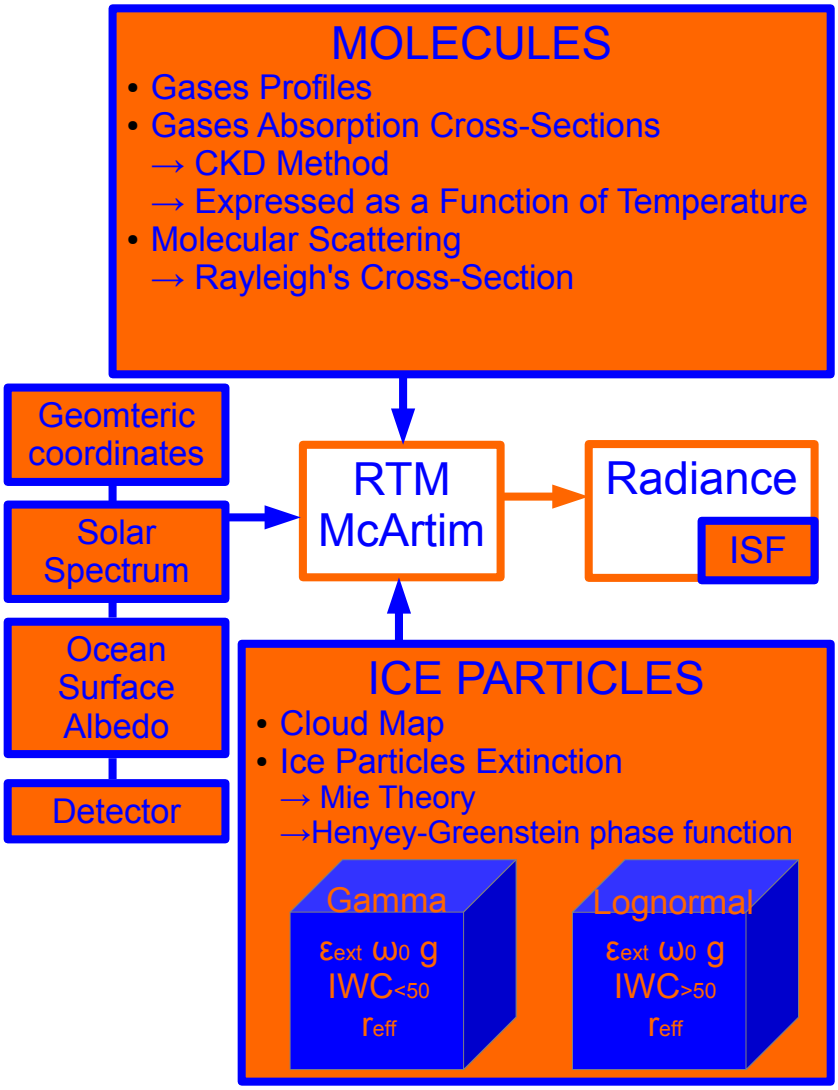

Figure 4.29: Flowchart of the radiative transfer simulations.

5

The Retrieval Procedure

In this chapter the procedure developed for the retrieval of cirrus optical properties are described.

First, some basic concepts of the Differential Optical Absorption Spectroscopy (DOAS) are reported.

Following the full spectral retrieval in the near-IR is explained. It makes use of two wavelengths intervals. The oxygen absorption band ($1.27\mu m$) is used to infer cloud optical depths and extinction coefficients, and the ice absorption band ($1.49\mu m$) is used to infer the ice water contents as well as ice water paths.

The estimation of the errors concerning the retrieval procedures is also reported.

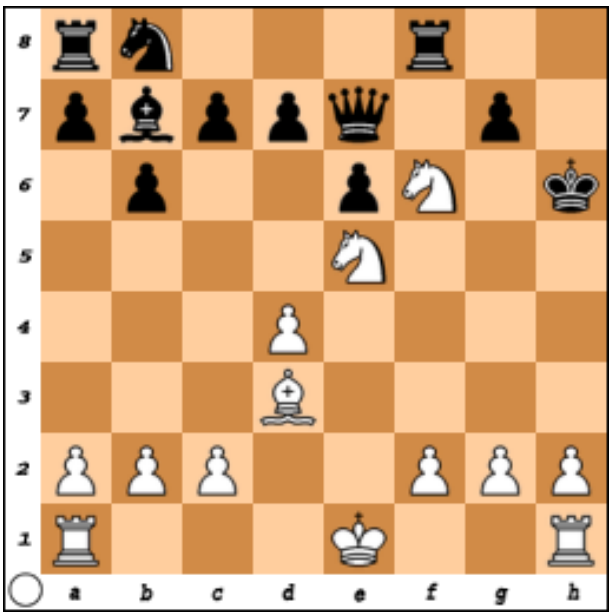

Figure 5.1: E. Lasker vs. G. A. Thomas (London, 1912). Queen's sacrifice, prior to the brilliant strategy to victory.

5.1 The DOAS Method

The Differential Optical Absorption Spectroscopy (DOAS) is a widely used technique in atmospheric research for the detection of different trace gases [98]. The basis of this spectroscopic measurements is the Beer-Lambert's law, which describes how light is extincted by matter when the radiation travels through a medium

$$I(\lambda) = I_0(\lambda) \cdot \exp(-\sigma(\lambda) c L) \tag{5.1}$$

where $I_0(\lambda)$ represents the incoming radiation, $I(\lambda)$ is the radiation after the extinction process, $\sigma(\lambda)$ is the extinction cross-section of the medium, c the concentration of the parcels forming the medium and L is the light path through the medium. The product $\sigma(\lambda)cL$ is called the optical depth of the medium; it is usually indicated with $\tau(\lambda)$ or $OD(\lambda)$. Since the Beer-Lambert's law is applied to the atmosphere which is a complex interacting system, Eq.5.1 has to consider the presence of multiple gases which can absorb according to their absorption cross-sections and they can scatter via Rayleigh scattering. Furthermore, the Beer-Lambert's law has also to consider the extinction process caused by particles forming clouds or aerosols and even in this case they can absorb the radiation according to their absorption cross-sections as well as scatter the radiation via Mie scattering. Finally, since the measured spectral radiance are collected with a specific instrument, also the instrumental effects must be taken into account. Hence, Eq.5.1 is best represented by the form

$$I(\lambda) = I_0(\lambda) \cdot \exp\Big[- L\Big(\sum_{j=1}^{n} (\sigma_j(\lambda) c_j) + \epsilon_R(\lambda) + \epsilon_M(\lambda) \Big) \Big] A(\lambda) \tag{5.2}$$

where n is the number of considered gases, $\sigma_j(\lambda)$ represents the absorption cross-section for each gas as well as c_j is the concentration for the specific $j-$gas. $\epsilon_R(\lambda)$ is the Rayleigh scattering occurring for the gaseous molecules while $\epsilon_M(\lambda)$ is the extinction caused by particles, where M refers to Mie theory; finally $A(\lambda)$ is the wavelength

dependent sensitivity of the instrument. To determine the concentration of a particular gas, it would in principle be necessary to quantify all other factors influencing the radiative transfer process. The DOAS technique overcomes this issue by separating the broadband effects due to either particle extinction processes and molecular absorptions from narrowband effects. In fact, certain gases exhibit narrowband absorption structures. The foundation of DOAS is thus to separate broad and narrowband spectral structures in order to isolate these narrowband components. In Fig.5.2 the DOAS principle is shown. The basic idea behind the method is to identify peculiar absorption features which derive from the cross-section of a specific parcel. These narrowbands features act like a fingerprint of the molecule and the identification of them leads to the detection of the gas concentration as well as to several other information.

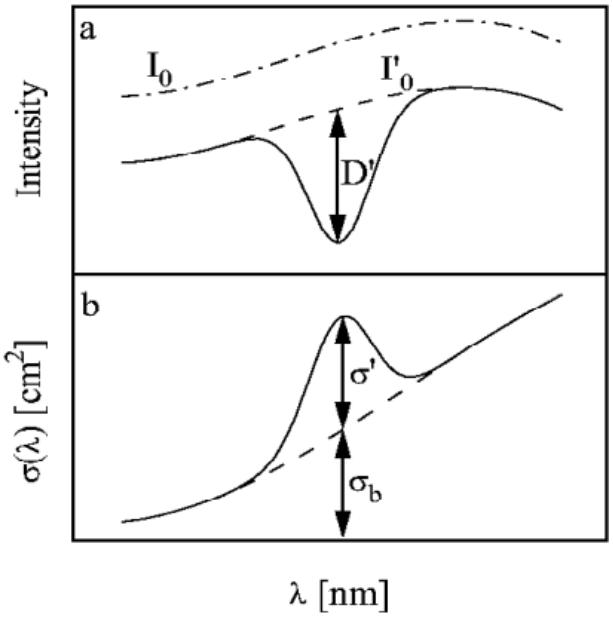

Figure 5.2: Principle of DOAS: $I_0(\lambda)$ and $\sigma(\lambda)$ are separated by an adequate filtering procedure into a narrow ($D'(\lambda)$, and $\sigma'(\lambda)$) and broad band part ($I'_0(\lambda)$ and $\sigma_b(\lambda)$). Adapted from [98].

In the present work, it is made use of the medium-broadband absorption features, since in the near-IR interval nor the molecules nor the particles show narrowband components.

5.2 Optical Properties Retrieval for Cirrus

The retrieval procedure for the optical properties of ice cirrus is set up as following. The first step is to use the DOAS method on the absorption band of a gas with known

concentration, and specifically the oxygen absorption band ($^1\Delta_g \leftarrow^3 \Sigma_g^-$) occurring at 1.27$\mu$m, in order to infer the vertical optical depth of the cloud.

After, the ice absorption band occurring around 1.49μm is used, in order to infer the mixing ratio of small to big ice particles within the cirrus cloud and then the total ice water content.

5.2.1 Oxygen Absorption Band Analysis - Part I

Oxygen is a molecule with well-known mixing ratio in the atmosphere ($MR_{O_2} = 20.95\%$) and therefore, using a tropical temperature and pressure profile, it is easy to get the concentration. Fig.5.3 shows an example of a collected spectrum in cloudy sky (left panel) from SF2-2013 and the relative absorption band caused by oxygen and used

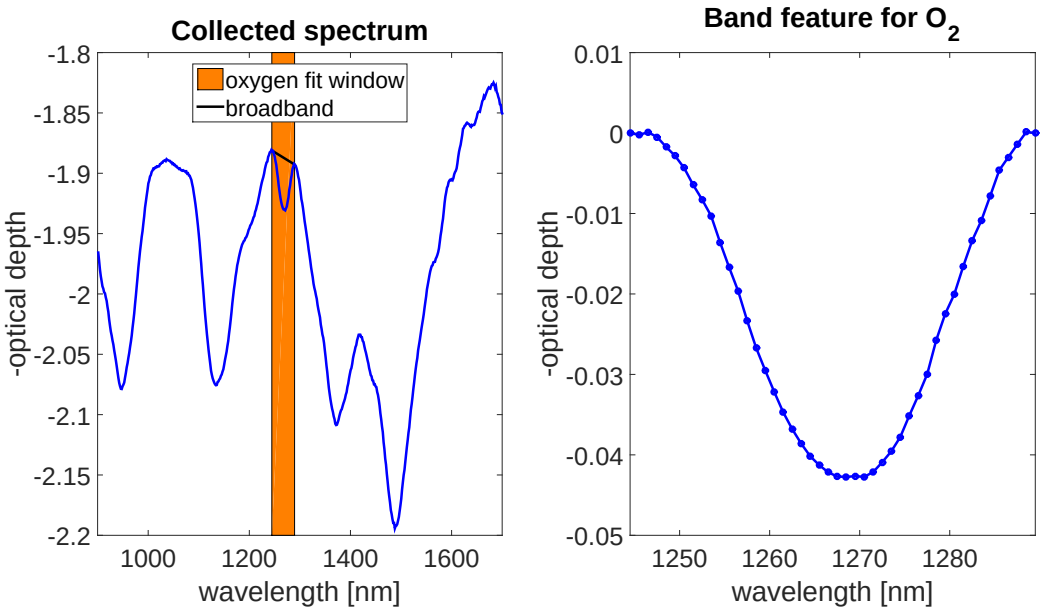

Figure 5.3: On the left panel an example of a collected spectrum in cloudy sky from SF2-2013 is plotted. In orange it is highlighted the wavelengths interval for the fit analysis ($[1244.5 - 1289.5]$nm) on the oxygen band (1.27μm). The black line indicates the broadband part of the spectrum. On the right panel the absorption band caused by oxygen is shown.

for the fitting procedure (right panel).

The fit range is chosen according to the oxygen absorption band occurring at $1.27\mu m$ ($7874 cm^{-1}$) [114]. The wavelengths interval is $[1244.5 - 1289.5]nm$, and for the central wavelength of the band $1267.5nm$ is used. The band feature, shown on the right in Fig.5.3, is like the D' of Fig.5.2, while the broadband component (black line in the left panel) acts like the I_0' of Fig.5.2.

For each collected spectrum in cloudy sky, it is possible to extract the optical depth of oxygen OD_{meas} at $\lambda = 1267.5nm$.

The optical depth of the oxygen absorption band ($^1\Delta_g \leftarrow^3 \Sigma_g^-$) in presence of a cirrus cloud can change because ice particles modify the spectral radiance according to their scattering properties. In this respect some sensitivity studies are conducted in order to investigate how the oxygen absorption band changes due to the presence of a cirrus cloud.

The simulations (shown in Fig.5.4) are done by varying the concentration of ice particles, in other terms the ice water content that affects also the cloud optical depth (OD_{cloud}); all the other parameters are kept fixed. Inspecting the wavelengths interval $[1244.5 - 1289.5]nm$, it becomes evident how the optical depth of oxygen changes increasing the ice water content. On the other hand, also a deeper ice absorption band ($1490nm$) is clearly visible since the increasing ice water content changes the ice absorption as well as the radiative transfer.

The absorption band of oxygen is mostly affected by scattering effects in presence of a cirrus made of ice (see the behaviors of the SSA ϖ_0 and the asymmetry parameter g in Fig.4.27). Therefore, from the oxygen fitting window, it is possible to infer the vertical optical depth of the cloud in that particular wavelengths interval, since the extinction is mostly due to scattering.

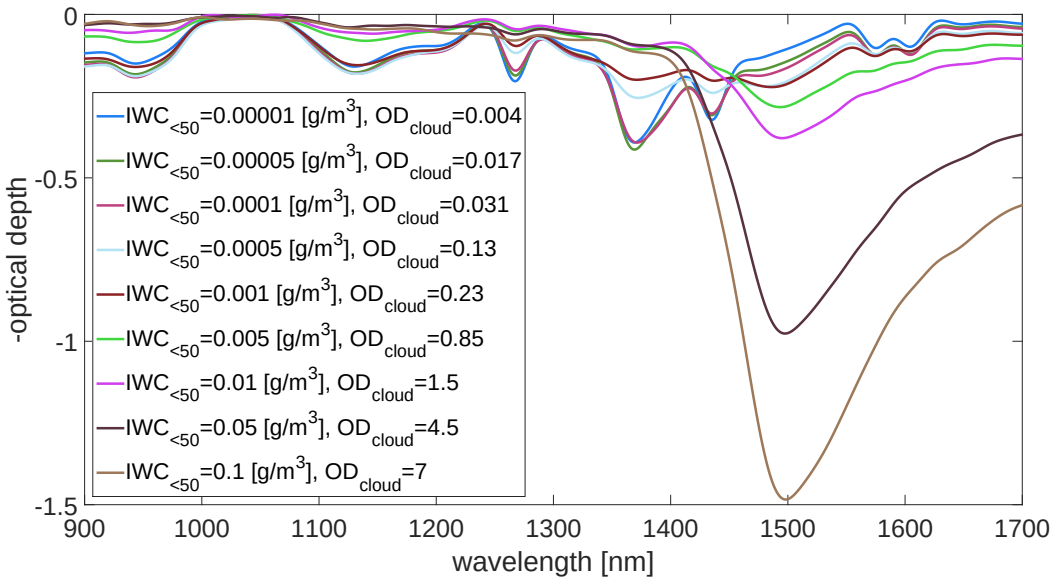

Figure 5.4: RTM simulations for $\log(I/I_0)$. In the simulations, the detector is looking at $-0.5°$, the altitude is 15.3km and the cloud is placed between 15.2km and 15.8km. Only small particles described by a gamma distribution are considered. In the legend, the different IWCs and cloud ODs are shown.

The vertical optical depth of a cirrus made of ice particles is inferred as following. The simulations are executed using only one particle size distribution (the gamma distribution), in other terms only particles with radii in the interval $[0-50]\mu m$. This can be done because in the oxygen fit window the ice absorption is very weak.
Starting with an initial ice water content ($IWC^0_{<50}$), the retrieval code runs in a loop, following the steps:

i. the optical properties for the cirrus with an $IWC^0_{<50}$ are extrapolated from the Mie calculations and uploaded in the RTM;

ii. the model can run in parallel (using all the CPU available on the machine) providing the spectral radiance for the wavelengths interval $[1244.5-1289.5]nm$ with a $1nm$ step;

iii. the simulated spectral radiance is convolved with the instrument slit function and the optical depth is obtained using the logarithmic function;

iv. making use of the DOAS technique, the broadband part of the absorption band is removed (following the same procedure used for the collected spectra, see right plot of Fig.5.3), obtaining the simulated band feature of the oxygen OD_{sim};

v. the simulation is fitted with the measurement, taking into account as central wavelength of the band $1267.5nm$; if the convergence criterion is satisfied, the fitting procedure ends, else the loop run again from the beginning with a new ice water content.

The convergence criterion is selected according to the instrument limitations since, even if instrumental errors are difficult to quantify, for DOAS observations in the near-IR they are typically in the range of $2\% - 3\%$ [98]. Thus, we select an average relative error of 3% on the collected radiances [118].
Hence, the first iteration starts with an initial ice water content $IWC^0_{<50}$ which provides the optical properties for the cirrus, or equivalently the extinction coefficient ϵ^0_{ext} (see Eq.4.86). The cloud optical depth is then calculated from

$$OD^0_{cloud} = \epsilon^0_{ext} \times H_{cloud} \tag{5.3}$$

where H_{cloud} is the vertical extension of the cloud (evaluated from the CPL data). When the precision criterion is not achieved after the first iteration, a new cloud optical depth at $\lambda = 1267.5nm$ is calculated, using the simple relation

$$OD^n_{cloud} : OD^{n-1}_{cloud} = OD^{n-1}_{sim} : OD_{meas}; \qquad n = 1, 2, 3, \ldots \tag{5.4}$$

where n is the number of iterations. This relation defines a linear equation which links the cloud optical depth (OD_{cloud}) with the changing optical depth for the oxygen

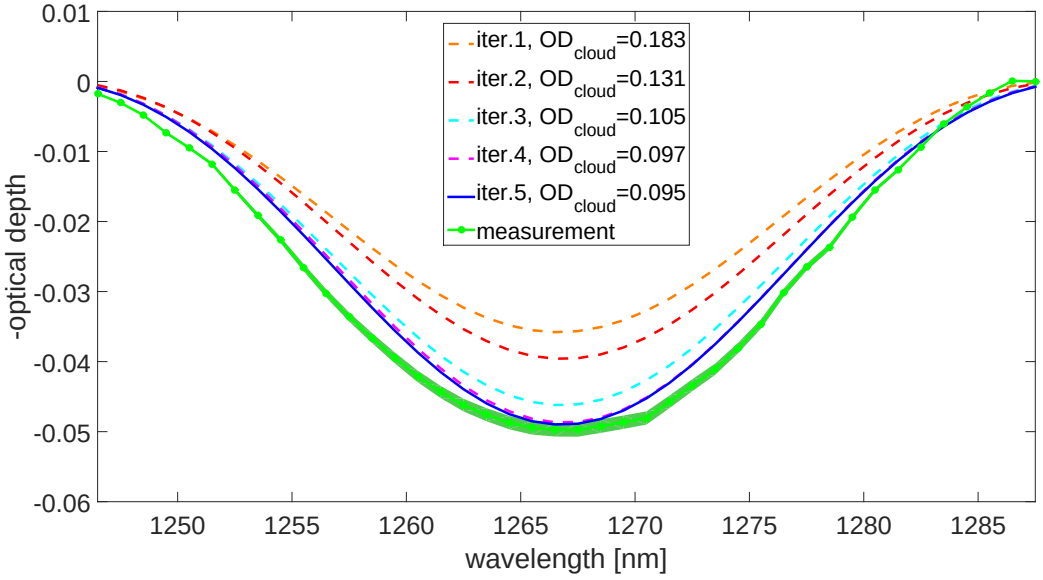

Figure 5.5: Example of the iterating procedure used to infer the oxygen OD_{meas}. The first iteration highlights the initializing point and after, by making use of Eq.5.5, the next iteration starts until the convergence criterion is satisfied. The green shadowed region represents the error of the retrieval (see Eq.5.7).

absorption band (OD_{sim} is the simulated one, while OD_{meas} is the measured one) due to the presence of ice particles

$$OD^{n}_{cloud} = \frac{OD^{n-1}_{cloud} \times OD^{n-1}_{sim}}{OD_{meas}}; \qquad n = 1, 2, 3, \ldots \tag{5.5}$$

Eq.5.5 shows that the oxygen absorption band depends on the cloud optical depth. The linear relation between cloud optical depth and oxygen absorption band can be derived from the Beer-Lambert's law (see Eq.5.1).

The new cloud optical depth OD^{n}_{cloud} identifies uniquely a new extinction coefficient via Eq.5.3, and hence, a new ice water content is also derived, using Eq.4.86.

The loop only ends when the precision criterion is reached and the OD_{cloud} is finally inferred. When the first spectrum is evaluated, the code automatically goes to the next spectrum and uploads all the new input parameters like geometric coordinates, ground

albedo, et cetera. The starting ice water content for the loop is now selected according to the previous inferred cloud optical depth. In other terms the inferred $\mathrm{OD}_{\mathrm{cloud}}$ of one collected spectrum represents the initial $\mathrm{OD}^{0}_{\mathrm{cloud}}$ for the following fitted spectrum. This choice allows to have a certain continuity during the fitting procedure for a multitude of spectra and provides the best initial IWC condition.

In Fig.5.5 an example of the fitting procedure is shown. In this case the convergence criterion is reached after five iterations. The average for the number of iterations is about 4.4, and using 7 CPU in parallel with a processor Intel(R) Core(TM) i7-4770 CPU @ 3.40Ghz, one iteration lasts less than 10 minutes.

In conclusion, after the procedure used to infer the cloud optical depth from the collected spectra is described, the discussion addresses another aspect of the analysis. In order to have a unique solution for the inferred cloud optical depth, it is necessary to work with a good characterization of the cirrus morphology. Looking at Eq.5.3, it is clear that the input parameter for the optical properties of ice particles is the extinction coefficient (and hence the ice water content), but the optical depth links the extinction coefficient to the vertical extension of the cloud. Therefore, if the bottom/top of the cloud is not known at all, it is impossible to infer a unique solution for the extinction coefficient, because changing the height of the cloud propagates into a variation of the $\mathrm{OD}_{\mathrm{cloud}}$ for a fixed extinction coefficient.

To overcome this ambiguity, the CPL data or any a priori information on the cloud height and vertical extension are helpful in order to have the best representation for the bottom/top cirrus. Inspecting Fig.3.5, it is possible from the CPL data to extrapolate the altitude for the cloud bottom/top and then to use these informations as input to the RTM.

5.2.2 Convergence Criterion and Estimation of the Errors

The relative error of the measured spectral radiance is assumed to be 3% [118]. The optical depths are calculated using Eq.5.1 ($OD_{meas}(\lambda) = -\ln(I(\lambda)/I_0(\lambda))$); therefore, in order to define the convergence criterion, we use the variance formula that, neglecting correlations and assuming independent variables, leads to calculate the error propagation as follows

$$\Delta f = \left(\sum_{i=1}^{n} \left(\frac{\partial f}{\partial x_i} \Delta x_i \right)^2 \right)^{1/2} \tag{5.6}$$

The equation of errors propagation, in our case, translates into

$$\Delta OD_{meas}(\lambda) = \sqrt{2} \times 0.03 \tag{5.7}$$

where 0.03 is the starting relative error of the collected radiances (3%), and the factor $\sqrt{2}$ derives from Eq.5.6.

For each collected spectrum, the retrieval error is evaluated via Eq.5.7. This error is chosen as convergence criterion for the fit. When the iterating procedure starts, the simulated optical depth is fitted to the measurement as follows

$$OD_{sim}(\lambda = 1267.5) \in [OD_{meas}(\lambda = 1267.5) \pm \Delta OD_{meas}(\lambda = 1267.5)] \tag{5.8}$$

When this condition is satisfied, the loop ends, and when not the iteration proceeds to the next step.

We also assess the error on the simulated radiances. The Monte Carlo algorithm based on probability density functions is subjected to statistical noise (Poisson noise). The Poisson noise decreases when more photons are used for the simulations (see subsection 4.2.1). Since the RTM is set up with 10^5 photons for each wavelength, the Monte Carlo algorithm estimates that the averaged relative error on the simulated spectral radiance is less than 1% (ca. 0.93%). However, this is the relative error for the spectral radiance at high resolution and not for the convolved spectral radiance. As described in section

4.3, the simulated high resolved spectral radiance are convolved with the ISF before being compared to the measured radiances. Therefore, it is necessary to find an error on the convolved simulated radiances. The operation of convolution is defined as the integral of the product of two functions (f and g)

$$(f * g)(t) = \int_{-\infty}^{\infty} f(\tau)g(t-\tau)d\tau \tag{5.9}$$

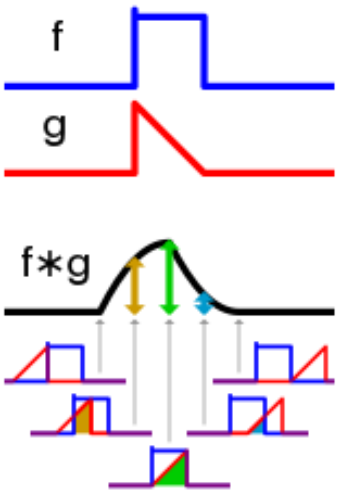

Figure 5.6: Operation of convolution.

In our case the function $f = I_{sim}(\lambda)$ and g is a Gaussian function with $\sigma = 10nm$. In Fig.5.6 a sketch showing the operation of convolution is depicted.

For the estimation of the uncertainty, we use the relative error, derived from the statistical noise of the Monte Carlo algorithm, as upper and lower limits on the f function. In other words, starting from the simulated radiances $I_{sim}(\lambda)$ with their statistical relative error of 0.93%, the upper and lower limits are defined as $f_{+/-} = I_{sim}(\lambda)(1 \pm 0.93\%)$ and the convolution function on both limits is finally applied. The impact of the statistical Monte Carlo noise to the convolved radiances is assessed by averaging the results and finding an averaged relative error of 1%.

To confirm this finding, the error of the simulations is also checked using another approach. Basically it is run ten times the same simulation ($I_n(\lambda); n = 10$), the convolution is applied and the convolved radiances are treated as expectation values without error. Then, the ensemble error is calculated using the standard formula

$$\Delta I(\lambda) = \sqrt{\frac{(I_1(\lambda) - \bar{I}(\lambda))^2 + \ldots + (I_n(\lambda) - \bar{I}(\lambda))^2}{n-1}} \tag{5.10}$$

where n is the number of the runs and $\bar{I}(\lambda)$ is the mean value at a specific wavelength,

or

$$\bar{I}(\lambda) = \frac{\sum_{i=1}^{n} I_i(\lambda)}{n} \tag{5.11}$$

From Eq.5.10 we finally assess an averaged relative error on the simulated spectral radiance of about 1‰. This result is completely in agreement with the previous one, because in this case we average the statistical noise of the Monte Carlo ($\sim 1\%$) running for ten times the same simulation, and therefore the final relative error should be ten times smaller than the previous one. This result confirms also that the convolution function doesn't affect the accuracy of the Monte Carlo model.

Hence, we finally estimate the averaged relative error on the simulated spectral radiance to 1%. Applying Eq.5.6, the final absolute error on the simulated optical depth $OD_{sim} = -\ln(I_{sim}(\lambda))$ is

$$\Delta OD_{sim}(\lambda) = 0.01 \tag{5.12}$$

Since the error of the simulated optical depths is more than three times smaller than the error of the measurements, during the iterative procedure only the experimental error is taken into account.

Now, we want to provide the uncertainties on the retrieved parameters. As said before, the oxygen band analysis ($1.27\mu m$) is developed for the retrieval of the cloud optical depth, and the procedure is a convergent iterative loop. In order to estimate the error on the inferred cloud optical depth, the same simulation is run for 10 times providing 10 different results for the cloud vertical optical depth ($OD^n_{cloud}(\lambda = 1267.5); n = 10$) and ice water content. For the estimation of the absolute error Eq.5.10 is used now with optical depths instead of spectral radiances. Finally, for the retrieved cloud optical depth a relative error of 3.2% is assessed. Similarly, the relative error on the inferred ice water content is estimated to 3.8%.

The error propagation on the optical properties is estimated as follows. Clearly, the cloud optical depth and the extinction coefficient are linked according to Eq.5.3. Conse-

quently, the extinction coefficient has the same averaged relative error of the cloud optical depth, i.e. 3.2%. In order to estimate the error on the single scattering albedo and the asymmetry parameter, two simulations are run. In the first run, an ice water content $IWC_{<50}$ is assumed, and in the second run, an ice water content of $IWC_{<50} \times (1+0.038)$ is used, where 3.8% is the relative error associated to the ice water content. Then the propagation of this uncertainty to the SSA and g is studied, and an averaged relative error of 4.7×10^{-5} for the single scattering albedo and 2.2×10^{-4} for the asymmetry parameter is found.

Similarly, the impact of the IWC uncertainty over the geometric mean radius (Eq.4.57) and the effective radius (see Eq.4.59) is estimated, finding the averaged relative errors of 6.4‰ for the mean radius and 4.8‰ for the effective radius of small particles, and 1.2‰ and 1.7‰ for mean and effective radius of large particles.

5.2.3 Oxygen Absorption Band Analysis - Part II

Once the relative errors for the retrieved parameters are assessed, it is necessary to investigate the impact of large particles on the oxygen absorption band fit. Since small and large particles are differently characterized with respect to the size distribution, a sensitivity study on the optical properties of ice particles and and their contribution to the inferred oxygen OD is performed. In other terms, the optical properties as a function of wavelength of small and large particles having the same extinction coefficient (at $\lambda = 1267.5nm$, i.e. same cloud optical depth) are extrapolated from the Mie calculations and compared. The results are reported in Fig.5.7. It becomes evident that assuming the same extinction for both particle sizes the two ensembles are not equivalent.

By inspecting Fig.5.7 (middle panel), the two ensembles have the same extinction coefficient and, within the error intervals they are the same. Moreover, the extinction coef-

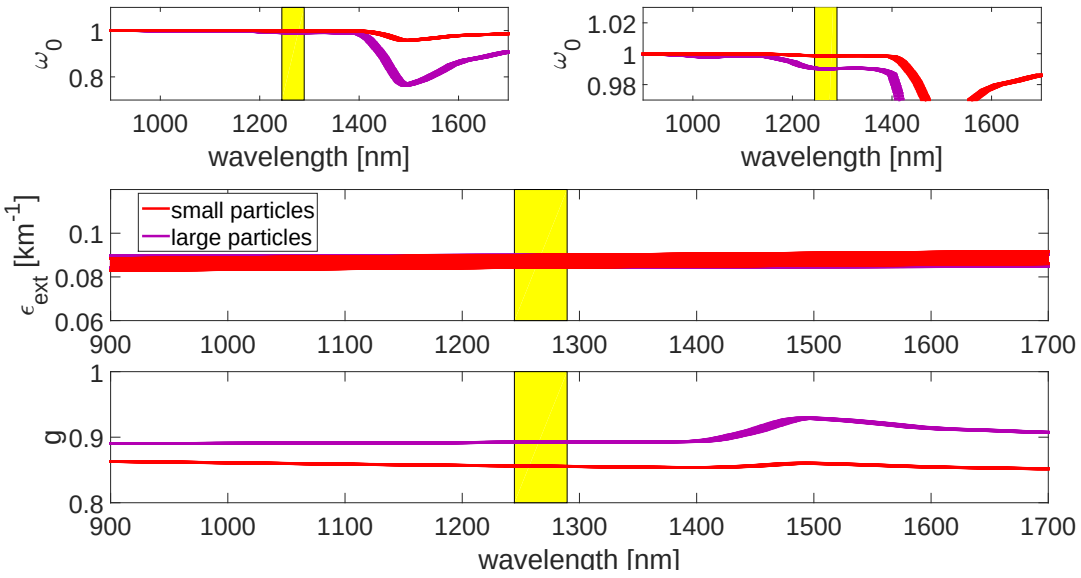

Figure 5.7: Optical properties of small and large particles with same $\mathrm{OD}_{\mathrm{cloud}}(\lambda = 1267.5) = 0.087$. Upper left (right) panel: single scattering albedo (a zoom-in in the oxygen fit range). Middle panel: extinction coefficient. Lower panel: asymmetry parameter. The yellow sector highlights the oxygen fit range ([1244.5-1289.5]nm). The optical properties are reported with the associated inferred errors (see subsection 5.2.2). $IWC_{<50} = 1.8 \times 10^{-4}[\mathrm{g/m^3}]$ and $IWC_{>50} = 3.8 \times 10^{-3}[\mathrm{g/m^3}]$.

ficients for both ensembles are constant for the whole wavelength range and accordingly we can refer to a constant cloud optical depth omitting the wavelengths dependency. Once the cloud optical depth is retrieved for $\lambda = 1267.5\mathrm{nm}$, it can be used for all the near-IR wavelength range (i.e. $[900 - 1700]\mathrm{nm}$).

Secondly, Fig.5.7 (lower panel) indicates that the asymmetry parameter is different for both ensembles. This shows a difference in the radiative transfer mechanism between small and large particles. Large particles tend to have larger asymmetry parameters which is due to the preferred scattering in forward direction as compared to small particles. As a consequence, the photons are constrained to longer paths when the detector is oriented to the horizon within the cirrus (assuming for both particle sizes the same

absorption probability).

Finally, the single scattering albedos differ within the error intervals, e.g. in the oxygen fit range (Fig.5.7 upper panels). Starting with the same extinction coefficient for both ensembles (but different IWCs), large particles absorb more photons as compared to small particles. Therefore, the photon light path within the cloud is shortened as compared to purely scattering particles since there is a higher probability for photons to be absorbed.

In conclusion, the optical properties analysis shows that both particle sizes have to be considered for the retrieval of the cloud optical depth. In fact for large and small particles, the radiative transfer changes slightly in the oxygen fit band. Therefore, two different analysis are run, where the first assumes only small particles and the second assumes only big particles, in order to achieve two boundary limits for the resulting cloud optical depth. In other terms an upper limit and a lower limit suggesting that the expected cloud optical depth is bracketed by this two boundaries.

Since the mixing ratio of small to large particles is somewhat uncertain and it cannot be retrieved using only the oxygen band analysis, a second method is developed. It makes use of the absorption band of ice occurring around 1490nm.

5.2.4 Ice Absorption Band Analysis

In the previous subsections the method developed for the OD_{cloud} retrieval is explained. The discussion includes that the inferred results are obtained using both particle size distributions (not together), in order to retrieve an upper and lower limit for the cloud optical depth.

Furthermore, once the cloud optical depth is inferred at a specific wavelength, the OD_{cloud} can be assumed constant for the whole near-IR range (see the extinction coefficient in Fig.5.7, middle panel). In fact, within the error intervals, it is not wavelength

dependent.

Now, the strategy developed to infer the mixing ratio of small to big particles within a cirrus layer is described. Assuming the two boundary limits for the inferred cloud optical depths, the procedure is executed for both limits and it is explained in detail only for one case.

Starting from a fixed cloud optical depth, it is possible to define two superimposed cloud layers, one described by the gamma distribution and one by the lognormal distribution, such as

$$OD_{cloud} = OD_{gamma} + OD_{lognormal} \tag{5.13}$$

The two cloud layers are superimposed which means that the morphology is the same, i.e. the cloud bottom/top is the same assuming small or large particles. Eq.5.13 can be expressed in terms of the extinction coefficients using Eq.5.3

$$\epsilon_{ext}^{cloud} = \epsilon_{ext}^{gamma} + \epsilon_{ext}^{lognormal} \tag{5.14}$$

The oxygen fitting procedure takes into account only small particles (or only large particles), i.e $\epsilon_{ext}^{cloud} \equiv \epsilon_{ext}^{gamma}$ (or $\epsilon_{ext}^{cloud} \equiv \epsilon_{ext}^{lognormal}$), therefore to account for both particle sizes, ϵ_{ext}^{gamma} has to be decreased and $\epsilon_{ext}^{lognormal}$ has to be increased such that Eq.5.14 is always satisfied. In this view, for each collected spectrum, we generate 9 lookup tables according to the following procedure. ϵ_{ext}^{gamma} is decreased from its initial value $\epsilon_{ext}^{0,gamma}$ (the one retrieved with the oxygen fitting procedure) according to

$$\epsilon_{ext}^{gamma} = i \times \epsilon_{ext}^{0,gamma} \tag{5.15}$$

where $i = 0.1, \ldots, 0.9$ with step 0.1. At the same time the contribution to the cloud extinction coefficient which derives from the lognormal distribution is evaluated via

$$\epsilon_{ext}^{lognormal} = \epsilon_{ext}^{cloud} - \epsilon_{ext}^{gamma} \tag{5.16}$$

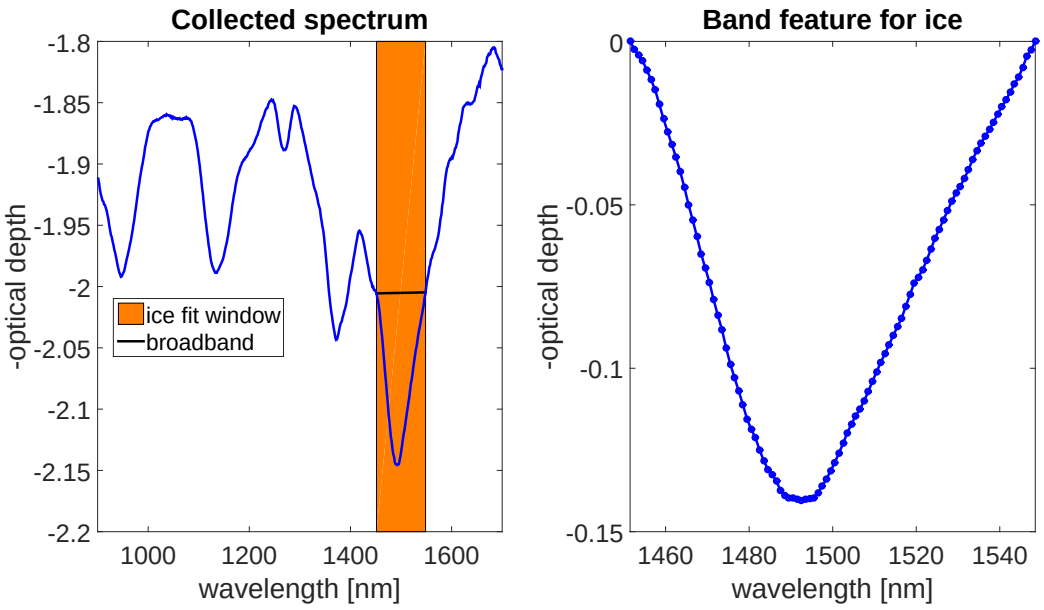

Figure 5.8: On the left panel an example of a collected spectrum in cloudy sky from SF2-2013 is plotted. The orange sector highlights the wavelengths interval for the fit analysis on the ice band, in black the broadband part of the spectrum in the selected fit interval is labeled. On the right panel the selected band feature caused by ice particles is shown.

where $\epsilon_{ext}^{cloud} \equiv \epsilon_{ext}^{0,gamma}$.

For the ice absorption fitting procedure, the wavelengths interval goes from $1451.5nm$ to $1548.5nm$ with a $1nm$ step. As central wavelength for the band $1493.5nm$ is used. The wavelengths interval is selected by inspecting a simulated spectral radiance in clear sky. In fact, looking at the lower panel of Fig.4.20, no absorption features are detected in the above-mentioned wavelengths interval and the main absorption feature in the near-IR caused by ice particles is present within this interval (see Fig.5.7 upper panels). The absorption band of ice is fundamental in order to infer the mixing ratio of small to large ice particles because the band is a representation of the whole ensemble of particles and therefore it shows the overall contributions coming from all particle sizes. The absorption band of ice particles (see Fig.5.8) is extrapolated from the measured

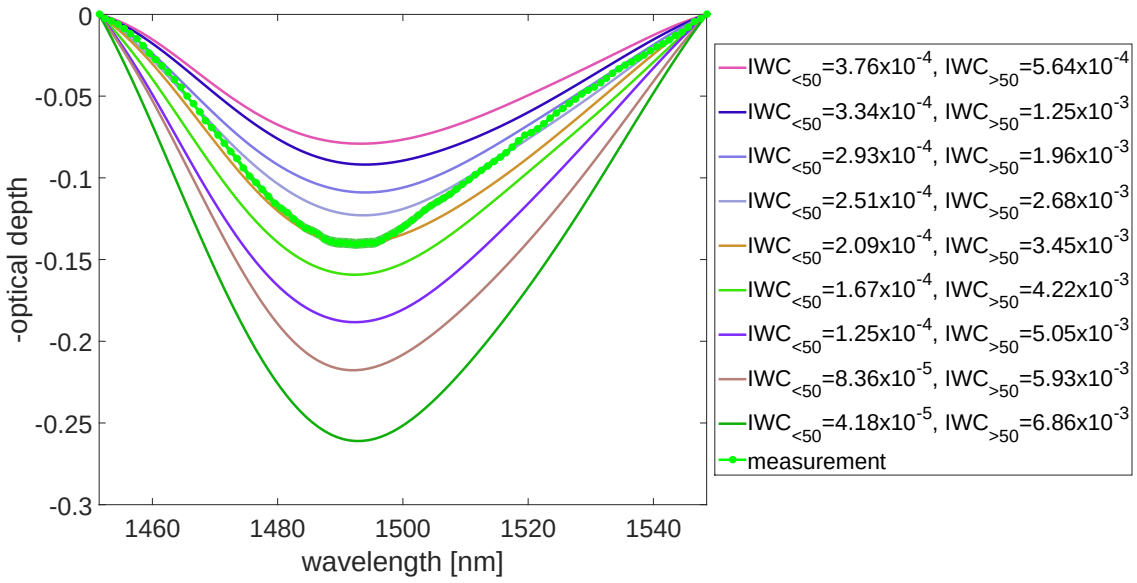

Figure 5.9: Example of the iterating procedure used for the retrieval of the particles mixing ratio. The cloud optical depth is kept fixed ($\mathrm{OD}_{\mathrm{cloud}} = 0.18$) and iteratively the concentration of small particles is decreased while the concentration of larger particles is increased, according to Eq.5.13 and Eq.5.14. The green shadowed region represents the uncertainty of the retrieval (see Eq.5.7).

spectra (as done with the absorption band of oxygen), then it is fitted to the 9 ice absorption bands generated varying the concentrations of small and big particles.

Finally, by interpolation on the 1493.5nm wavelength the mixture of small and large particles is determined.

Fig.5.9 shows an example of the iterating procedure which generates the 9 lookup tables. The cloud optical depth (inferred with the oxygen band approach) is fixed within the simulations. Iteratively the code decreases the concentration of small particles while increases the concentration of larger particles in order to satisfy Eq.5.13.

The same procedure is used for the upper limit of the inferred cloud optical depths, i.e. the results found assuming only large particles in the oxygen band fit. In this case the iteration decreases the extinction of big particles while increases the extinction caused

by small particles. In this manner, the upper and lower bound for the ice water contents ($IWC_{<50}$, $IWC_{>50}$ and IWC_T) is determined.

By using the ice absorption band fit window other important parameters can be inferred such as the photon path length within the cloud. Once the cloud optical depth is inferred (OD_{cloud}), the ice water path (IWP) can be evaluated from the Beer-Lambert's law (Eq.5.1), as follows

$$OD_{sim}(\lambda) = OD_{meas}(\lambda) = \epsilon_{ext}(\lambda) \times IWP(\lambda) \tag{5.17}$$

where IWP is the photon light path within the cloud. OD_{sim} and OD_{meas} are the simulated and measured optical depths at $\lambda = 1493.5nm$. Hence, the photon path length is obtained from

$$IWP(\lambda) = \frac{OD_{sim}(\lambda)}{\epsilon_{ext}(\lambda)} \tag{5.18}$$

where ϵ_{ext} accounts for small and large particles, i.e $\epsilon_{ext} = \epsilon_{ext}^{gamma} + \epsilon_{ext}^{lognormal}$.

It is arguable that there is not a perfect agreement between the simulated and measured band shapes (inspecting Fig.5.9 for the ice band and Fig.5.5 for the oxygen band). Most likely this is due to the Gaussian function used to convolve all the simulated spectral radiance. This function could not represent perfectly the real slit function of the instrument, that can be in principle an asymmetric function. Furthermore, we use the same standard deviation ($\sigma = 10nm$) for the whole wavelengths interval. A more detailed investigation on the instrument slit function may reveal that the Gaussian standard deviation can be expressed as a function of wavelength and thus change over the whole wavelength range. Clearly, a real device cannot work as a perfect ideal instrument and therefore some not-counted effects can appear in the direct comparison with the model.

6

Results and Discussions

Within this chapter, the methods previously introduced are applied to a series of collected data.

First, the selection of the data relevant for the validation of the methods is reported.

Hence, the oxygen band method provides the results for the cloud optical depth. These findings are compared to the data collected by CPL and Hawkeye.

Figure 6.1: "*Scuola di Atene*", Raffaello (1509-1511).

Finally, the mixing ratio of small to large particles is inferred using the ice absorption band method. These results are finally discussed and compared with in situ measurements (Hawkeye, NOAA Water, UCATS and DLH) in order to validate the new methods.

6.1 The Data Selection

Within the NASA ATTREX project, the science flights were divided into two campaigns with different science foci (see section 2.2). During the Guam campaign, all flights were planned with lots of dives (where CPL cannot work) and within an environment with high levels of humidity and frequent cirrus. During the Dryden campaign (on the eastern Pacific), the flights were planned on long straight tracks, with some dives along the path. The sky conditions were almost clear and sometimes CPL and the in situ instruments reported the detection of cirrus. Among the six science flights performed during the Dryden campaign, we focus on the second flight (SF2-2013) where the CPL data for the cirrus morphology are available as well as the Hawkeye, NOAA Water, UCATS and DLH data. During the Dryden campaign, the Hawkeye instrument was not composed by three probes yet (i.e. the spectrometer + the cloud particle imager + the 2D-Stereo probe), but it consisted only of the fast cloud droplet probe (FCDP) standalone (i.e. the spectrometer). Therefore, the data collected by Hawkeye and used in the present work refer to the Hawkeye-FCDP (see section 3.3) and not to the whole instrument used in the Guam campaign.

Fig.3.5 shows the data collected by CPL during a flight segment of SF2-2013. The flight direction was almost straight and few dives were performed. As illustrated in chapter 3, the lidar is an in situ instrument and it points to the nadir direction while the mini-DOAS instrument collects data in remote and it looks in limb direction. Hence, we expect a delay in between the measurements of both instruments of the same cloud part. In other terms, the mini-DOAS instrument points forward to the cirrus layer that is later detected by CPL.

The overall configuration is shown in Fig.6.2 (upper panel). During the first part of the flight segment there was a dive where no data were collected by CPL and the mini-

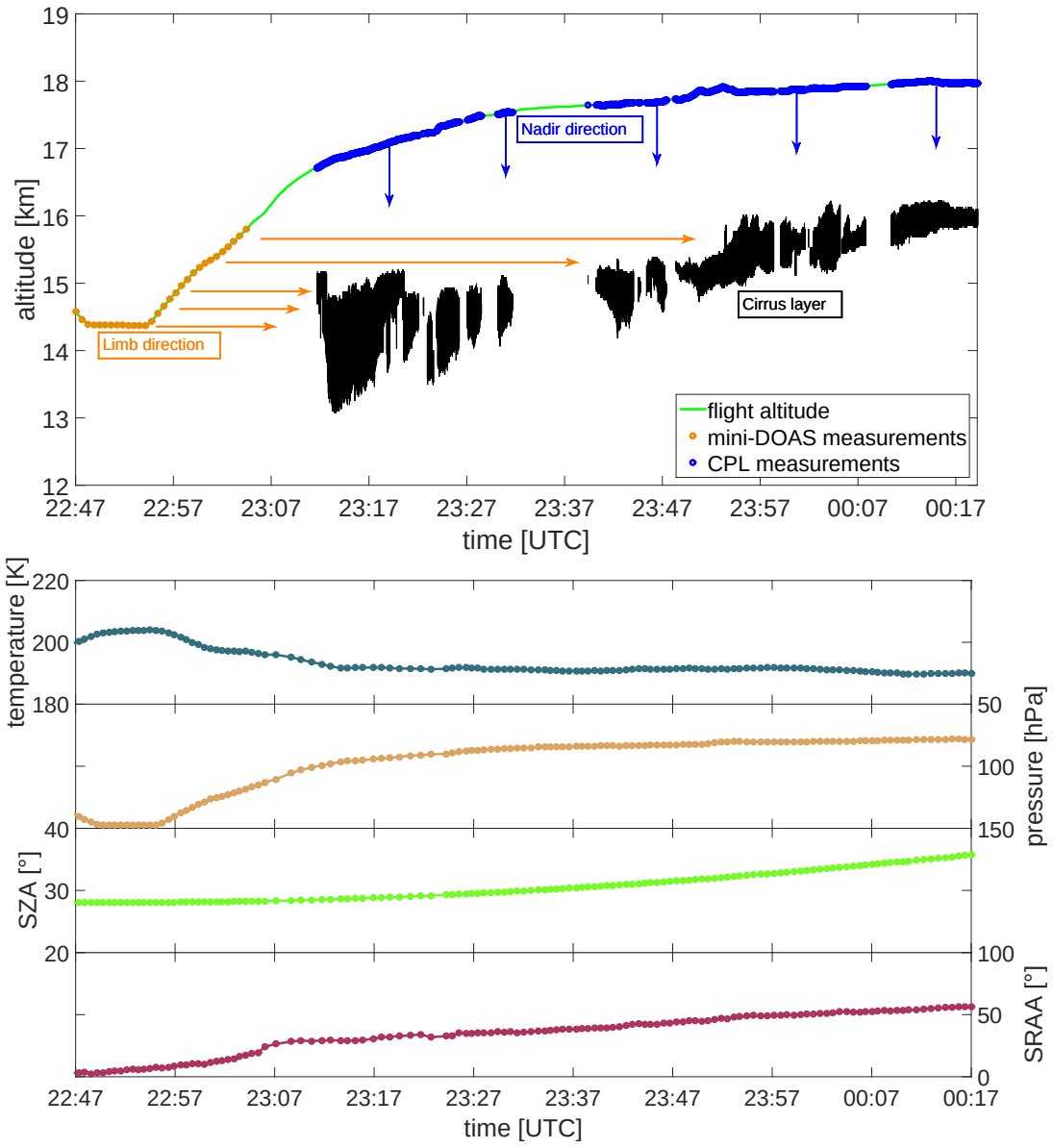

Figure 6.2: Upper panel: flight segment altitude for the mini-DOAS and CPL data detection (SF2-2013); the cirrus layers detected by CPL are plotted in black. Following: temperature, pressure, solar zenith angle and solar relative azimuth angle for the same flight segment.

DOAS telescopes were kept with a fixed elevation angle to $-0.5°$ (i.e. they were looking direct to the horizon). After spending few minutes at lower altitudes ($\sim 14.3\text{km}$), the GH started the ascent reaching the cruise altitude ($\sim 18\text{km}$). After the dive, the CPL data were collected almost continuously. In Fig.6.2 (upper panel) the data available from CPL concerning the position of the cirrus layer are plotted (in black). The next lower panels show the atmospheric conditions (in situ pressure and temperature) and the relevant geometric coordinates (SZA, $SRAA$). At those altitudes and temperatures only ice cirrus can be formed, therefore we decide to investigate the data of the mini-DOAS that were collected within the cirrus layer.

The ice particles described via Mie theory and treated as an ensemble provide very specific averaged optical properties for the cirrus characterization, particularly when the cirrus is modeled as a homogeneous slab. The asymmetry parameter g (see Eq.4.84) defines the *anisotropy* of the medium for the scattering component. The anisotropic scattering behavior can be used as *privileged observation direction* when looking straight to the horizon inside the cirrus (i.e. within the medium). In Fig.6.3 a sketch showing

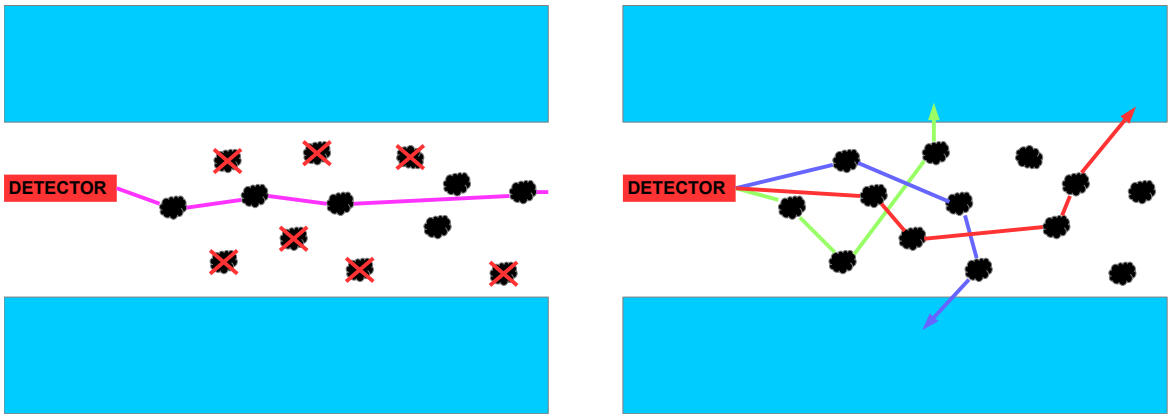

(a) Anisotropic scattering medium. (b) Isotropic scattering medium.

Figure 6.3: Sketch showing the different behaviors for the scattering directions in presence of an anisotropic scattering (a) or isotropic scattering (b) medium. Read the text for more details.

the different behaviors of scatters in an anisotropic scattering (a) (isotropic scattering (b)) medium is depicted. By inspecting Fig.4.26, it is clear that ice particles show a strong peak in the forward scattering direction. This behavior is represented by Fig.6.3 (a), where among all the particles forming the cloud only few of them are statistically favored to be reached by the scattered photons. This means that the modeled HG phase function characterizes a medium where the probability of scattering in the forward direction (i.e. to the next forward ice particle) is higher as compared to the probability of scattering in a randomly selected direction (i.e. ice particles marked with a red cross). This condition provides a privileged observation direction for the detector because, within the cloud, the photon path becomes increasingly long. If the medium scatters isotropically (see Fig.6.3 (b)), the trajectories can be randomly different and in this case the persistence of photons inside the medium is reduced as compared to the anisotropic scattering case [79].

In order to provide quantitative results to the discussion, some sensitivity studies are conducted. The main idea is that, having a privileged observation direction (in terms of the isotropic/anisotropic scattering), the increasing photon path length for the anisotropic scattering case provides a larger absorption as compared to the isotropic scattering medium.

In Fig.6.4 a first study is reported. It shows the sensitivity of the observations in limb direction when the detector is within or outside the cloud. When the detector is within the cloud (red line), the absorption of ice is amplified with respect to the cases when the detector is located above (blue line) or below (yellow line) the cloud. The limb viewing detection within the cloud renders the measurements more sensitive to the ice absorption and therefore the retrieval of the cirrus optical properties becomes easier as compared to the case of detector outside the cloud.

In Fig.6.5 the implications of the asymmetry parameter on the radiative transfer are

illustrated. The two simulations are run with same input parameters except for the asymmetry parameter. In one simulation the asymmetry parameter is evaluated via Mie theory (blue line), in the other simulation (red line) $g = 0$ for the whole wavelengths interval.

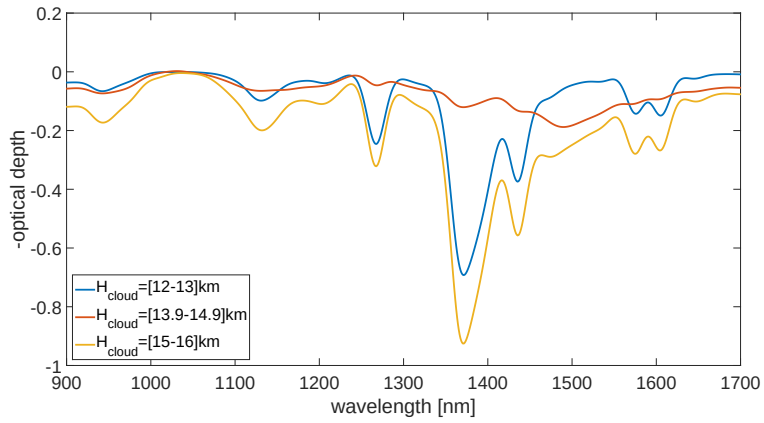

Figure 6.4: RTM simulations on the different cloud location with respect to the detector. The detector is placed at 14.4km looking at $-0.5°$ ($\mathrm{OD}_{\mathrm{cloud}} = 0.54$).

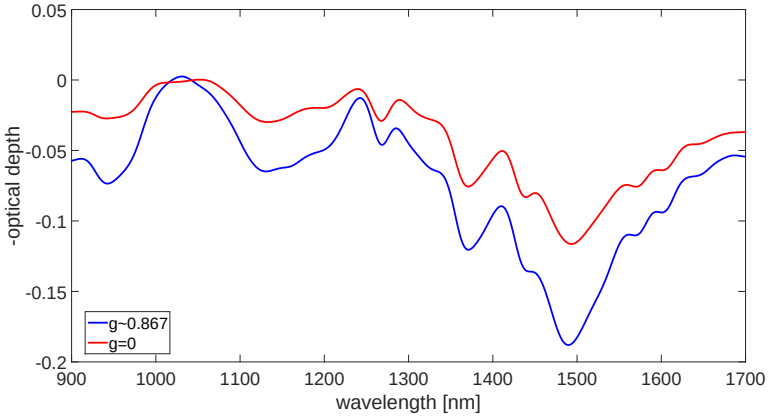

Figure 6.5: RTM simulations on the anisotropic/isotropic ($g = 0.867/g = 0$) HG phase function of ice particles. The detector is placed within the cirrus layer ($\mathrm{OD}_{\mathrm{cloud}} = 0.54$, $\mathrm{EA} = -0.5$).

In the first case the cirrus provides an example of anisotropic scattering medium (like Fig.6.3 (a)). In the second case the cirrus is characterized as an isotropic scattering medium (like Fig.6.3 (b)).

The absorption bands of molecules and ice particles are all deeper in the anisotropic scattering case, revealing that the photon light path becomes longer due to a strong forward peak in the angular diffusion direction.

Therefore, in order to strengthen the signal of ice particles in the near-IR spectrum, the

best detection configuration for the mini-DOAS instrument is achieved when

i. the detector is inside the cirrus;

ii. the detector is pointed towards the limb.

6.1.1 Cirrus Layer Configuration

Here, a basic method is reported that can be used when modeling the cirrus layer morphology as input to the RTM. The data collected by CPL are fundamental in order to remove the ambiguity in Eq.5.3, since for cloud optical depth retrievals it is necessary to have a good representation of the cloud position. In the context of the radiative transfer simulations, the position of the cloud bottom/top are the most important.
In Fig.6.2 (upper panel) the CPL data for the cirrus location are shown (in black).

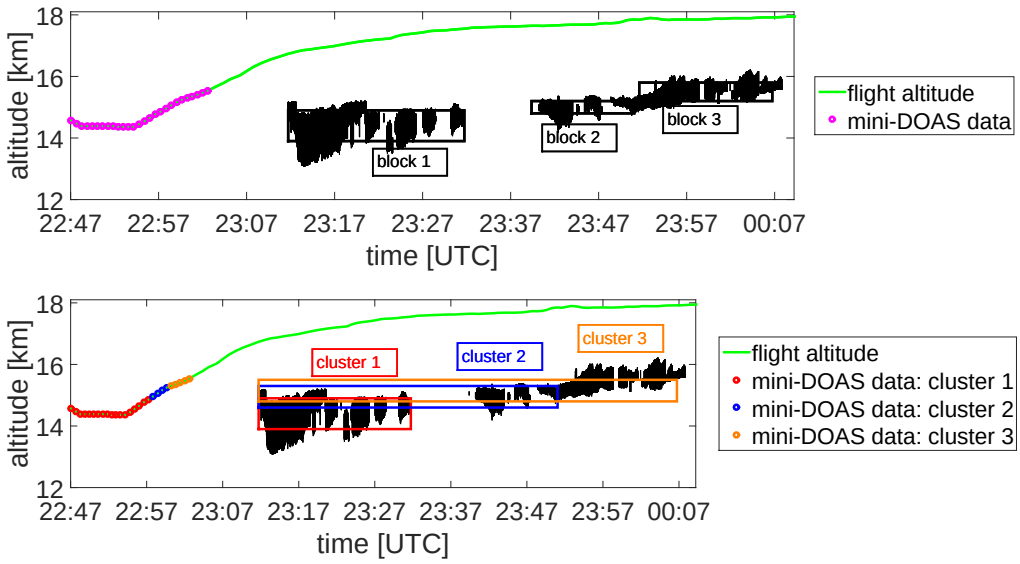

Figure 6.6: Clustering procedure. By making use of the CPL data about the cirrus position, it is possible to generate averaged blocks (black rectangles in the upper panel) representing the different cloud layers within the RTM simulations. In the lower panel the final clusters used in the RT modeling are shown (colored rectangles).

From these informations, it is possible to *cluster* the CPL data in order to have a basic layer (*block*) representation of the cirrus. The block structure facilitates the radiative transfer modeling.

This procedure is illustrated in Fig.6.6. At first (upper panel), the data from CPL are extracted and clustered in several blocks. The blocks are clustered according to the visibility of the mini-DOAS telescope (i.e. the line of sight). The blocks are time-averaged data of CPL concerning the cloud top, cloud bottom, and its central position. Following (lower panel), these blocks are used to create the final clusters.

For the first series of measured spectra (red points in the lower panel), the altitudes of detection are sensitive mostly to the first block (upper panel), hence the first cluster overlaps the first block.

When the aircraft is moving to higher altitudes, the mini-DOAS becomes more sensitive to the second block (upper panel) but physically the first block is also still present. Therefore, the second cluster (lower panel) reflects a cloud bottom/top which derives from the time-averaged data of block 1 and 2, but the central position of the layer is selected taking into account only block 2.

Following, the third cluster presents a cloud bottom/top which derives from the time-averaged data of the blocks 1, 2 and 3, but the central position takes into account only block 3.

These clusters define the different cloud altitude profiles to be used as inputs for the radiative transfer simulations. With this method it is possible to incorporate the different data collected by CPL and to shape them into a reasonable representation of the cloud morphology.

6.2 Inferred Cirrus ODs

In this section, the cloud optical depths are inferred using the oxygen absorption band method (see subsections 5.2.1 and 5.2.3). The results are discussed and compared with the findings of CPL and Hawkeye.

Fig.6.7 shows the inferred cloud optical depth (upper panel) and the extinction coefficient (lower panel). Two different cloud optical depths for each spectrum are retrieved from the mini-DOAS measurements. The red line corresponds to a lower limit, assuming only small particles in the oxygen absorption band analysis; the purple line represents the upper limit, assuming only large particles. The mini-DOAS inferred ODs and extinction coefficients are retrieved with a relative error of 3.2% (see subsection 5.2.2). These results are valid within the whole wavelengths interval $[900-1700]\mathrm{nm}$

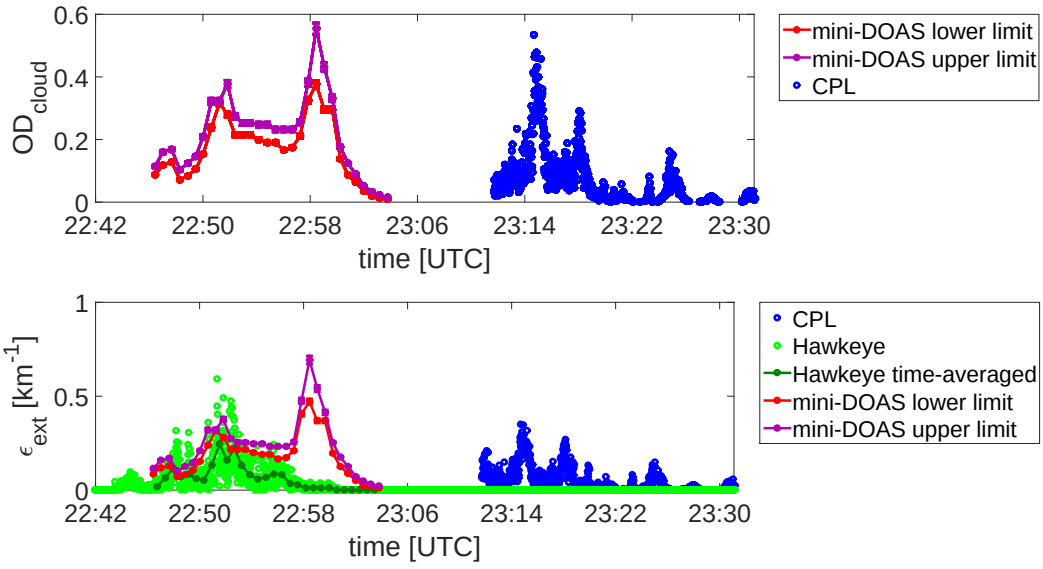

Figure 6.7: Inferred cirrus optical depth (upper panel) and extinction coefficient (lower panel). The upper limit (lower limit) refers to the analysis assuming only large particles (small particles).

since, within the error intervals, the extinction coefficient doesn't show a wavelength dependency (see Fig.5.7 middle panel). The CPL ODs and extinction coefficients are evaluated at $\lambda = 1064nm$.

It can be noted that the cirrus containing only large particles needs a higher extinction coefficient as compared to the cirrus cloud only containing small particles in order to obtain the same oxygen optical depth. In other terms, even if large particles can increase the photon light path within the cloud because they have larger asymmetry parameters as compared to small particles (see Fig.5.7 lower panel), they absorb more radiation in the ice absorption band (see Fig.5.7 upper panels) consequently the photon path length is reduced.

It should be noted that the mini-DOAS instrument provides measurements sensitive to the horizontal layer covered by the telescope field of view and only barely to other layers, while the CPL data are vertical soundings of the cloud deck. Accordingly the mini-DOAS observations have to be interpreted as horizontal integrations of the CPL data. Further, due to their different observation geometries the CPL and the mini-DOAS measurements are not collocated with respect to time.

In fact, by observing the behavior of the extinction coefficients (Fig.6.7 lower panel), the mini-DOAS results can be interpreted as a time-weighted sum of the CPL data. In other words, the mini-DOAS is capable to detect in one spectrum the contributions deriving from different vertical sectors of the cirrus. The described method thus provides complementary information on the cirrus optical properties to the in situ measurements performed by the different instruments.

In addition to CPL, the Hawkeye data also allow to infer cloud extinction coefficients. They are reported in Fig.6.7 (lower panel, all data in light green, time-averaged in dark green). The Hawkeye extinction coefficients are calculated from the measured densities and particle dimensions. For the optical model they assume spheres and the optical

properties are evaluated via Mie theory (the typical wavelength for these calculations is $1\mu m$). The comparison of the mini-DOAS inferred extinction coefficients with the Hawkeye findings shows a good agreement for all observations until 22:58 UTC. Afterwards, in the time interval 22:58 - 23:02 UTC, the GH moves to higher altitudes and then outside the cirrus layer. Here, the data reported by Hawkeye are below the detection limit of the instrument, while the mini-DOAS reports a peak in the extinction coefficients. Inspecting the CPL data, it is arguable that the mini-DOAS becomes sensitive to the cirrus layers detected later by CPL. This is evident since the mini-DOAS can inspect horizontally several vertical sections of the cloud, providing a time-averaged overview of the cirrus layer, i.e. quasi in situ detection of ice particles optical properties. The good agreement found between the different instruments validate the model and the method developed for the data analysis of the near-IR differential optical absorption spectroscopy measurements. Moreover, the good agreement demonstrates the potential of near-IR spectroscopic limb observations for the retrieval of cirrus optical properties. Further, it should be noted that due to lack in limb observations, a full-fit for near-IR measurements has never attempted before. Furthermore, the DOAS technique which makes use of instrumentation at medium spectral resolution, turns out to be a powerful tool of investigation since it is able to detect in the near-IR subvisible thin cirrus clouds in remote sensing when well oriented within the cirrus. These subtile objects are very difficult to detect even from precise instruments such as satellites, and then the information concerning their microphysical characteristics are still very uncertain.

The main limitation in the analysis is the cloud morphology. In fact, if the cloud bottom/top is not known with a certain degree of confidence, the retrieval of cloud optical depth cannot be executed with good accuracy.

6.3 Inferred IWCs and IWPs

Within this section the results on the inferred ice water contents and ice water paths are reported. As explained in subsection 5.2.4 , the ice absorption band at 1493.5nm caused by ice particles can be used to investigate the mixing ratio of small to large particles. Starting from the two boundary limits for the inferred cloud ODs (see Fig.6.7), the simultaneous upper and lower limit for the ice water contents and ice water paths ($IWC_{<50}$, $IWC_{>50}$, IWC_T, IWP) can be inferred. The results for the ice water contents are shown in Fig.6.8. The results show that the major contribution to the total IWC_T is due to the large particles. Concerning the description of the ensemble [81], the parameterization of the particle size distributions in terms of ice water contents is a very important point. In fact, how the optical properties of single particles are contributing

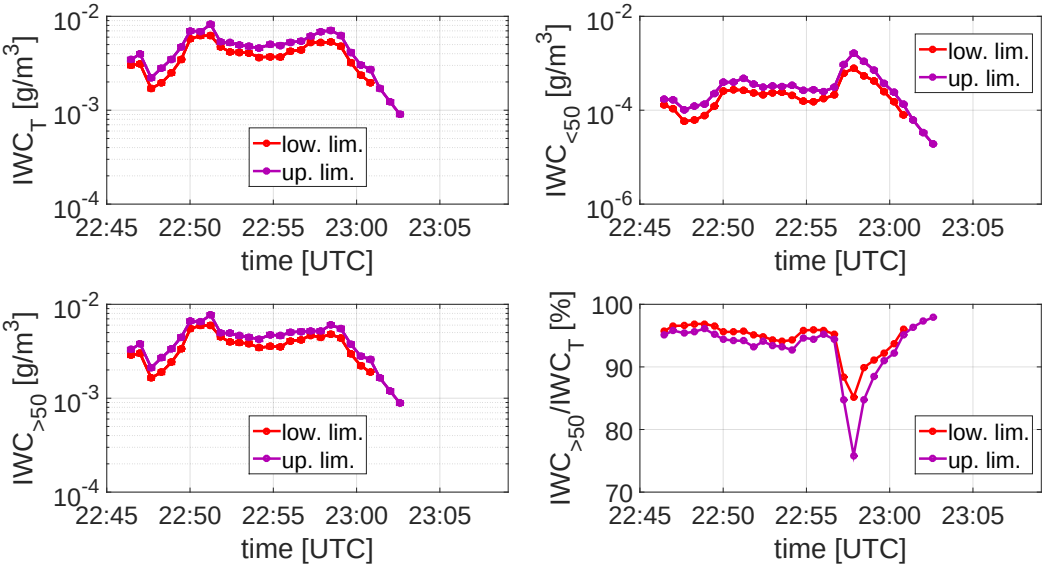

Figure 6.8: Total ice water content (top left), ice water content for small particles (top right), ice water content for large particles (bottom left) and mixing ratio for large particles (bottom right).

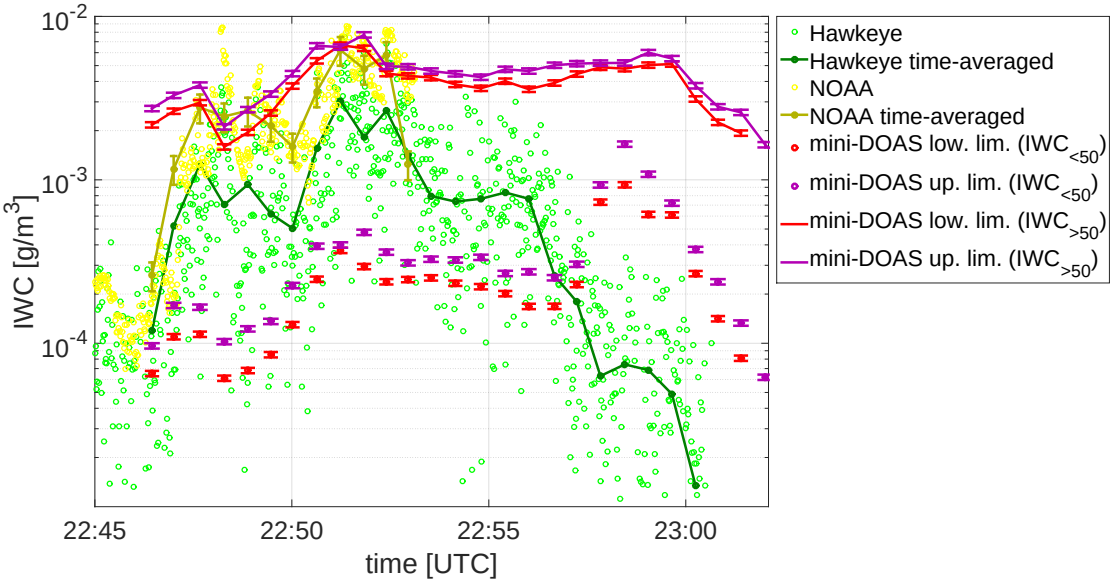

Figure 6.9: Inferred ice water contents for the mini-DOAS, Hawkeye and NOAA Water observations.

to the optical properties of the whole ensemble, and how they are affected by the ice water content largely characterizes the cirrus. In this respect, the ice absorption band method can reveal whether the assumed particle size distributions are appropriate for ice cirrus analysis or not.

As a first validation, the mini-DOAS IWCs are compared to the in situ Hawkeye and NOAA Water measured IWCs. Hawkeye (see section 3.3) provides in situ measurements of ice water contents, number concentrations and particle size distributions (in the radii interval $[0-25]\mu m$), while NOAA Water (see section 3.4) provides in situ measurements of the total water concentration (all three H_2O phases) and from these data they evaluate the IWC. The comparison on the ice water contents is shown in Fig.6.9. The results lead to several conclusions.

First, the measured IWCs of Hawkeye are well reproduced by the mini-DOAS measurements. Hawkeye measures two peaks in the IWCs (around 22:47 UTC and 22:52

UTC) and these peaks are also detected by the mini-DOAS, though somewhat flatter and with overall larger IWCs. Further, for the measurements around 22:58 UTC, when the GH leaves the cirrus cloud and in consequence Hawkeye detects very low IWCs concentrations, the mini-DOAS detects an increment of the IWCs most likely because it becomes sensitive to the next cloud layers, as detected by CPL (see Fig.6.7).

Second, the total ice water content inferred by the mini-DOAS (see top left panel of Fig.6.8) is mainly made up of large particles ($IWC_{>50}$). The large particles contribute more than 90% to the total IWC_T (see bottom right panel of Fig.6.8). In this respect, the mini-DOAS overestimates the Hawkeye data. In fact, the mini-DOAS $IWC_{>50}$ marks an upper limit for the Hawkeye IWCs (see Fig.6.9) but it must be remembered that Hawkeye measures particles with sizes ranging in the radii interval $[0-25]\mu m$, therefore they should mostly reflect the mini-DOAS results for $IWC_{<50}$.

The NOAA Water instrument infers IWCs much closer to the mini-DOAS results as compared to the Hawkeye IWCs. Like the mini-DOAS, the NOAA Water instrument is sensitive to the whole ensemble of ice particles and not only to small crystals like the Hawkeye fast cloud droplet probe. In this respect, the NOAA Water instrument provides a relevant validation for the mini-DOAS inferred results and the methods proposed in the present work. The NOAA Water inferred IWCs are available only for the first part of the investigated segment because then a failure occurred in the inlet tubing and the subsequent IWCs cannot be calculated.

As shown in section 4.6, the particle sizes and the relative optical properties are weighted according to the particle size distributions employed in the mini-DOAS retrievals and they can be parameterized in terms of the total ice water content (IWC_T) as suggested by [81] (see Eq.4.56 and Fig.4.22). Since the *McFarquhar and Heymsfield* parameterization is not considered in the present retrieval, the mini-DOAS results provide new parameterizations in terms of IWC_T. Both parameterizations are shown in Fig.6.10

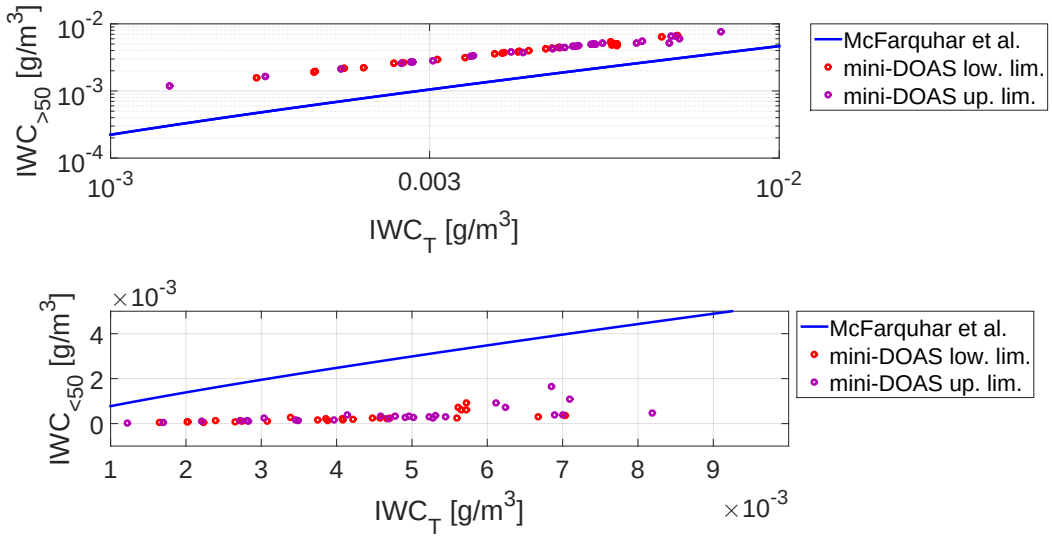

Figure 6.10: Ice water content parameterizations. In the upper panel (lower panel), the ice water content for large particles (small particles) as a function of the total ice water content is shown. $IWC_T = IWC_{<50} + IWC_{>50}$.

and compared with the *McFarquhar and Heymsfield* parameterization. The results show that the parameterization proposed by [81] is not able to explain the ice absorption band detected by the mini-DOAS. In fact, if the *McFarquhar and Heymsfield* parametrization of the particle distributions was correct (Eq.4.56), then the analysis of the ice absorption at 1493.5nm should indicate a larger ice amount than the retrieved ice amount for small particles (see Fig.6.10, lower panel). Vice versa, the parameterization provides lower amounts of $IWC_{>50}$ as a function of the IWC_T with respect to the retrieved larger particles. Since the collected spectra reveal deeper optical depths, the *McFarquhar and Heymsfield* parameterization cannot be used for the detected cirrus. Deeper absorption optical depths for ice particles mean that primarily the contribution of large particles is not well accounted for in [81]. In fact, as shown in Fig.5.7 (upper panels), the single scattering albedo of large particles provide stronger absorption with

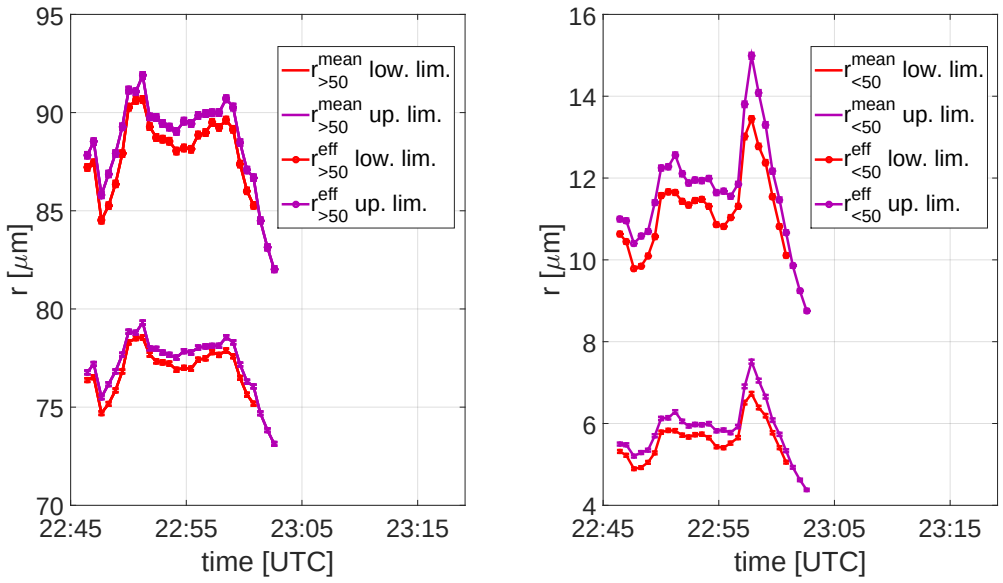

Figure 6.11: In the left panel, the mean radius (see Eq.4.57) and the effective radius (see Eq.4.59) for large particles are shown. On the right panel the same results for small particles are reported.

respect to small particles.

Further, the mini-DOAS inferred ice water contents are sensitive to the mean radius (or to the effective radius) of the total ensemble for both small and large particles (see Fig.4.24). Therefore, it is possible to retrieve the particle sizes once the IWCs are known. The inferred radii are shown in Fig.6.11, they indicate that the large particles (mean radius of about $[73-78]\mu m$) primarily contribute to the total ice water content (see Fig.6.11 left panel).

Particles with such dimensions ($r \sim 75\mu m$, see left panel of Fig.6.11) cannot be frequent in the TTL since the low temperatures prefer the formation of very small aggregates [54, 57, 109]. In order to justify the presence of large particles in the TTL, the in situ water vapour mixing ratio is inspected and the results are shown in Fig.6.12. The figure shows the in situ water vapour mixing ratio detected by UCATS and DLH, and the

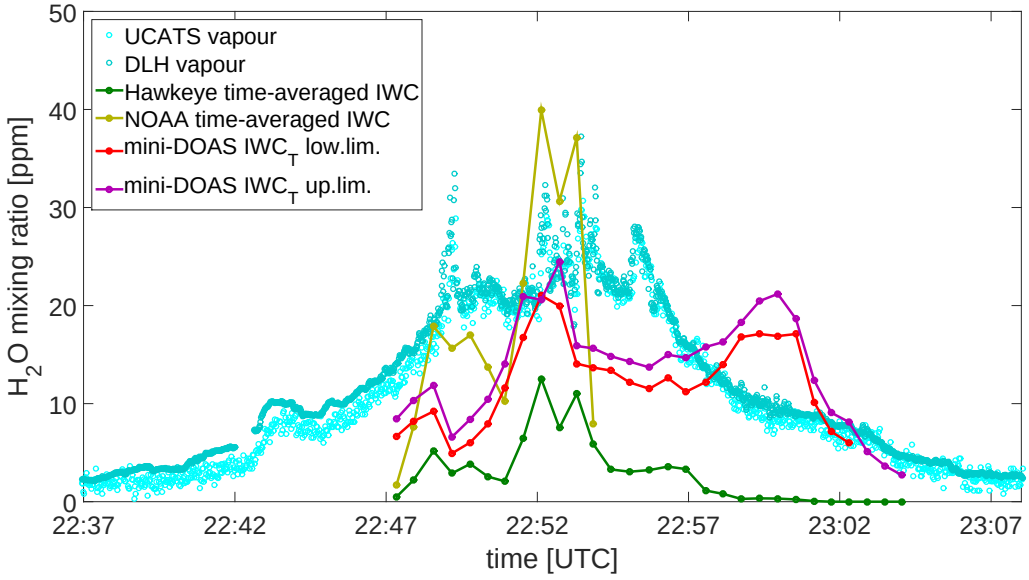

Figure 6.12: Mixing ratios for water vapour (UCATS and DLH instruments) and ice water contents (Hawkeye, NOAA Water and mini-DOAS instruments).

IWCs mixing ratio for Hawkeye, NOAA Water and the mini-DOAS. The comparison provides evidence that sufficient amount of water is available to form large particles. Furthermore, the NOAA Water inferred IWCs mixing ratio (see Fig.6.12) are larger compared to the mini-DOAS and Hawkeye results. The Hawkeye measurements are sensitive to the small particles (i.e. $r < 50\mu m$), while the mini-DOAS and the NOAA water measure the overall contribution, i.e. small and large particles. Since the mini-DOAS and the NOAA Water instruments show a very good agreement when inspecting the inferred ice water mass (see Fig.6.9) then a difference in the inferred IWCs mixing ratio derives from the particle sizes, i.e. the PSDs adopted. In other terms, the NOAA Water inferred IWCs mixing ratio can be obtained assuming the same ice mass inferred by the mini-DOAS but smaller particle sizes than the particle sizes retrieved by the mini-DOAS.

In order to provide evidences of the presence of large particles ($r > 50\mu m$) in the

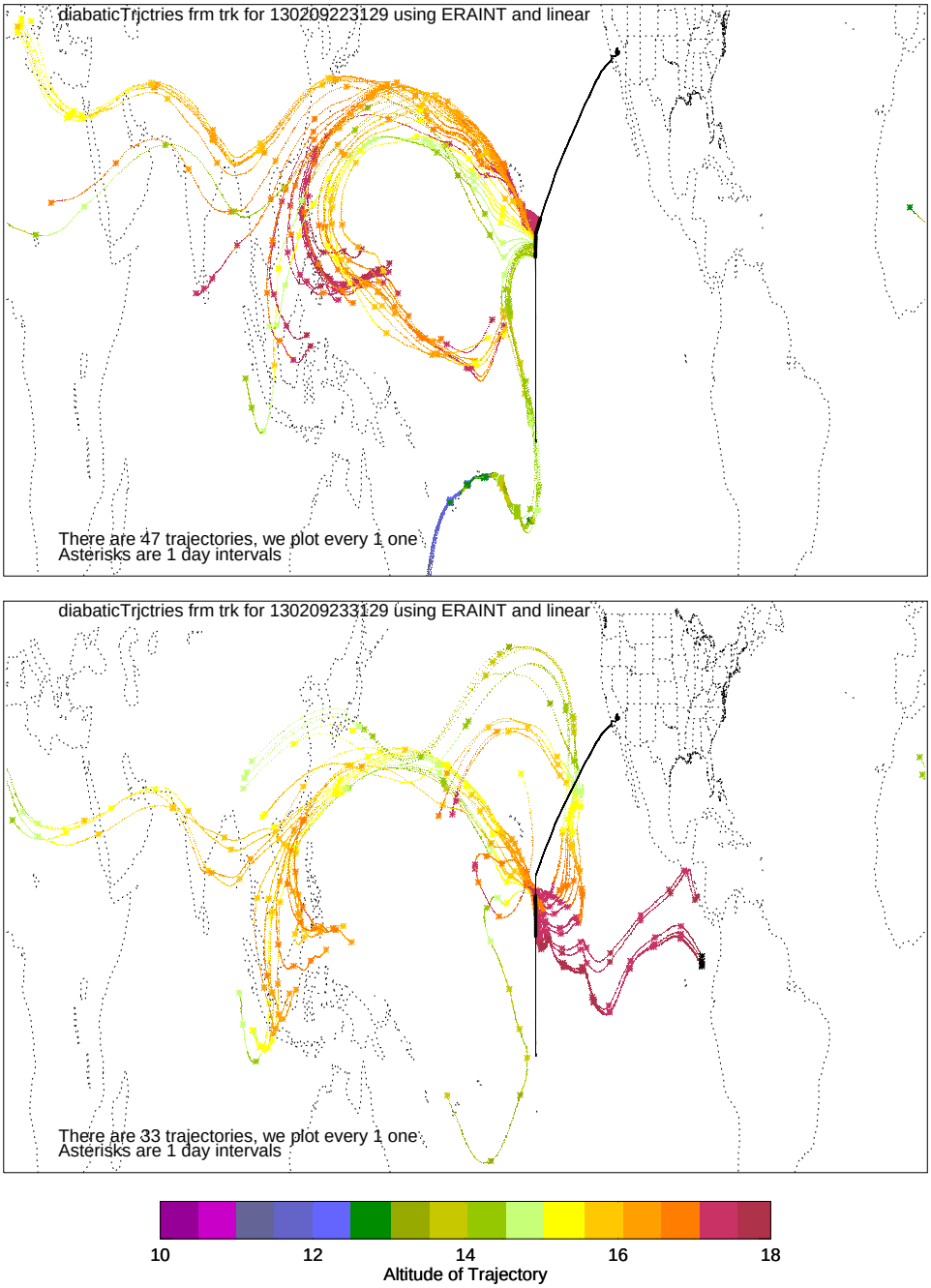

Figure 6.13: Air mass back-trajectories for the flight segments 22:31-23:31 UTC (upper panel) and 23:31-00:31 UTC (lower panel) of SF2-2013. The black line shows the the whole flight trajectory. The color bar indicates the altitude of trajectories in km.

TTL, the air mass back-trajectories[1] along the flight segment can be investigated (see Fig.6.13). Fig.6.13 shows 10-day diabatic back-trajectories from selected points along the flight track. The calculations use 6-hourly ERA-Interim[2] analyses (0.75 by 0.75 degree resolution) along with heating rates depending on longitude, latitude, and altitude (constant in time, based on CALIPSO / CLOUDSAT data [137]). The vertical resolution of these analysis is approximately 1km near the TTL. The upper panel of Fig.6.13 shows the back-trajectories for the investigated dive (22:31-23:31 UTC). The air mass trajectories are around 14km (green colored) on the flight track. When moving back in time (1 asterisk corresponds to 1 day), the air masses originate from regions just below the flight track (they become olive green), suggesting that an injection of humid air masses containing large particles from a mesoscale system into the TTL was possible. In the lower panel of Fig.6.13 the back-trajectories of the subsequent flight segment is reported (23.31-00:31 UTC). In this case, the GH rose to higher altitudes. In fact, the air masses on the flight track derive from 16 to 18km altitudes. In the very first section, the air masses originate from the regions around the flight altitude with very few injections from lower layers. These air masses and those following represent the cloud layers detected by the mini-DOAS when the GH moved out of the cloud (after 22:58 UTC). For the air masses (after 22:58 UTC) later probed, the mini-DOAS results show a different IWCs mixing ratio (see Fig.6.8 bottom right panel). In fact, a larger amount of small particles is inferred. This can be explained as following. During this section, the mini-DOAS is sensitive to the cloud layer detected until 22:58 UTC but then it becomes sensitive also to the subsequent cloud layers (see upper panel of Fig.6.2 for the configurations of detection) which were formed most likely by in-situ condensation at lower temperatures.

The ERA-Interim analyses on the air masses back-trajectories (22:31-23:31 UTC) high-

[1] https://bocachica.arc.nasa.gov/ATTREX_2013/back_traj/back_traj.html
[2] http://www.ecmwf.int/en/research/climate-reanalysis/era-interim

lights that an injection of humid air masses from the middle and upper troposphere into the flight track is very likely, supporting the idea of an upward lift of large particles from the bottom layers which is also confirmed by the high water vapour mixing ratio levels measured in situ (see Fig.6.12).

In fact, when an event of enhanced ice water content is observed in the tropics, this is often related to recent strong convection activity. This was also reported by [110], they analyzed the IWCs data of several experiments (executed in the tropics, midlatitudes and Arctic regions), focusing on the temperature dependence of the ice water content. Their results for the tropical regions are reported in Fig.6.14, where the inferred IWCs

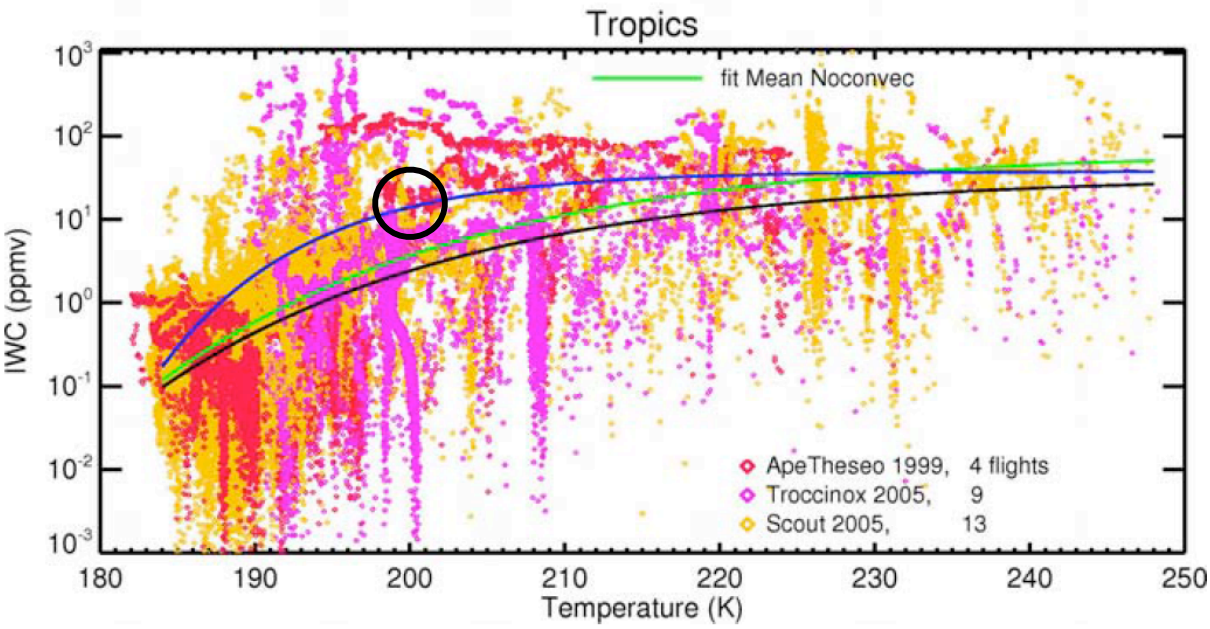

Figure 6.14: Temperature dependence of IWCs in tropical cirrus. Black/blue/green lines are fits through the median/mean/mean (without convective events) values (adapted from [110]). The black circle indicates the inferred IWCs results for the mini-DOAS.

for the mini-DOAS observations are also circled. Fig.6.14 shows that the mini-DOAS (and NOAA Water) inferred IWCs (black circle) stand on the mean line fit (blue) which accounts for convective events. This comparison confirms that the air mass probed by the mini-DOAS was probably impacted by convection. Therefore one can classify the cloud of being of moist origin.

Regarding the possibility of growing in situ large particles via sedimentation processes, *Jensen et al.* [56] demonstrate that when the water vapour concentration is about $2-2.5\mathrm{ppm}v$ then the formation of ice crystals with diameters of ca. $100\mu\mathrm{m}$ can occur. The mini-DOAS results show even higher diameters for the large particles (up to $150-160\mu\mathrm{m}$) but, at the same time, large concentration for water vapour is also measured. If these massive particles can formed in situ, they are subjected to rapid sedimentation and they have high terminal velocities because they carry big amount of mass within a low density environment [40]. For particles diameters of about $100\mu\mathrm{m}$ the terminal velocities are larger than $10\mathrm{cm}/\mathrm{s}$ [40, 87]. Therefore, these particles rapidly settle, except in rapid updrafts. Therefore the detection of large particles by the mini-DOAS and in addition the in situ detection of high concentration of water vapour (UCATS and DLH instruments) provide further evidence that particles of a convective outflow event were observed during the flight segment 22:45-23:00 UTC of SF2-2013. This conclusion is also supported by the analysis on the back-trajectories as well as by the *Schiller et al.* [110] data (see Fig.6.14).

Of particular interest in general circulation model (GCM) is the capability of correlating the ice water content of clouds to the diameters of particles forming them. These correlations simplify the calculations for the radiative net budget. *Liou et al.* [73] estimate that the tropical cirrus containing IWCs in the range of $[10^{-6}-10]\mathrm{g}/\mathrm{m}^3$ can be parameterized as a function of the ice particles effective diameter (Fig.6.15). The mini-DOAS inferred IWCs and effective diameters also provide a relation and the relative results are

shown in Fig.6.16, in green the best fit from *Liou et al.* [73] is also reported. For small particles there is a very good agreement with the *Liou et al.* parameterization. The mini-DOAS results express the same relation for IWC and D_{eff}, however with an offset of ca. 5µm. The *Liou et al.* inferred best fit has to cover a very large spread of data. In fact, in the tropics not only in situ ice particles can be formed but very likely the presence of large particles transported in the TTL from the convective outflows may impact drastically the IWC. In this respect the prediction of *Liou et al.* is rather uncertain and they provide relative errors spanning from 5% to 40%. Thus, the mini-DOAS results for small particles are consistent with the [73] parameteri-

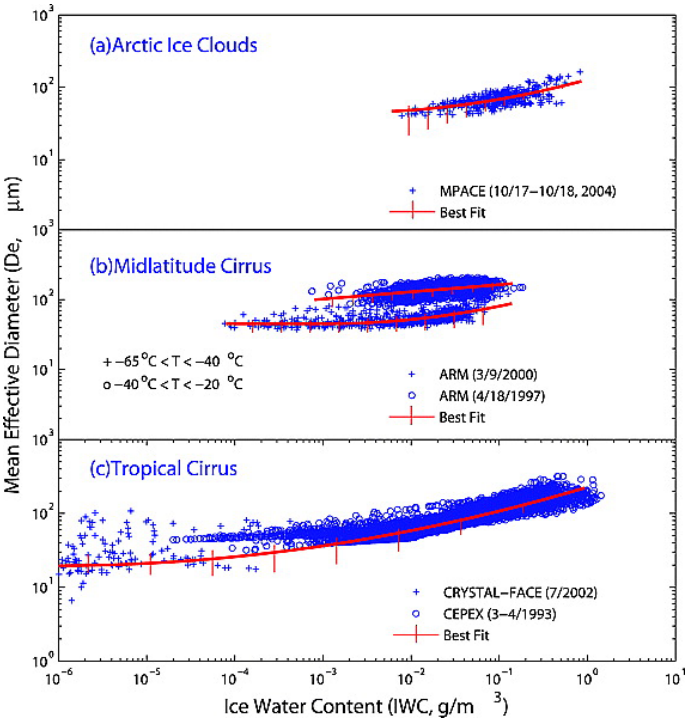

Figure 6.15: Mean correlation curves with uncertainties associated with small ice crystal concentration for IWC and D_{eff} for (a) Arctic regions, (b) midlatitude, and (c) the tropics. Adapted from [73].

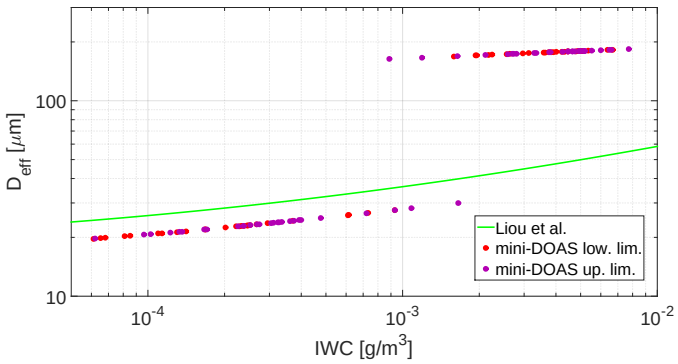

Figure 6.16: Inferred effective diameter as a function of IWC for the mini-DOAS. Green curve from [73], see Fig.6.15 (c) panel (red curve).

zation, while the large particles show a different relation of D_{eff} as a function of IWC. *Liou et al.* have parameterized the data using the same particle size distributions used in the mini-DOAS retrievals, but the analyzed data in [73] are more sensitive to small particles with respect to large particles. In fact, they mostly involved only the gamma distribution for the fitting procedure. In the ice absorption band ($1493.5\mathrm{nm}$), the mini-DOAS instrument seems to be sensitive to both small and large particles. For large particles, the mini-DOAS inferred results point to a deficit in characterizing differently the relation between particle sizes and ice water contents for cirrus formed in convective outflows of the TTL. In this respect a unique parameterization cannot be used for general circulation model calculations of radiative net budget. Moreover, *Liou et al.* do not account for temperature dependence (they do only for midlatitudes cirrus), while [110] (see Fig.6.14) clearly illustrate that such a correlation for tropical cirrus exists. Noteworthy, the relation of IWC with temperature is largely dependent on the genesis of the individual cirrus. Therefore, the mini-DOAS results support the parameterization for small particles but, on the other hand reveal that a unique relation does not exist when large particles are also present.

The quality of the present method developed to retrieve IWCs depends mostly on the assumed particle size distributions parameterizations and on how the different contributions of small and large particles are weighted. Since the Hawkeye (FCDP) instrument measured ice particles in the radii interval $[0-25]\mu\mathrm{m}$, it is possible to extract the measured PSDs and compare them with the gamma distribution employed for the mini-DOAS retrievals. The results are shown in Fig.6.17 for three different ice water contents. The Hawkeye PSDs are calculated only for the flight segment of interest when the mini-DOAS measurements are available, i.e. 22:45-23:00 UTC. The selection in terms of IWC is done using the relative error of the retrieved mini-DOAS IWCs (3.8%). Consequently the PSDs are chosen according to the IWCs interval $IWC \times (1 \pm 0.038)$.

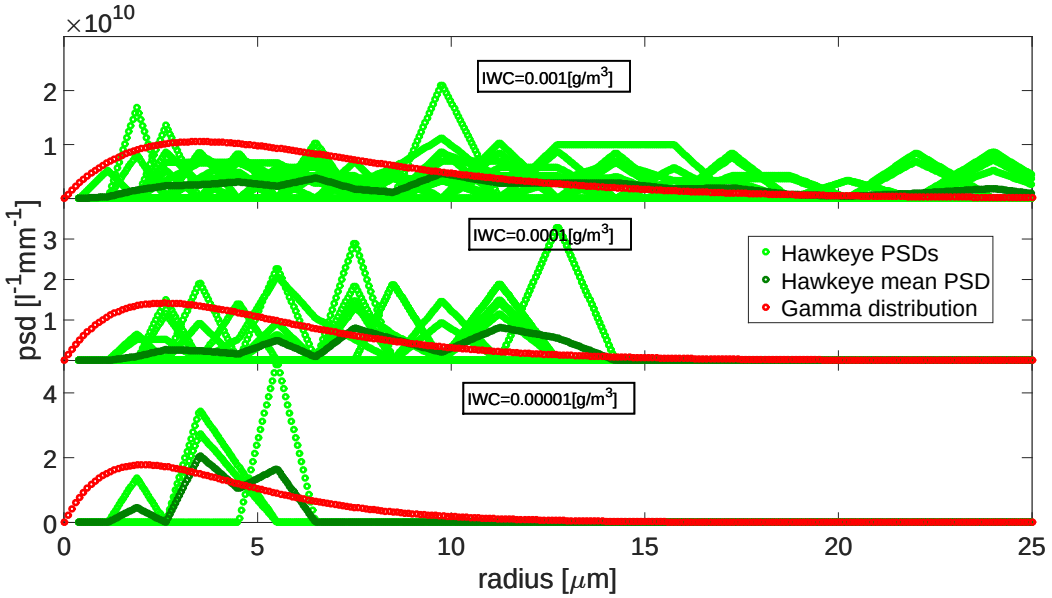

Figure 6.17: Particle size distributions inferred by Hawkeye and gamma particle size distribution from [81], involved in the mini-DOAS analysis. The Hawkeye data derive from the flight segment SF2-2013 (22:45-23:00 UTC).

Finally an averaged PSD from the Hawkeye data is also plotted for each IWC. Fig.6.17 shows that there is a good agreement for particle radii larger than $10\mu m$ except for the $IWC = 10^{-4}[g/m^3]$ where the gamma distribution underestimates the Hawkeye averaged PSD. For the particle radii interval $(0-10)\mu m$, the Hawkeye PSDs and the gamma distribution show a different behavior, in particular for the $IWC = 10^{-3}[g/m^3]$ and $IWC = 10^{-4}[g/m^3]$. This difference may explain the difference between the IWCs measured by Hawkeye and the inferred $IWC_{<50}$ from the mini-DOAS (see Fig.6.9). Moreover, the contribution of larger particles, accounted for by assuming a lognormal distribution in the mini-DOAS retrievals, is not measured in the Hawkeye spectrometer probe and therefore a direct comparison (1 to 1) is not really possible.

Inferred IWPs

Finally, the retrieved ice water paths are reported for the selected flight segment. The results are shown in Fig.6.18 (left panel). The lower limit (in red) is obtained from the analysis performed on the oxygen absorption band (1.27µm) assuming only small particles (see Fig.6.7). The upper limit (in purple) is retrieved assuming only large particles. As suggested before, for the two cases, the total extinction acts in a slightly different way. The optical properties show that large particles absorb more compared to small particles. Therefore, even if they scatter more into the forward direction (see Fig.5.7, lower panel), the light path within the cloud is shortened. This can be seen in Fig.6.18 (left panel). The upper limit (purple line), which defines the upper bound in the cloud optical depth retrieval (oxygen absorption band analysis), provides for the

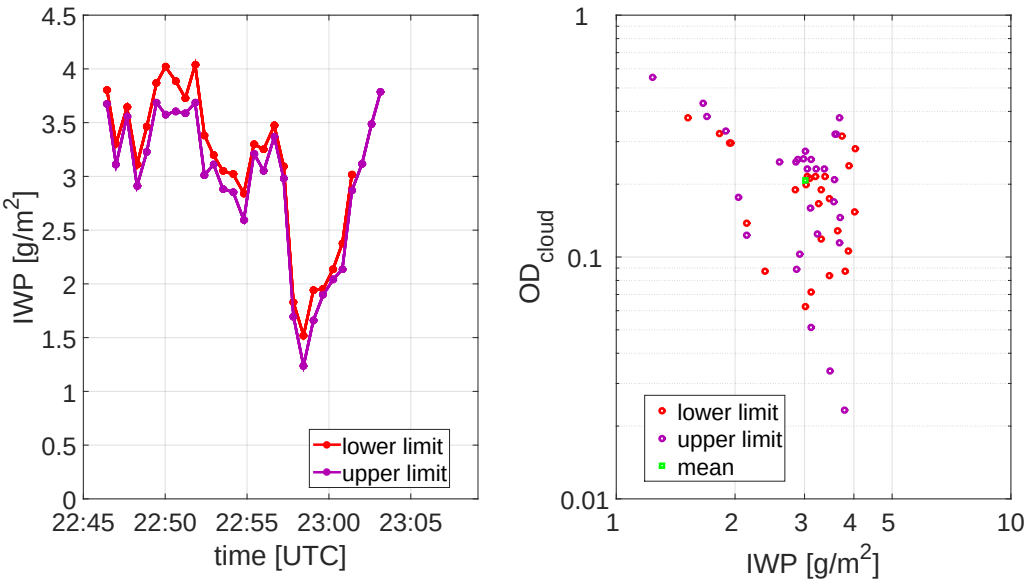

Figure 6.18: Inferred ice water paths from the mini-DOAS for the studied flight segment of SF2-2013 (left panel). Correlations between inferred cloud extinctions and inferred IWPs (right panel), in green the mean is reported.

IWP retrieval a lower limit since extinction coefficients and ice water paths are inversely proportional (see Eq.5.18).

For parameterizations in general circulation models is necessary to find correlations between the different parameters involved in the calculations for the radiative net budget. Thus, in Fig.6.18 (right panel) the inferred cloud ODs as a function of the inferred IWPs are shown. Like for cloud retrievals in the visible wavelengths interval [41, 22, 126], the mini-DOAS inferred IWPs provide new insights on the near-IR wavelengths interval at low cloud optical depths ($0.02 < \mathrm{OD}_{\mathrm{cloud}} < 0.6$). In fact, the mini-DOAS observations may offer a direct comparison to simulation of the near-IR radiative transfer of GCMs. The mean value of the ODs as a function of IWPs (see Fig.6.18 green dot) suggests that the parameterization found by [22] may also be used for the near-IR, but since for the few observations the results are scattered, a correlation can hardly be distinguished.

Daniel et al. [16] provide measurements from spectrally resolved near-IR $[865 - 1065]\mathrm{nm}$ observations of all three phases of water and total path-integrated column abundances of vapour, liquid and ice water. With respect to their work, the mini-DOAS results provide the IWPs by using one absorption band of ice ($1493.5\mathrm{nm}$) for the retrieval instead of a non-absorbing wavelengths interval. Moreover, the geometry of observations are different with respect to *Daniel et al.* [16], since the mini-DOAS collect spectra in limb within the cloud, while *Daniel et al.* [16] mostly analyze ground-based observations and they provide more information about the liquid water paths since low-altitude clouds were probed. In a later study, *Daniel et al.* [17] extend the retrieval in the near-IR wavelengths interval to $[900 - 1700]\mu\mathrm{m}$. They use ground-based zenith observations to retrieve water in the three phases and the relative photon paths, even in this case they mostly report on liquid water.

In this respect, the mini-DOAS observations from the GH are more focused on ice particles forming cirrus in the TTL. As demonstrated on the present thesis, air-borne limb

measurements in the near-IR may provide novel and complementary information on cloud OD and IWC of the climate relevant TTL cirrus.

Conclusions and Outlook

In the present study a new method for the retrieval of the optical properties of ice particles forming cirrus clouds is explored and discussed.

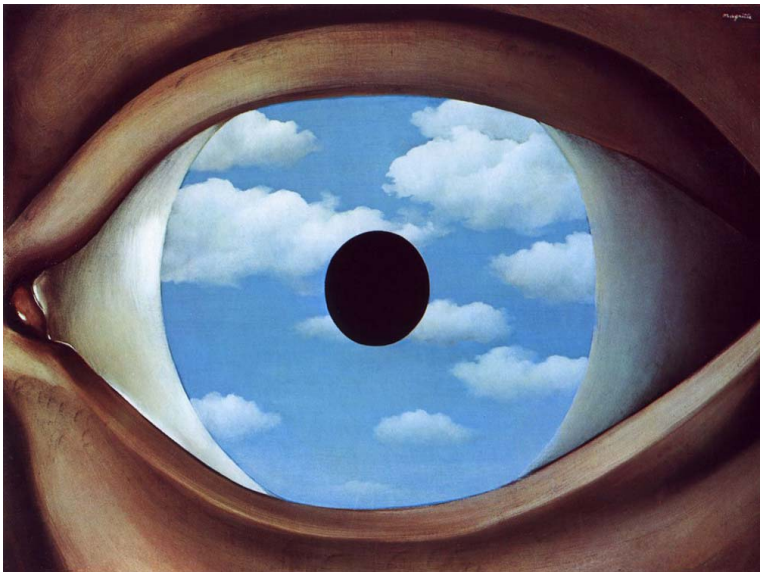

Figure 6.19: "*Le Faux Miroir*", R. Magritte (1928).

The data relevant for this study were collected with the mini-DOAS instrument (Differential Optical Absorption Spectroscopy [98], $S/N \sim 300$) on board the NASA Global Hawk (GH), during the ATTREX (Airborne Tropical TRopopause Experiment) campaigns [59].

The theoretical model used to explain the near-IR spectra consists of

i. a Monte Carlo radiative transfer model (McArtim [20]) for the simulations of the spectral radiance (1% relative error) in the near-IR interval $[900 - 1700]\mathrm{nm}$;

ii. a Mie scattering code (double-precision Lorentz-Mie scattering code [85, 86, 84]) to calculate the optical properties of ice particles ($\sim 10^{-4} - 10^{-5}$ relative error). Here, the ice particles are treated as spheres of equivalent mass by making use of two different particle size distributions, the gamma distribution for small particles ($r < 50\mu m$) and the lognormal distribution for larger particles ($r > 50\mu m$). The particle size distributions are parameterized as functions of the ice water contents (IWCs) [81].

The method developed for the near-IR spectral retrieval is divided in two steps.

First, the modeled oxygen absorption band ($^1\Delta_g \leftarrow ^3\Sigma_g^-$ at $1.27\mu m$) is fitted to the measurements in order to retrieve the cloud optical depths (ODs). The procedure is applied two times, first considering only small particles and then considering only big particles. These two procedures lead to an upper and a lower limit for the expected ODs and extinction coefficients. The sensitivity studies suggest that the best detection is reached when the detector is placed within the cloud and is pointed to the horizon. In this case the threshold for the inferred cloud ODs is 0.01.
The method is applied to a flight segment of SF2-2013 where the Global Hawk probed the tropical tropopause layer (TTL) in the eastern Pacific during the winter season and several TTL cirrus layers were encountered. The mini-DOAS inferred results are compared with the CPL and Hawkeye in situ measurements and the best agreement is obtained with Hawkeye. A direct in situ comparison with CPL is not possible since the CPL data are only available when the GH doesn't fly within a cirrus and the mini-DOAS data analyzed here refer to a dive flight segment within a cirrus. However, the cloud bottom/top informations provided by CPL are worthwhile for the general understanding of the mini-DOAS data since these informations are required as input to the radiative transfer model. The relative errors for the inferred cloud ODs and extinction

coefficients are assessed to 3.2%. The major limitation of the oxygen absorption band method is the characterization of the cloud morphology. In other terms, the method can be used when the cloud top/bottom are known with a certain degree of confidence.

The second step of the retrieval consists on a fitting procedure executed on the ice absorption band ($\sim 1.49\mu m$). From this analysis it is possible to distinguish between the contributions of small and large particles, finding the relative mixing ratio. The sensitivity studies show that, for the same extinction, the large particles absorb more radiation. Therefore, once the cloud optical depth is known, the particle mixing ratio can be inferred. Since the optical properties are linked to the ice water contents via the particle size distributions, the measured ice absorption determines the ice water content of small and large particles. In the retrieval the threshold for the inferred total ice water content is reached when the cloud optical depth is ~ 0.06 and it is about $10^{-3}[g/m^3]$.
The inferred IWCs are compared with the in situ Hawkeye and NOAA Water measurements. A reasonable agreement is found between the temporal behavior of the mini-DOAS and Hawkeye measurements. A direct comparison of IWCs with Hawkeye is not possible because Hawkeye measures only particles with radii up to $25\mu m$, while the theoretical model for the mini-DOAS considers particles with radii up to $200\mu m$. On the other hand, the comparison of IWCs with the NOAA Water instrument shows a very good agreement and since the NOAA Water instrument, like the mini-DOAS, is sensitive to all particle sizes, this finding validates the mini-DOAS inferred results as well as the proposed new retrieval methods.
The remarkable finding is a high amount of ice formed by large particles ($\sim 10^{-3} - 10^{-2}[g/m^3]$) at very high altitudes ($14 - 16km$). The ice particle mixing ratios are compared to the in situ water vapour concentrations (provided by UCATS and DLH) in order to investigate possible connections. The data confirm that very likely the air

masses probed by the mini-DOAS have a convective origin, and therefore large amounts of water vapour and large ice particles have been transported from the upper troposphere to the probed altitude region in the TTL. The convective outflows play a relevant role in this critical region for climate forcing and thus the physical characterization of such events is significant in order to study the global radiative net budget. The relative error of the inferred IWCs is assessed to 3.8%. The major limitation in the ice absorption band method is the characterization of the particle size distributions needed as input to the model and the overlapping of water vapour absorption (2ν) on the ice signal when very thin cirrus are investigated ($\mathrm{OD} < 0.02$).

The methods developed and validated with this work provide new insights into the microphysical properties of ice particles forming cirrus clouds in the TTL. Specifically, they provide measurements of cloud ODs, particles IWCs and ice water paths from a convective cirrus event occurred in the TTL during the winter season, when the TTL reaches the coldest temperature and extremely dry air enters the stratosphere. The occurrence frequency of such convective outflows may change in a changing climate and, since they strongly impact the TTL and the lower stratosphere, the knowledge of their microphysics is fundamental to determine their forcing effects (greenhouse vs. albedo). The results also validate the data collected by the mini-DOAS instrument, since a full spectral analysis of limb measured spectra in the near-IR was not yet performed and validated before.

Moreover, the proposed model is suitable to be easily applied in different contexts, i.e. measurements collected not only in the TTL but also at lower altitudes, where clouds formed by water in liquid an ice phase can be probed. In this respect, the optical and microphysical properties of liquid or mixed phase clouds could also be tackled.

Outlook

The applied methods to infer cloud ODs, IWCs and IWPs in the present study have several advantages over past methods, but they still face a couple of shortcomings. Accordingly, in future the following should be tackled.

i. To improve the radiative transfer model, the impact of different particle size distributions on the optical properties of ice particles and on the radiative transfer has to be investigated.

ii. Furthermore, the impact of different ice crystal shapes on the optical properties has to be studied using different approaches (e.g., T-matrix [129] or dipole discrete approximation [21]).

iii. To improve the fit procedures, the effects of different non-linear least-squared algorithms (e.g. Levenberg-Marquardt algorithm) should be investigated.

iv. The improved retrieval have to be applied to several other science flights. A particular focus is the GH flights outbound from Guam during the convective season in early 2014, where TTL cirrus were ubiquitous. The resulting dataset can provide new insights into the optical properties of convective cirrus clouds in the TTL. These data are useful for global radiative budget calculations, specifically when the radiative forcing effects of cirrus have to be accounted for. In this respect, new correlations between the different optical parameters can possibly be established and may serve to improve the representation of the studied processes in the general circulation models.

v. The improved retrieval can be used to investigate mixed phase clouds. It can be adapted to infer the optical properties of liquid water clouds or even liquid and ice water mixed clouds. In this case, the proposed new method can be applied

to the mini-DOAS measurements collected on board the HALO[3] aircraft at low altitudes (i.e. $10 - 12\text{km}$).

[3] http://www.dlr.de/dlr/en/desktopdefault.aspx/tabid-10203/339_read-268#/gallery/136

List of Figures

1 Obscured by clouds - Pink Floyd (1972). 1

1.1 Flammarion engraving. 5
1.2 Earth's atmosphere - vertical structure. 6
1.3 Global circulation. 9
1.4 Troposphere dynamic. 9
1.5 Schematic of the TTL. 13
1.6 Ice crystals habits. 16
1.7 CALIPSO and SAGE II cirrus data. 20

2.1 The NASA ATTREX logo. 23
2.2 The NASA Global Hawk UAS. 24
2.3 GH instrument arrangement. 25
2.4 The mini-DOAS instrument. 31
2.5 Science flights tracks. 33

3.1 Tesla experiment (1899). 37
3.2 Hg, Kr and Ar collected spectra. 40

3.3 DC and offset samples. 42
3.4 The mini-DOAS data. 43
3.5 The CPL data. 44
3.6 The Hawkeye data. 46

4.1 Laufmaschine - Drais 49
4.2 Sketch of the direction of the radiation. 50
4.3 Monte Carlo raytracing method. 55
4.4 Photon trajectory. 55
4.5 Simulations varying the number of photons 57
4.6 Modeling of the FOV. 59
4.7 Modeling of the ISF. 59
4.8 P, T, O_2, CO_2, H_2O, and cloud profiles. 63
4.9 Solar spectrum. 64
4.10 Ocean surface albedo vs. SZA. 65
4.11 Simulations varying the OSA. 66
4.12 OD vs. clear sky/cloudy conditions. 67
4.13 Spectral lines intensities for O_2, CO_2 and H_2O. 69
4.14 Doppler and broadening effects on the line shape. 72
4.15 FWHM for Doppler and pressure effects. 73
4.16 Absorption cross-sections for O_2, CO_2 and H_2O. 74
4.17 CKD vs. LBL methods. 76
4.18 PDFs for H_2O in function of PT. 77
4.19 Resulting absorption cross-sections for the CKD method. 78
4.20 Simulations on the CKD vs. LBL methods. 79
4.21 Rayleigh's phase function. 83
4.22 Ice water content parameterization for small and large crystals. 88

4.23 Particle size distribution for small and large crystals. 89
4.24 Effective radius and mean radius for small and large crystals. 90
4.25 Refractive index of ice. 93
4.26 The Henyey-Greenstein's phase function. 101
4.27 Q_{ext}, Q_{sca}, ϖ_0 and g for small and large crystals. 103
4.28 C_{ext}, C_{sca} and ϵ_{ext} for small and large crystals. 104
4.29 Flowchart of the RTM simulations. 106

5.1 Chess diagram (Lasker-Thomas, 1912). 107
5.2 Principle of DOAS. 109
5.3 O_2 absorption band analysis. 110
5.4 Simulations varying the IWC. 112
5.5 Iterating procedure for the O_2 band analysis. 114
5.6 Convolution function. 117
5.7 Optical properties of small and large particles with same OD. 120
5.8 Ice absorption band analysis. 123
5.9 Iterating procedure for the ice band analysis. 124

6.1 Scuola di Atene, Raffaello (1509-1511). 127
6.2 Mini-DOAS and CPL data for a flight segment. 129
6.3 Anisotropic vs. isotropic scattering medium. 130
6.4 Simulations varying the cloud position. 132
6.5 Simulations varying the asymmetry parameter. 132
6.6 Cloud clustering procedure: building of the layer. 133
6.7 OD_{cloud} and ϵ_{ext} results. Mini-DOAS vs. CPL/Hawkeye. 135
6.8 IWCs results. 138
6.9 IWCs mini-DOAS vs. Hawkeye and NOAA. 139

6.10 IWC_T parameterizations. 141
6.11 $\bar{r}_{<50}$, $\bar{r}_{>50}$, $r^{eff}_{<50}$ and $r^{eff}_{>50}$ results from the mini-DOAS. 142
6.12 IWC vs H_2O vapour mixing ratios. 143
6.13 Era-Interim back-trajectories. 144
6.14 IWCs vs. T. 146
6.15 D_{eff} vs. IWC from [73]. 148
6.16 D_{eff} vs. IWC for the mini-DOAS. 148
6.17 PSDs vs. IWC for Hawkeye and mini-DOAS. 150
6.18 IWPs results and correlations. 151
6.19 Le Faux Miroir - Magritte 155

List of Tables

1.1 Atmosphere's chemical composition. 7

2.1 List of instruments and relative topics. 26
2.2 Specifics of the mini-DOAS. 32
2.3 List of the science flights. 34

4.1 Photon number vs Poisson noise. 58
4.2 Geometric coordinates. 62
4.3 PT grid points for the cross-sections calculations. 75
4.4 Coefficients of the lognormal distribution. 86

List of Abbreviations and Acronyms

ATTREX: Airborne Topical TRopopause EXperiment

CALIPSO: Cloud-Aerosol Lidar and Infrared Pathfinder Satellite Observation

CKD: Correlated-K Distribution

CPI: Cloud Particle Imager

CPL: Cloud Physics Lidar

CPT: Cold Point Tropopause

DFRC: Dryden Flight Research Center (CA, US)

DLH: Diode Laser Hygrometer

DOAS: Differential Optical Absorption Spectroscopy

EA: Elevation Angle

FCDP: Fast Cloud Droplet Probe

FOV: Field Of View

GH: Global Hawk

GCM: General Circulation Model

HG: Henyey-Greenstein (phase function)

ISF: Instrument Slit Function

ITCZ: Inter-Tropical Convergence Zone

IWC: Ice Water Content

LBL: Line By Line

LZRH: Level of Zero net Radiative Heating

McArtim: Monte carlo Atmospheric radiative transfer inversion model

NIST: National Institute of Standards and Technologies

OD: Optical Depth

PSD: Particle Size Distribution

RTE: Radiative Transfer Equation

RTM: Radiative Transfer Model

SAGE: Stratospheric Aerosol and Gas Experiment

SRAA: Solar Relative Azimuth Angle

SSA: Single Scattering Albedo

SZA: Solar Zenith Angle

TTL: Tropical Tropopause Layer

UCATS: Unmanned aicraft systems Chromatograph Atmospheric Trace Species

WMO: World Meteorological Organization

Bibliography

[1] J. P. D. Abbatt, J. L. Thomas, K. Abrahamsson, C. Boxe, A. Granfors, A. E. Jones, M. D. King, A. Saiz-Lopez, P. B. Shepson, J. Sodeau, D. W. Toohey, C. Toubin, R. von Glasow, S. N. Wren, and X. Yang, "Halogen activation via interactions with environmental ice and snow in the polar lower troposphere and other regions", Atmos. Chem. Phys. **12**, 6237-6271 (2012).

[2] G. Anderson, S. Clough, F. Kneizys, J. Chetwynd, and E. Shettle , "AFGL atmospheric constituent profiles (0-120km)", Tech. Rep. **AFGL-TR-86-0110**, Air Force Geophys. Lab., Hanscom Air Force Base, Bedford, Mass. (1986).

[3] J. Aschmann, B.-M. Sinnhuber, E. L. Atlas, and S. M. Schauffler, "Modeling the transport of very short-lived substances into the tropical upper troposphere and lower stratosphere", Atmos. Chem. Phys. **9** (23), 9237-9247 (2009).

[4] J. Aschmann, B.-M. Sinnhuber, M. P. Chipperfield, and R. Hossaini, "impact of deep convection and dehydration on bromine loading in the upper troposphere and lower stratosphere", Atmos. Chem. Phys. **11** (6), 2671-2687 (2011).

[5] M. P. Bailey, and J. Hallett "A Comprehensive Habit Diagram for Atmospheric Ice Crystals: Confirmation from the Laboratory, AIRS II, and Other Field Studies", J. Atmos. Sci. **66**, 2888-2899 (2009).

[6] A. J. Baran, and S. Havemann, "The dependence of retrieved cirrus ice-crystal effective dimension on assumed ice-crystal geometry and size-distribution function at solar wavelengths", Q. J. R. Meteorol. Soc. **130**, 2153-2167 (2004).

[7] S. Borrmann, S. Solomon, L. Avallone, and J. E. Dye, "On the occurrence of ClO in cirrus clouds and volcanic aerosol in the tropopause region", Geophys. Res. Lett. **24**, 2011-2014 (1997).

[8] B. Bregman, P. Wang, and J. Lelieveld, "Chemical ozone loss in the tropopause region on subvisible ice clouds, calculated with a chemistry-transport model", J. Geophys. Res. **107** (D3), 4032 (2002).

[9] S. Brinckmann, A. Engel, H. Bönisch B. Quack, and E. Atlas, "Short-lived brominated hydrocarbons - observations in the source regions and the tropical tropopause layer", Atmos. Chem. Phys. **12** (3), 1213-1228 (2012).

[10] D. R. Bates, "Rayleigh scattering by air", Planet. Space Sci. **32**, 785-790 (1984).

[11] B. A. Bodhaine, N. B. Wood, E. G. Dutton, and J. R. Slusser, "On Rayleigh optical depth calculations", J. Atmos. Oceanic Technol. **16**, 1854-1861 (1999).

[12] F. P. Bretherton, and V. E. Suomi, *First International Satellite Cloud Climatology Project Regional Experiment (FIRE) Research Plan*, 76 pp. [Available from the National Climatic Program Office, Rm. 108, 11400 Rockvillle, MD., 20852] (1983).

[13] D. C. Catling, and K. J. Zahnle, "The Planetary Air Leak", Scientific American **May 2009**, p. 26 (accessed 25 July 2012).

[14] K. V. Chance, and R. J. D Spurr, "Ring effect studies: Rayleigh scattering, including molecular parameters for rotational Raman scattering, and the Fraunhofer spectrum", App. Opt. **36** (21), 5224-5230 (1997).

[15] S. Chandrasekhar, *Radiative Transfer* (Oxford Press, 1950).

[16] J. S. Daniel, S. Solomon, R. W. Portmann, A. O. Langford, C. S. Eubank, E. G. Dutton, and W. Madsen, "Cloud liquid water and ice measurements from spectrally resolved near-infrared observations: A new technique", J. Geophys. Res. **107** (D21), 4599 (2002).

[17] J. S. Daniel, R. W. Portmann, H. L. Miller, S. Solomon, A. O. Langford, C. S. Eubank, R. Schofield, D. D. Turner, and M. D. Shupe, "Cloud property estimates from zenith spectral measurements of scattered sunlight between 0.9 and 1.7μm", J. Geophys. Res. **111**, D16208 (2005).

[18] S. M. Davis, and Coauthors, "In situ and lidar observations of tropopause subvisible cirrus clouds during TC4", J. Geophys. Res. 115, (2010).

[19] A. E. Dessler, and P. Yang, "The distribution of tropical thin cirrus clouds inferred from Terra MODIS data", J. Clim. **16**, 1241-1247 (2003).

[20] T. Deutschmann, S. Beirle, U. Frieß, M. Grzegorski, C. Kern, L. Kritten, U. Platt, J. Pukite, T. Wagner, B. Werner, and K. Pfeilsticker, "The Monte Carlo Atmospheric Radiative Transfer Model McArtim: Introduction and Validation of Jacobians and 3D Features", J. Quant. Spectrosc. Radiat. Transfer **112** (6), 1119-1137 (2011).

[21] H. DeVoe, "Optical properties of molecular aggregates. I. Classical model of electronic absorption and refraction", J. Chem. Phys. **41**, 393-400 (1964).

[22] E. E. Ebert, and J. A. Curry, "A parameterization of ice cloud optical properties for climate models", J. Geophys. Res. **97**, 3831-3836 (1992).

[23] B. Edlén, "The dispersion of standard air", J. Opt. Soc. Amer. **43**, 339-344 (1953).

[24] K. F. Evans and A. H. Evans, "The Prospect for Remote Sensing ofCirrus Clouds with a Submillimeter-Wave Spectrometer", J. App. Met. **38**, 514-525 (1999).

[25] P. M. Forster, and K. P. Shine, "Assessing the climate impact of trends in stratospheric water vapor", Geophy. Res. Lett. **29** (6), 1086 (2002).

[26] F. Franks, "Nucleation of ice and its management in ecosystems", Philosophical Transactions of the Royal Society A. **361** (1804), 557-574 (2003).

[27] Q. Fu and K. N. Liou, "On the correlated k-distribution method for radiative transfer in nonhomogeneous atmospheres", J. Atmos. Sci. **49**, 2139-2156 (1992).

[28] Q. Fu, Y. X. Hu, and Q. Yang, "Identifying the top of the tropical tropopause layer from vertical mass flux analysis and CALIPSO lidar cloud observations", Geophys. res. Lett. **34**, L14813 (2007).

[29] Q. Fu, "A New Parameterization of an Asymmetry Factor of Cirrus Clouds for Climate Models", J. Atmos. Sci. **64**, 4140-4150 (2007).

[30] S. Fueglistaler, and P. H. Haynes, "Control of interannual longer-term variability of stratospheric water vapor", J. Geophyis. Res. **110**, D24108 (2005).

[31] S. Fueglistaler, A. E. Dessler, T. J. Dunkerton, I. Folkins, Q. Fu, and P. W. Mote, "Tropical tropopause layer", Rev. Geophyis. **47** (1), 1-31 (2009).

[32] A. Gettelman, and P. M. d. F. Forster, "A climatology of the tropical tropopause layer", J. Meteor. Soc. Japan **80** (4B), 911-924 (2002).

[33] A. Gettelman, P. M. de F. Forster, M. Fujiwara, Q. Fu, H. Vo´omel, L. K. Gohar, C. Johanson, and M. Ammerman, "Radiation balance of the tropical tropopause layer", J. Geophys. Res. **109**, D07103 (2004).

[34] J.-F. Gayet, J. Ovarlez, V. Shcherbakov, J. Str´om, U. Schumann, A. Minikin, F. Auriol,A. Petzold, and M. Monier, "Cirrus cloud microphysical and optical properties at southern and northern midlatitudes during the INCA experiment", J. Geophys. Res. **109**, D20206 (2004).

[35] J.-F. Gayet, G. Mioche, V. Shcherbakov, C. Gourbeyre, R. Busen, and A. Minikin, "Optical properties of pristine ice crystals in mid-latitude cirrus clouds: a case study during CIRCLE-2 experiment", Atmos. Chem. Phys. **11**, 2537-2544 (2011).

[36] R. M. Goody, R. West, L. Chen, and D. Crisp, "The correlated-k method for radiation calculation in nonhomogeneous atmospheres", J. Quant. Spectrosc. Radiat. Transfer **42**, 539-550 (1989).

[37] J. F. Grainger and J. Ring, "Anomalous Fraunhofer line profiles", Nature London **193**, 762 (1962).

[38] J. E. Hansen and L. D. Travis, "Light scattering in planetary atmospheres", Space Sci. Rev. **16**, 527-610 (1974).

[39] L. G. Henyey and J. L. Greenstein, "Diffuse Radiation in the Galaxy", Ap. J. **93**, 70 (1941).

[40] A. J. Heymsfield, and J. Iaquinta, "Cirrus Crystal Terminal Velocities", J. Atmos. Sci. **57**, 916-938 (1999).

[41] A. J. Heymsfield, S. Matrosov, and B. Baum, "Ice Water Path-Optical Depth Relationships for Cirrus and Deep Stratiform Ice Cloud Layers", J. Appl. Meteor. **42**, 1369-1390 (2003).

[42] D. C. Harris, M. D. Bertolucci, *Symmetry and Spectroscopy* (Dover Publications, 1989).

[43] M. von Hobe, J.-U. Groß, G. G´unther, P. Konopka, I. Gensch, M. Kr´amer, N. Spelten, A. Afchine, C. Schiller, A. Ulanovsky, N. Sitnikov, G. Shur, V. Yushkov, F. Ravegnani, F. Cairo, A. Roiger, C. Voigt, H. Schlager, R. Weigel, W. Frey, S. Borrmann, R. M´uller, and F. Stroh, "Evidence for heterogeneous chlorine activation in the tropical UTLS", Atmos. Chem. Phys. **11**, 241-256 (2011).

[44] S. Hollars, Q. Fu, J. Comstock, and T. Ackerman, "Com- parison of cloud-top height retrievals from ground-based 35 GHz MMCR and GMS-5 satellite observations at ARM TWP Manus site", Atmos. Res. **72**, 169-186 (2004).

[45] R. Hossaini, M. P. Chipperfield, W. Feng, T. J. Breider, E. Atlas, S. A. Montzka, B. R. Miller, F. Moore, And J. Elkins, "The contribution of natural and anthropogenic very short-lived species to stratospheric bromine", Atmos. Chem. Phys. **12** (1), 371-380 (2012).

[46] J. Huang, and M. B. McElroy, "Contributions of the Hadley and Ferrel Circulations to the Energetics of the Atmosphere over the Past 32 Years", Journal of Climate **27** (7), 2656-2666 (2014).

[47] H. C. van de Hulst, *Light Scattering by Small Particles* (Dover, New York, 1981).

[48] J. Humlíček, "Optimized computation of the Voigt and complex probability functions", J. Quant. Spectrosc. Radiat. Transfer **27**, 437-444 (1982).

[49] F. Immler, and O. Schrems, "Determination of tropical cirrus properties by simultaneous LIDAR and radiosonde measurements", Geophys. Res. Lett. **29** (23), 2090 (2002).

[50] P. Irwin, *Giant planets of our solar system: an introduction* (Springer 2006).

[51] E. Järvinen, M. Schnaiter, G. Mioche, O. Jourdan, V. N. Shcherbakov, A. Costa, A. Afchine, M. Krämer, F. Heidelberg, T. Jurkat, C. Voigt, H. Schlager, L. Nichman, M. Gallagher, E. Hirst, C. Schmitt, A. Bansemer, A. Heymsfield, P. Lawson, U. Tricoli, K. Pfeilsticker, P. Vochezer, O. Möhler, and T. Leisner, "Quasi-Spherical Ice in Convective Clouds", Amer. Meteor. Soc. **73** (18), 3885-2026 (2016).

[52] J. D. Jackson, *Classical Electrodynamics. Third Edition* (J. Wiley & Sons Inc., 1999).

[53] E. Jensen, S. Kinne, and O. Toon, "Tropical cirrus cloud radiative forcing: Sensitivity studies", Geophys. Res. Lett. **21** (18), 2023-2026 (1994).

[54] E. Jensen, O. B. Toon, L. Pfister, and H. B. Selkirk "Dehydration of the upper troposphere and lower stratosphere by subvisible cirrus clouds near the tropical tropopause", Geophys. Res. Lett. **23**, 825-828 (1996).

[55] E. Jensen, O. B. Toon,H. B. Selkirk, J. D. Spinhirne, and M. R. Schoeberl, "On the formation and persistence of subvisible cirrus clouds near the tropical tropopause", J. Geophys. Res. **101** (D16), 21361 (1996).

[56] E. J. Jensen, L. Pfister, T. V. Bui, P. Lawson, B. Baker, Q. Mo, D. Baumgardner, E. M. Weinstock, J. B. Smith, E. J. Moyer, T. F. Hanisco, D. S. Sayres, J. M. St. Clair, M. J. Alexander, O. B. Toon, and J. A. Smith, "Formation of large ($\simeq 100\mu m$) ice crystals near the tropical tropopause", Atmos. Chem. Phys. **8**, 1621-1633 (2008).

[57] E. J. Jensen, and Coauthors, "Ice nucleation and dehydration in the Tropical Tropopause Layer". Proc. of National Acad. Sci. **110** (6), (2013a).

[58] E. J. Jensen, and Coauthors, "The NASA Airborne Tropical TRopopause EXperiment (ATTREX)", SPARC Newsl. **41**, 15-24 (2013b).

[59] E. Jensen, L. Pfister, D. Jordan, T. Bui, R. Ueyama, H. Singh, T. Thornberry, A. Rollins, R. Gao, D. Fahey, K. Rosenlof, J. Elkins, G. Diskin, J. DiGangi, R. Lawson, S. Woods, E. Atlas, M. Navarro Rodriguez, S. Wofsy, J. Pittman, C. Bardeen, O. Toon, B. Kindel, P. Newman, M. McGill, D. Hlavka, L. Lait, M. Schoeberl, J. Bergman, H. Selkirk, M. Alexander, J. Kim, B. Lim, J. Stutz, and K. Pfeilsticker, "The NASA Airborne Tropical TRopopause EXperiment (ATTREX): High-Altitude Aircraft Measurements in the Tropical Western Pacific", Bull. Amer. Meteor. Soc. doi:10.1175/BAMS-D-14-00263.1, in press (2015).

[60] Z. Jin, T. P. Charlock, W. L. Smith Jr., and K. Rutledge, "A parameterization of ocean surface albedo", Geophys. Res. Lett. **31**, L22301 (2004).

[61] H. M. Jones, J. Haywood, F. Marenco, D. O'Sullivan, J. Meyer, R. Thorpe, M. W. Gallagher, M. Kramer, K. N. Bower, G. Radel, A. Rap, A. Woolley, P. Forster6, and H. Coe, "A methodology for in-situ and remote sensing of microphysical and radiative properties of contrails as they evolve into cirrus", Atmos. Chem. Phys. **12**, 8157-8175 (2012).

[62] M. C. Kelley, *The Earth's Ionosphere: Plasma Physics and Electrodynamics (2nd ed.)* (Academic Press, 2009).

[63] B. C. Kindel, P. Pilewskie, K. S. Schmidt, T. Thornberry, A. Rollins, and T. Bui, "Upper-troposphere and lower-stratosphere water vapor retrievals from the 1400 and 1900 nm water vapor bands", Atmos. Meas. Tech. **8**, 1147-1156 (2015).

[64] M. King, S. Tsay, S. Platnick, M. Wang, and K. Liou, "Cloud retrieval algorithms for MODIS: Optical thickness, effective particle radius, and thermodynamic phase", emphMODIS Algorithm Theoretical Basis Document No. ATBD-MOD-05 MOD-06 - Cloud product, p.83 (1997).

[65] A. V. Korolev, G. A. Isaac, and J. Hallett, "Ice particle habits in Arctic clouds", Geophys. Res. Lett. **26**, 1299-1302 (1999).

[66] L. Kritten, A. Butz, M. Dorf, T. Deutschmann, S. Kühl, C. Prados-Roman, J. Pukite, A. Rozanov, R. Schofield, and K. Pfeilsticker, "Time dependent profile retrieval of UV/vis absorbing radicals from balloon-borne limb measurements - a case study on NO_2 and O_3", Atmos. Meas. Tech. **3**, 933-946 (2010).

[67] M. Kuntz, "A new implementation of the Humlíček algorithm for the calculation of the Voigt profile function", J. Quant. Spectrosc. Radiat. Transfer **57**, 819-824 (1997).

[68] R. L. Kurucz, I. Furenlid, J. Brault, and L. Testerman, "Solar flux atlas from 296 to 1300 nm", National Solar Observatory, Sunspot, New Mexico, U.S.A., (1984).

[69] R. P. Lawson, D. O'Connor, P. Zmarzly, K. Weaver, B. A. Baker, Q. Mo, and H. Jonsson, "The 2D-S (Stereo) probe: Design and preliminary tests of a new airborne, high-speed, high-resolution imaging probe", J. Atmos. Ocean. Tech. **23**, 1462-1477 (2006).

[70] J. Lee, P. Yang, A. E. Dessler, B.-C. Gao, and S. Platnick, "Distribution and Radiative Forcing of Tropical Thin Cirrus Clouds", J. Atmos. Sci. **66**, 3721-3731 (2009).

[71] K. N. Liou, "Influence of cirrus clouds on weather and climate processes: A global perspective", Mon. Weather Rev. **114**, 1167-1199 (1986).

[72] K. N. Liou, *Radiation and Cloud Processes in the Atmosphere* (Oxford Univ. Press, 1992).

[73] K. N. Liou,, Y. Gu, Q. Yue, and G. McFarguhar, "On the correlation between ice water content and ice crystal size and its application to radiative transfer and general circulation models", Geophys. Res. Lett. **35**, L13805 (2008).

[74] C. Liu, and E. J. Zipster, "Global distribution of convection penetrating the tropical tropopause", J. Geophys. Res. **110**, D23104 (2005).

[75] Y. Liu, W. Wu, M. P. Jensen, and T. Toto, "Relationship between cloud radiative forcing, cloud fraction and cloud albedo, and new surface-based approach for determining cloud albedo", Atmos. Chem. Phys. **11**, 7155-7170 (2011).

[76] D. Lowe, and A. R. MacKenzie, "Polar stratospheric cloud microphysics and chemistry", J. Atmos. Solar-Terrestrial Phys. **70** (1), 13-40 (2008).

[77] Z. Luo, T. Peter, H. Wernli, S. Fueglistaler, M. Wirth, C. Kiemle, H. Flentje, V. A. Yushkov, V. Khattatov, V. Rudakov, A. Thomas, S. Borrmann, G. Toci, P. Mazzinghi, J. Beuermann, C. Schiller, F. Cairo, G. Di Don-Francesco, A. Adriani, C. M. Volk, J. Strom, K. Noone, V. Mitev, R. A. MacKenzie, K. S. Carslaw, T. Trautmann, V. Santacesaria, and L. Stefanutti, "Ultrathin tropical tropopause clouds (UTTCs): II. Stabilization and destabilization mechanism", Atmos. Chem. Phys. **3**, 1093-1100 (2003).

[78] Z. Luo, and W. B. Rossow, "Characterizing tropical cirrus life cycle, evolution, and interaction with upper-tropospheric water vapor using Lagrangian trajectory analysis of satellite observations", J. Clim. **17**, 4541-4563 (2004).

[79] A. Marshak and A.B. Davis, *3D Radiative Transfer in Cloudy Atmospheres* (Springer, Berlin-Heidelberg, 2005).

[80] S. Massie, A. Gettelman, W. Randel, and D. Baumgardner, "Distribution of tropical cirrus in relation to convection", J. Geophys. Res. **107** (D21), 4591 (2002).

[81] G. M. McFarquhar and A. J. Heymsfield, "Parametrization of tropical cirrus ice crystal size distributions and implications for radiative transfer: results from CEPEX", J. Atmos. Sci. **54**, 2187-2200 (1997).

[82] G. M. McFarquhar, A. J. Heymsfield, J. Spinhirne, and B. Hart, "Thin and subvisual tropopause tropical cirrus: Observations and radiative impacts", J. Atmos. Sci. **57**, 1841-1853 (2000).

[83] G. M. McFarquhar, J. Um, M. Freer, D. Baumgardner, G. L. Kok, and G. Mace, "The importance of small ice crystals to cirrus properties: Observations from the Tropical Warm Pool International Cloud Experiment (TWP-ICE)", Geophys. Res. Lett. **57**, L13803 (2007).

[84] G. Mie, "Beiträge zur Optik trüber Medien, speziell kolloidaler Metallösungen", Annalen der Physik **330**, 377-445 (1908).

[85] M. I. Mishchenko, J. M. Dlugach, E. G. Yanovitskij, and N. T. Zakharova, "Bidirectional reflectance of flat, optically thick particulate laters: an efficient radiative transfer solution and applications to snow and soil surfaces", J. Quant. Spectrosc. Radiat. Transfer *63*, 409-432 (1999).

[86] M. I. Mishchenko, L. D. Travis, A. A. Lacis, *Scattering, Absorption, and Emission of Light* (NASA Goddard Institute for Space Studies, New York, 2004).

[87] R. Müller, and T. Peter, "The Numerical Modelling of the Sedimentation of Polar Stratospheric Cloud Particles", Ber. Bunsenges. Phy. Chem. **96** (3), 353-361 (1992).

[88] L. Nazarenko, et al., "Future climate change under RCP emission scenarios with GISS ModelE2", J. Adv. Model. Earth Syst. **7**, 244-267 (2015).

[89] R. E. Newell, Y. Zhu, E. V. Browell, W. G. Read, and J. W. Waters, "Walker circulation and tropical upper tropospheric water vapor", J. Geophys. Res. **101**, 1961-1974 (1996).

[90] L. L. Pan, L. C. Paulik, S. B. Honomichl, L. A. Munchak, J. Bian, H. B. Selkirk, and H. Vömel, "Identification of the tropical tropopause transition layer using the ozone-water vapor relationship", J. Geophys. Res. Atmos. **119**, 3586-3599 (2014).

[91] E. R. Peck and K. Reeder, "Dispersion of air", J. Opt. Soc. Amer. **62**, 958-962 (1972).

[92] R. Penndorf, "Tables of the refractive index from standard air and Rayleigh scattering coefficient for the spectral region between 0.2 and 20.0 μ and their application to atmospheric optics", J. Opt. Soc. Amer. **47**, 176-182 (1957).

[93] T. Peter, B. P. Luo, M. Wirth, C. Kiemle, H. Flentje, V. A. Yushkov, V. Khattatov, V. Rudakov, A. Thomas, S. Borrmann, G. Toci, P. Mazzinghi, J. Beuermann, C. Schiller, F. Cairo, G. Di Donfrancesco, A. Adriani, C. M. Volk, J. Strom, K. Noone, V. Mitev, R. A. MacKenzie, K. S. Carslaw, T. Trautmann, V. Santacesaria, and L. Stefanutti, "Ultrathin tropical tropopause clouds (UTTCs): I. Cloud morphology and occurrence", Atmos. Chem. Phys. **3**, 1083-1091 (2003).

[94] L. Pfister, H. B. Selkirk, E. J. Jensen, M. R. Schoeberl, O. B. Toon, E. V. Browell, W. B. Grant, B. Gary, M. J. Mahoney, T. V. Bui, and E. Hintsa, "Aircraft observations of thin cirrus clouds near the tropical tropopause", J. Geophys. Res. **106** (D9), 9765-9786 (2001).

[95] S. Platnick, M. D. King, S. A. Ackerman, W. P. Menzel, B. A. Baum, J. C. Riedi, and R. A. Frey, "The MODIS Cloud Products: Algorithms and Examples From Terra", IEEE Trans. Geosci. Remote Sens. **41** (2), 459-473 (2003).

[96] P. J. Popp, R. S. Gao, T. P. Marcy, D. W. Fahey, P. K. Hudson, T. L. Thompson, B. Kärcher, B. A. Ridley, A. J. Weinheimer, D. J. Knapp, D. D. Montzka, D. Baumgardner, T. J. Garrett, E. M. Weinstock, J. B. Smith, D. S. Sayres, J. V. Pittman, S. Dhaniyala, T. P. Bui, and M. J. Mahoney, "Nitric acid uptake on sub-tropical cirrus cloud particles", J. Geophys. Res. **109**, D06302 (2004).

[97] P. J. Popp, T. P. Marcy, E. J. Jensen, B. Kärcher, D. W. fahey, R. S. Gao, T. L. Thompson, K. H. Rosenlof, E. C. Richard, R. L. Herman, E. M. Weinstock, J. B. Smith, R. D. May, H. Vömel, J. C. Wilson, A. J. Heymsfield, M. J. Mahoney, and A. M. Thompson, "The observation of nitric acid containing particles in the tropical lower stratosphere", Atmos. Chem. Phys. **6** (3), 601-611 (2006).

[98] U. Platt and J. Stutz, *Differential Optical Spectroscopy. Principles and Applications* (Springer, Berlin-Heidelberg, 2008).

[99] C. Prados-Roman, A. Butz, T. Deutschmann, M. Dorf, L. Kritten, A. Minikin, U. Platt, H. Schlager, H. Sihler, N. Theys, M. Van Roozendael, T. Wagner, and K. Pfeilsticker, "Airborne DOAS limb measurements of tropospheric trace gas profiles: case studies on the profile retrieval of O_4 and BrO", Atmos. Meas. Tech. **4**, 1241-1260 (2011).

[100] V. Ramanathan, and W. Collins, "Thermodynamic regulation of ocean warming by cirrus clouds deduced from observations of the 1987 El Nino", Nature **351**, 27-32 (1991).

[101] W. J. Randel, and E. J. Jensen, "Physical processes in the tropical tropopause layer and their roles in a changing climate", Nat. Geosci. **6** (3), 169-176 (2013).

[102] C. V. Raman, "A new radiation", Indian J. Phys. **2**, 387-398 (1928).

[103] C. D. Rodgers, *Inverse Methods for Atmospheric Sounding: Theory and Practice* (World Scientific Publishing Co. Pte. Ltd., 2000).

[104] A. Roesch, M. Wild, R. Pinker, and A. Ohmura, "Comparison of spectral surface albedos and their impact on the general circulation model simulated surface climate", J. Geophys. Res. **107** (D14), 4221 (2002).

[105] P. Rolland, K. N. Liou, M. D. King, S. C. Tsay, and G. McFarquhar, "Remote sensing of optical and microphysical properties of cirrus clouds using Moderate-Resolution Imaging Spectroradiometer channels: Methodology and sensitivity to physical assumptions", J. Geophys. Res. **105** , 11721-11738 (2000).

[106] L. S. Rothman *et al.*, "The HITRAN2012 molecular spectroscopic database", J. Quant. Spectrosc. Radiat. Transfer **130**, 139-204 (2013).

[107] J. H. Seinfeld and S. N. Pandis, *Atmospheric Chemistry and Physics: From Air Pollution to Climate Change 3rd Edition* (Wiley, 2016).

[108] K. Sassen, and B. S. Cho, "Subvisual-thin cirrus clouds lidar data set for satellite verification and climatological research", J. Appl. Meteorol. **31**, 1275-1285 (1992).

[109] C. Schiller, A. Afchine, N. Eicke, C. Feigl, H. Fischer, A. Giez, P. Konopka, H. Schlager, F. Tuitjer, F. G. Wienhold, and M. Zoger, "Ice particle formation and sedimentation in the tropopause region: A case study based on in situ measurements of total water during POLSTAR 1997", Geophys. Res. Lett. **26** (14), 2219-2222 (1999).

[110] C. Schiller, M. Krämer, A. Afchine, N. Spelten, and N. Sitnikov, "Ice water content of Arctic, midlatitude, and tropical cirrus", J. Geophys. Res. **113**, D24208 (2008).

[111] M.R. Schoeberl, A. E. Dessler, T. Wang, M. A. Avery, and E. J. Jensen, "Cloud formation, convection, and stratospheric dehydration", Earth and Space Science **1**, 1-17 (2014).

[112] M. Šimečková, D. Jacquemart, L. S. Rothman, R. R. Gamache, and A. Goldman, "Einstein A-coefficients and statistical weights for molecular absorption transitions in the HITRAN database", J. Quant. Spectrosc. Radiat. Transfer **98**, 130-155 (2006).

[113] S. C. Sherwood, "On moistening of the tropical troposphere by cirrus clouds", J. Geophys. Res. **104**, 11949-11960 (1999).

[114] K. M. Smith, D. A. Newnham, and R. G. Williams, "Collision-induced absorption of solar radiation in the atmosphere by molecular oxygen at $1.27\mu m$: Field observations and model calculations", J. Geophys. Res. **106** (D7), 7541-7552 (2001).

[115] S. Solomon, S. Borrmann, R. R. Garcia, R. Portman, L. Thomason, L. R. Poole, D. Winkler, and M. P. McCormick, "Heterogeneous chlorine chemistry in the tropopause region", J. Geophys. Res. **102**, 21411-21429 (1997).

[116] S. Solomon, K. H. Rosenlof, R. W. Portmann, J. S. Daniel, S. M. Davis, T. J. Sanford, and G. K. Plattner, "Contributions of Stratospheric Water Vapor to Decadal Changes in the Rate of Global Warming", Science **327**, 1219-1223 (2010).

[117] G. L. Stephens, S.-C. Tsay, P. W. Stackhouse, and P. J. Flatau "The relevance of the Microphysical and Radiative Properties of Cirrus Clouds to Climate and Climatic Feedback", J. Atmos. Sci. **47** (14), 1742-1753 (1990).

[118] J. Stutz, B. Werner, M. Spolaor, L. Scalone, J. Festa, C. Tsai, R. Cheung, S. F. Colosimo, U. Tricoli, R. Raecke, R. Hossaini, M. P. Chipperfield, W. Feng, Ru-Shan Gao, E. J. Hintsa, J. W. Elkins, F. L. Moore, B. Daube, J. Pittman, S. Wofsy, and K. Pfeilsticker, "A New Differential Optical Absorption Spectroscopy Instrument to Study Atmospheric Chemistry from a High-Altitude Unmanned Aircraft", Atmos. Meas. Tech. **10**, 1017-1042 (2017).

[119] A. Tarantola, *Inverse Problem Theory and Methods for Model Parameter Estimation*, (Society for Industrial and Applied Mathematics, 2005)

[120] T. D. Thornberry, A. W. Rollins, R. S. Gao, L. A. Watts, S. J. Ciciora, R. J. McLaughlin, and D. W. Fahey, "A two-channel, tunable diode laser-based hygrometer for measurement of water vapor and cirrus cloud ice water content in the upper troposphere and lower stratosphere", Atmos. Meas. Tech. **8**, 211-244 (2015).

[121] G. Thuillier, M. Hersé, D. Labs, T. Foujols, W. Peetermans, D. Gillotay, P. C. Simon, and H. Mandel, "The solar spectral irradiance from 200 to 2400 nm as measured by the SOLSPEC spectrometer from the ATLAS and EURECA missions", Solar Phys. **214**, 1-22 (2003).

[122] S. M. Uppala, P. W. KÅllberg, A. J. Simmons, U. Andrae, V. D. C. Bechtold, M. Fiorino, J. K. Gibson, J. Haseler, A. Hernandez, G. A. Kelly, X. Li, K. Onogi, S. Saarinen, N. Sokka, R. P. Allan, E. Andersson, K. Arpe, M. A. Balmaseda, A. C. M. Beljaars, L. V. D. Berg, J. Bidlot, N. Bormann, S. Caires, F. Chevallier, A. Dethof, M. Dragosavac, M. Fisher, M. Fuentes, S. Hagemann, E. Hólm, B. J.

Hoskins, L. Isaksen, P. A. E. M. Janssen, R. Jenne,A. P. Mcnally,J.-F. Mahfouf,J.-J. Morcrette, N. A. Rayner, R. W. Saunders, P. Simon, A. Sterl, K. E. Trenberth, A. Untch, D. Vasiljevic, P. Viterbo, and J. Woollen, "The ERA-40 re-analysis", Q. J. R. Meteorol. Soc. **131**, 2961-3012 (2005).

[123] R. Volkamer, S. Baidar, T. L. Campos, S. Coburn, J. P. DiGangi, B. Dix, E. W. Eloranta, T. K. Koenig, B. Morley, I. Ortega, B. R. Pierce, M. Reeves, R. Sinreich, S. Wang, M. A. Zondlo, and P. A. Romashkin, "Aircraft measurements of BrO, IO, glyoxal, NO_2, H_2O, $O_2 - O_2$ and aerosol extinction profiles in the tropics: comparison with aircraft-/ship-based in situ and lidar measurements", Atmos. Meas. Tech. **8**, 2121-2148 (2015).

[124] J. M. Wallace and P. V. Hobbs, *Atmospheric Science. An Introductory Survey*, (Elsevier Inc., 2006)

[125] P.-H. Wang, P. Minnis, M. P. McCormick, G. S. Kent, and K. M. Skeens, "A 6-year climatology of cloud occurrence frequency from Stratospheric Aerosol and Gas Experiment II observations (1985-1990)", J. Geophys. Res. **101** (D23), 29407-29429 (1996).

[126] Z. Wang, and K. Sassen, "Cirrus cloud microphysical property retrieval using lidar and radar measurements. Part I: Algorithm description and comparison with in situ data", J. Appl. Meteor. **41**, 218-229 (2002).

[127] X. Wang, K. N. Liou, S. S. C. Ou, G. G. Mace, and M. Deng, "Remote sensing of cirrus cloud vertical size profile using MODIS data", J. Geophys. Res. **114** (D9), D09205 (2009).

[128] S. G. Warren and R. E. Brandt, "Optical constants of ice from the ultraviolet to the microwave: A revised compilation", J. Geophys. Res. **113**, D14220 (2008).

[129] P. C. Waterman, "Matrix formulation of electromagnetic scattering", Proceedings of the IEEE **53**, 805-812 (1965).

[130] B. Werner, J. Stutz, M. Spolaor, L. Scalone, R. Raecke, J. Festa, S. F. Colosimo, R. Cheung, C. Tsai, R. Hossaini, M. P. Chipperfield, G. S. Taverna, W. Feng, J. W. Elkins, D. W. Fahey, R.-S. Gao, E. J. Hintsa, T. D. Thornberry, F. L. Moore, M. A. Navarro, E. Atlas, B. C. Daube, J. Pittman, S. Wofsy, and K. Pfeilsticker, "Probing the subtropical lowermost stratosphere and the tropical upper troposphere and tropopause layer for inorganic bromine", Atmos. Chem. Phys. **17**, 1161-1186 (2017).

[131] D. M. Winker, W. H. Hunt, and M. J. McGill, "Initial performance assessment of CALIOP", Geophys. Res. Lett. **34**, L19803 (2007).

[132] D. M. Winker, J. Pelon, J. A. Coakley Jr., S. A. Ackerman, R. J. Charlson, P. R. Colarco, P. Flamant, Q. Fu, R. M. Hoff, C. Kittaka, T. L. Kubar, H. Le Treut, M. P. Mccormick, G. Megie, L. Poole, K. Powell, C. Trepte, M. A. Vaughan, and B. A. Wielicki, "The CALIPSO mission. A Global 3D View of Aerosols and Clouds", Bull. Amer. Meteor. Soc., doi:10.1175/2010BAMS3009.1 (2010).

[133] International Meteorological Vocabulary (2nd ed.). Geneva: Secretariat of the World Meteorological Organization. 1992. p. 636. ISBN 92-63-02182-1.

[134] K. Wolf, A. Ehrlich, T. Hüneke, K. Pfeilsticker, F. Werner, M. Wirth, and M. Wendisch, "Potential of remote sensing of cirrus optical thickness by airborne spectral radiance measurements in different viewing angles and nadir geometry", Atmos. Chem. Phys. Discuss., doi:10.5194/acp-2016-970, in review (2016).

[135] D. Wylie, and W. Menzel, "Eight years of high cloud statistics using HIRS", J. Clim. **12**, 170-185 (1999).

[136] P. Yang, L. Bi, B. A. Baum, K.-N. Liou, G. W. Kattawar, M. I. Mishchenko, and B. Cole, "Spectrally Consistent Scattering, Absorption, and Polarization Properties of Atmospheric Ice Crystals at Wavelengths from 0.2 to 100μm", J. Atmos. Sci. **70**, 330-347 (2013).

[137] Q. Yang, Q. Fu, and Y. Hu, "Radiative impacts of clouds in the tropical tropopause layer", J. Geophys. Res. **115**, D00H12 (2010).

Publications

B Werner, J Stutz, M Spolaor, L Scalone, R Raecke, J Festa, SF Colosimo, R Cheung, C Tsai, R Hossaini, MP Chipperfield, GS Taverna, W Feng, JW Elkins, DW Fahey, RS Gao, EJ Hintsa, TD Thornberry, FL Moore, MA Navarro, E Atlas, BC Daube, J Pittman, S Wofsy, and K Pfeilsticker, "**Probing the subtropical lowermost stratosphere and the tropical upper troposphere and tropopause layer for inorganic bromine**", *Atmos. Chem. Phys. 17*, 1161-1186 (2017).

J Stutz, B Werner, M Spolaor, L Scalone, J Festa, C Tsai, R Cheung, SF Colosimo, U Tricoli, R Raecke, R Hossaini, MP Chipperfield, W Feng, RS Gao, EJ Hintsa, JW Elkins, FL Moore, B Daube, J Pittman, S Wofsy, and K Pfeilsticker, "**A New Differential Optical Absorption Spectroscopy Instrument to Study Atmospheric Chemistry from a High-Altitude Unmanned Aircraft**", *Atmos. Meas. Tech. 10*, 1017-1042 (2017).

Acknowledgements

I would like to thank Prof. K. Pfeilsticker who gave me the possibility to develop this work and to explore the admirable world of clouds. I thank him for standing in the ring and fighting in order to better understand what I really was doing...a PhD is a very long process, a growth from many different perspectives.

His group: Tine, Tilman, Dominique, Sebastian...and the previous ones...Ugo, Bodo, Tim, Rasmus and Katja. They are all precious people.

I thank Prof. J. Stutz for the collaboration and his formidable guys: Fedele, James and Max.

I would like to thank also all the NASA ATTREX people (too many names) for the wonderful (Eastern and Western Pacific) experiences.

In particular I thank D. Jordan for his spontaneous friendship when I was far away from home.

I thank the NOAA Water group, they provided important data at the very end of this work. Moreover, I thank also the other groups which were fundamental in the understanding of the final results: Hawkeye, DLH and UCATS.

I would like to thank Prof. Leisner who accepted to be the referee.

At last but not least, I thank my big family with long roots in Friuli, Sicily, Holland,

Rome and Heidelberg. They unconditionally provided, are providing and will provide me a shelter from the life's storms.